Variable-density groundwater flow simulations and particle tracking – Numerical modelling using DarcyTools

Preliminary site description of the Simpevarp area – version 1.1

Sven Follin, SF GeoLogic AB

Martin Stigsson, Sten Berglund
Svensk Kärnbränslehantering AB

Urban Svensson
Computer-aided Fluid Engineering AB

December 2004

SKB

Variable-density groundwater flow simulations and particle tracking – Numerical modelling using DarcyTools

Preliminary site description of the Simpevarp area – version 1.1

Sven Follin, SF GeoLogic AB

Martin Stigsson, Sten Berglund
Svensk Kärnbränslehantering AB

Urban Svensson
Computer-aided Fluid Engineering AB

December 2004

Abstract

SKB is conducting site investigations for a high-level nuclear waste repository in fractured crystalline rocks at two coastal areas in Sweden, Forsmark and Simpevarp. The investigations started in 2002 and have been planned since the late 1990's. The work presented here investigates the possibility of using hydrogeochemical measurements in deep boreholes to reduce parameter uncertainty in a regional modelling of groundwater flow in fractured rock. The work was conducted with the aim of "improving the palaeo-hydrogeological understanding of the Simpevarp area" and to give recommendations to the preparations of the next version of the Preliminary Site Description (1.2).

The study is based on a large number of numerical simulations of transient variable-density groundwater flow through a strongly heterogeneous and anisotropic medium. The simulations were conducted with the computer code DarcyTools, the development of which has been funded by SKB. DarcyTools is a flexible porous media code specifically designed to treat groundwater flow and salt transport in sparsely fractured crystalline rock and it is noted that some of the features presented in this report are still under development or subjected to testing and verification.

The simulations reveal the sensitivity of the results to different hydrogeological modelling assumptions, e.g. the sensitivity to the initial groundwater conditions at 10,000 BC, the size of the model domain and boundary conditions, and the hydraulic properties of deterministically and stochastically modelled deformation zones. The outcome of these simulations was compared with measured salinities and calculated relative proportions of different water types (mixing proportions) from measurements in two deep core drilled boreholes in the Laxemar subarea. In addition to the flow simulations, the statistics of flow related transport parameters were calculated for particle flowpaths from repository depth to ground surface for two subareas within the model domain, Laxemar and Simpevarp. Some of the main findings of this study were: (i) the important role of outcropping deterministically modelled deformation zones, (ii) the importance of studying multiple realisations of the stochastic DFN, (iii) that salinity can be an insensitive parameter for calibration and that model calculations of different water types may be useful as guidance in the calibration process, (iv) that the flow porosity of the deformation zones affects the salinity, which in turn affects the Darcy flux and, hence, the flow related transport parameters, (v) that the local topography within the model domain, which was used to define the ground water table in this study, causes strong local flow cells even for a release area situated close to a regional surface water divide/model boundary.

Sammanfattning

SKB genomför platsundersökningar för ett djupförvar för högaktivt radioaktivt avfall i urberg. Undersökningarna utförs i två kustnära områden i Sverige, Forsmark och Simpevarp. Platsundersökningar påbörjades 2002 och har planerats sedan slutet på nittiotalet. Arbetet som presenteras i denna rapport undersöker möjligheten att använda hydrogeokemiska mätningar i djupa borrhål för att minska parameterosäkerheten vid grundvattenmodellering i sprickigt berg. Arbetet har utförts med målet att uppnå en "ökad förståelse för den palaeo-hydrogeologiska utvecklingen i Simpevarpsområdet", samt att ge rekommendationer inför arbetet med nästa version av den Preliminära Platsbeskrivningen (1.2).

I arbetet ingår ett stort antal densitetsberoende transienta grundvattensimuleringar i ett starkt heterogent och anisotropt medium. Simuleringarna utfördes med beräknings-verktyget DarcyTools, vars utveckling har finansierats av SKB. DarcyTools är ett flexibelt beräkningsverktyg som bygger på en porös-media formulering av strömningsekvationerna. DarcyTools är speciellt anpassad till att kunna hantera flöde och salt transport i sprickigt kristallint berg. Noteras bör att några funktioner som presenteras i denna rapport är alltjämt under utveckling och därmed föremål för tester och behov av verifiering.

Simuleringarna visar på känsligheten för olika hydrogeologiska modellantaganden, exempelvis grundvattnets initialtillstånd 10 000 f Kr, modellområdets storlek och randvillkor samt hydrauliska egenskaper hos deterministiska och stokastiska deformationszoner. Utfallet av simuleringarna jämfördes med uppmätta salthalter och beräknade relativa halter av olika vattentyper från mätningar i två djupa kärnborrhål i Laxemarområdet. Vidare presenteras statistik för transportrelaterade flödesparametrar baserat på simulerade flödesvägar för inerta partiklar som släppts på förvarsnivå från två delområden inom modelldomänen, Laxemar och Simpevarp. Några viktiga iakttagelser i den här studien är: (i) den stora betydelsen av de deterministiskt modellerade deformationszonernas utgående och transmissivitet, (ii) betydelsen av att studera multipla realiseringar av de stokastiskt modellerade deformationszonerna, (iii) att salinitet kan vara en okänslig parameter vid kalibrering och att modellberäkningar av olika vattentyper kan vara användbara som guide i kalibreringsprocessen, (iv) att deformationszonernas flödesporositet påverkar saltfältet vilken i sin tur påverkar darcyflödet och därmed de flödesrelaterade transportparametrarna, (v) att den lokala topografin inom modellområdet, vilken användes för att definiera grundvattenytans läge i denna studie, ger starka lokala flödesceller även för fallet att utsläppsområdet ligger i nära anslutning till en regional ytvattendelare/modellrand.

Contents

1 Introduction

1.1 Background

The Swedish Nuclear Fuel and Waste Management Company (SKB) carries out site investigations in two different candidate areas in Sweden with the objective of describing the in situ conditions for a bedrock repository for spent nuclear fuel. The two candidate areas are named Forsmark and Simpevarp. The site characterisation work is divided into two phases, an initial site investigation phase (IPLU) and a complete site investigation phase (KPLU) /SKB, 2001/. The results of IPLU are used as a basis for deciding on a subsequent KPLU phase. On the basis of the KPLU investigations a decision is made as to whether detailed characterisation will be performed (including sinking of a shaft).

An integrated component in the site characterisation work is the development of site descriptive models. These comprise basic models in three dimensions with an accompanying text description. Central in the modelling work is the geological model which provides the geometrical context in terms of a model of deformation zones and the rock mass between the zones. Using the geological and geometrical description models as a basis, descriptive models for other geodiciplines (hydrogeology, hydrogeochemistry, rock mechanics, thermal properties and transport properties) will be developed /SKB, 2000/. In addition, a description is provided of the surface ecological system, the latter which partly constitutes the interface between the geosphere and the biosphere. Great care is taken to arrive at a general consistency in the description of the various models and assessment of uncertainty and possible needs of alternative models /Andersson, 2003/.

Numerical models are developed at a regional scale (hundreds of square kilometres) and on a local scale (tens of square kilometres). The model on the regional scale model serves to provide boundary conditions for the local scale models. In the Simpevarp area two local scale models are developed, one for the Simpevarp subarea and one for the Laxemar subarea.

Descriptive model versions are produced at specified times which are adapted to the needs of the primary users, i.e. repository design and safety assessment. These specified times define a "data freeze" which singles out the database which should inform the model version in question. The results of the descriptive modelling also serve to produce feedback to, and setting the priorities for the ongoing site characterisation.

1.2 Objectives

A major objective of this study is to support the development of a preliminary Site Description of the Simpevarp area. The work presented is this report is based on the available data of 1 July 2003 (Data Freeze 1.1) and the previous Site Description /SKB, 2002/. The present version of the preliminary Site Description is written off as V1.1 and the previous one as V0. The final version of the Preliminary Site Description is denoted by 1.2, which is due in the beginning of 2005. Inherent in this objective lies a testing of specific hydrogeological issues such as model size, boundary conditions, etc, as well as to give recommendations regarding their treatment in forthcoming model versions. Another major objective is to apply the computer code DarcyTools, the development of which is

funded by SKB. DarcyTools is a flexible porous media code. It is specifically designed to treat flow and salt transport in sparsely fractured crystalline rock and it is noted that some of the features are still under development or subjected to testing and verification, e.g. the multi-rate diffusion model.

A third objective of this study is to assess the role of known and unknown hydrogeological conditions for the present-day distribution of saline groundwater in the Simpevarp area on a regional scale. An improved understanding of the historic (palaeo) hydrogeology and hydrochemistry is necessary in order to gain credibility for the Site Description in general and the hydrogeological-hydrogeochemical description in particular. This is to serve as a basis for describing the present hydrogeological-hydrogeochemical conditions on a local scale as well as predictions of future hydrogeological-hydrogeochemical conditions.

Since hydrogeology and hydrogeochemistry deal with the same geological and hydro-dynamic properties, the two disciplines should be able to complement each other while describing/modelling the bedrock ground water system. The advantages with an integrated modelling approach are numerous, e.g.

- Hydrogeochemical models traditionally focus on the effects from reactions rather than on the effects from flow and transport. An integrated modelling approach can describe flow directions and hence help to understand the origin of the ground water. The turnover time of the ground water system can indicate the age of the ground water and, knowing the flow rate, can be used to indicate the reaction rate.

- Hydrogeological models can, independently from hydrogeochemistry, predict the salinity at any point of the modelled rock volume, and the predictions can be checked by direct hydrogeochemical measurements or indirect calculations. If the chosen hydrodynamic model parameters values and/or processes cannot reproduce the hydrogeochemical observations then the assumptions need to be revised.

1.3   Scope of work and layout of report

The work presented in this report was conducted by The DarcyTools Team involving modelling experts from SF GeoLogic, SKB and Computer-aided Fluid Engineering. The DarcyTools code is developed by Computer-aided Fluid Engineering on behalf of SKB /Svensson et al. 2004; Svensson and Ferry, 2004; Svensson, 2004/.

The report begins with a closer look at the computer code DarcyTools and the workflow for its use in this study (Chapter 2). Chapter 3 presents the overall modelling strategy of this report, the model specifications and the deliverables on groundwater flow and particle tracking. The calibration targets used in this study are presented in Chapter 4 together with the uncertainties that were identified. Chapter 5 presents the results from the transient flow and salinity simulations and Chapter 6 the results form the particle tracking. Finally, Chapter 7 contains a discussion about the possibilities for using the present-day distribution of saline groundwater as a calibration target for groundwater flow models and an improved palaeo-hydrogeological understanding of the Simpevarp area.

1.4   Setting and limitations

The model domain used in this study was identical to the regional model domain of the Simpevarp area, the dimensions of which are 21 km, 13 km and 2.1 km in the Easting (x), Northing (y), and Elevation (z) directions. The deterministically modelled deformation zones available for this study were taken from the V0 deformation zone model. Figure 1-1 shows the model domain and the V0 deformation zones. It is noted that most of deformation zones s are vertical and there are only a few deformation zones that are sub vertical. Also shown are the locations of regional water divides, the local model area, the Simpevarp and Laxemar subareas, the present-day shoreline and the two deep core drilled boreholes in the Laxemar subarea, KLX01 and KLX02. The dimensions of the local model domain were 5.2 km, 3.2 km and 1.1 km in the x,y,z-directions.

The fracture network modelling and the hydrogeochemical flow modelling of the Simpevarp area performed in this study were purposely set to exploit data from the Laxemar subarea solely. The reason was the incomplete preparatory analysis of the hydrogeological and hydrogeochemical data encompassed by the Data Freeze 1.1 at the start of the modelling. As a consequence, simulation results far from the Laxemar subarea are of generic interest mainly. In particular, it is noted that comparisons with field data from the many boreholes in the Äspö subarea and the deep core drilled borehole KSH01 in the Simpevarp subarea are outside the scope of this study.
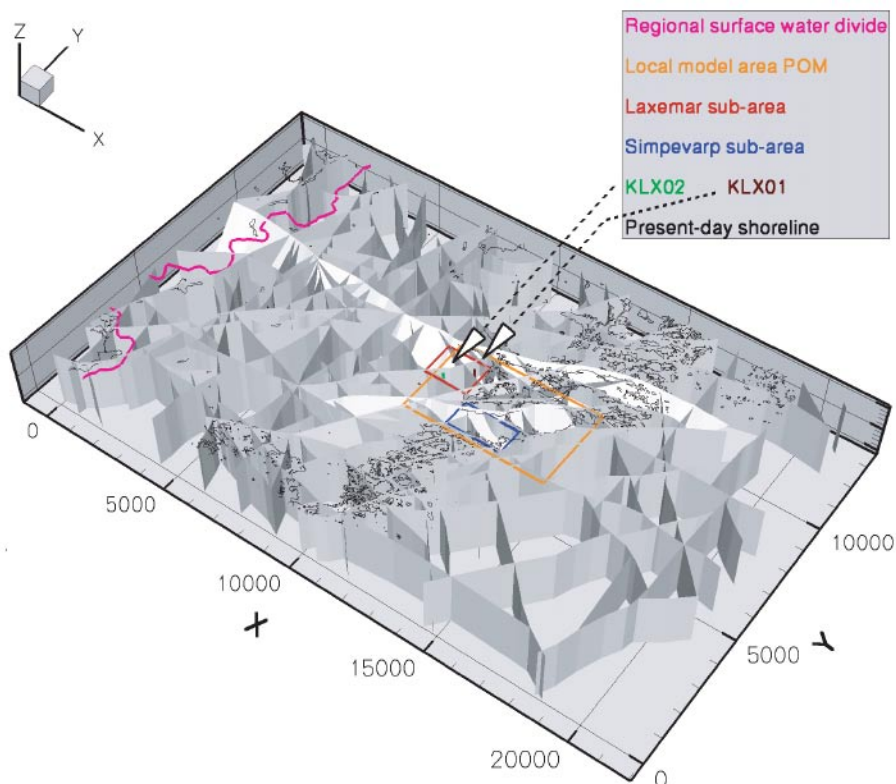
Figure 1-1. *Overview of the V0 deformation zone model of the Simpevarp area. The model consists of 171 deformation zone segments. The dimensions of the regional model domain are 21 km, 13 km and 2.1 km in the x,y,z-directions. The dimensions of the local model domain are 5.2 km, 3.2 km and 1.1 km in the x,y,z-directions.*
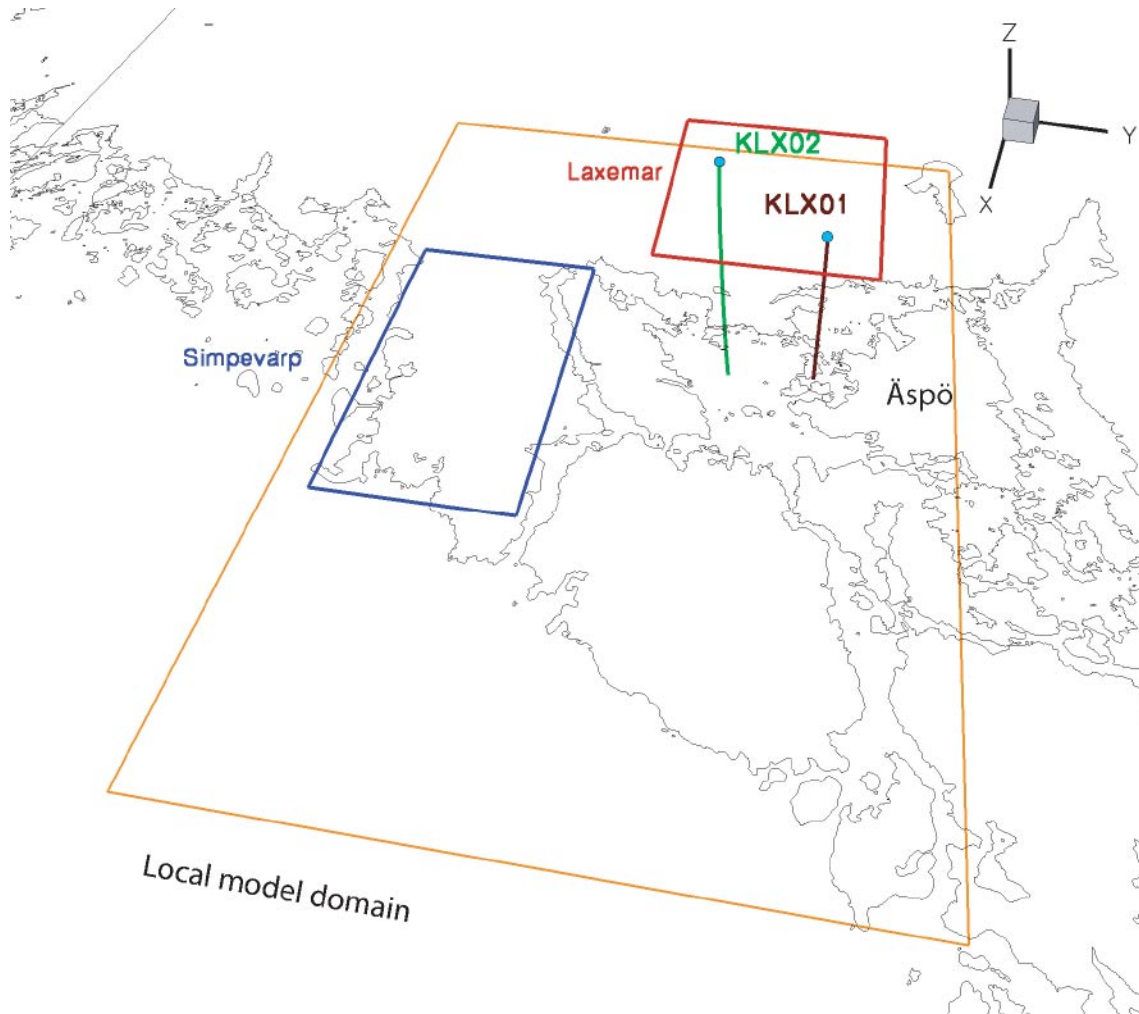
Figure 1-2. *Close-up of the local model area and the Simpevarp (blue) and Laxemar (red) subareas. The local model area is coloured in orange. The cored boreholes KLX01 and KLX02 are subvertical and c 1,100 and 1,700 m long, respectively.*

2 Hydrogeological modelling with DarcyTools

The computer code DarcyTools is intended for simulations of groundwater flow and mass transport in porous and/or fractured media using continuum equations. The fractured medium in mind is a sparsely fractured crystalline rock mass between fracture zones and the porous medium considered is the cover of Quaternary deposits on the top of the bedrock surface. Hence, DarcyTools allows for numerical simulations in accordance with SKB's systems approach for hydrogeological modelling described in /Rhén et al. 2003/.

A number of novel modelling features are incorporated in DarcyTools. The most fundamental feature probably is the method to generate grid properties from a network of discrete fractures /Svensson, 2001a,b/. Using this method the geometric and hydraulic properties assigned to every single fracture is directly represented in the computational grid. This method is believed to result in very accurate anisotropy and connectivity properties.

Detailed descriptions of the functionality of DarcyTools are documented in /Svensson et al. 2004/. However, it is useful to briefly summarise how DarcyTools was used within this study and detail a few specifics of how certain functionalities are implemented in the code.

2.1 Workflow

The starting point is the deterministically modelled deformation zones (DDZ) and the stochastic discrete fracture network model (DFN or SDZ) and its associated statistical properties. The spatial resolution of the flow model, the mesh discretisation (the computational grid), affects the derivation of the grid cell properties. The basic principle used in DarcyTools is to choose a mesh discretisation in accordance with the lower truncation of the fracture size of the stochastic fracturing and to sort out (discard) all isolated fractures generated (regardless of size and properties). The lower truncation is ideally subjected to a sensitivity analysis, which implies that the process is repeated until little or no significant differences can be observed in the flow simulations. The rationale behind this methodology is due to the nature of log-normal and power-law size distributions, which are the size distributions commonly used. That is, a small feature can only be of a potential hydraulic importance if it is connected to a larger feature etc. It is noted that both the fracture intensity and the spatial model for the stochastic fracturing come into play in this methodology.

Once a proper value for the lower truncation on fracture size has been concluded, grid cells without fractures may conceptually be regarded as inactive from an advective flow point of view. In practice, however, low values of the grid cell hydraulic properties have to be used for the sake of the equation solver. The choice of "background rock" hydraulic properties is a function of grid size which in turn depends on the size of the model domain, see Section 2.3. In the work reported here fixed values of the background properties were used. No attempt was made to construct simple block domains on the same scale as the chosen grid resolution to conclude on the heterogeneity or anisotropy. Indeed, such DFN models can be constructed:

- to calculate quantities such as equivalent grid cell hydraulic conductivity as a function of block size, and

- to assess sensitivities to modelling parameters such as truncation of parameter distributions, e.g. fracture length or fracture transmissivity.

When the geometric and hydraulic properties of the DFN conceptual model are properly understood, a large-scale DFN can be constructed within the considered model domain and subsequently transformed to produce an equivalent grid cell model that has hydraulic properties consistent with a realisation of the underlying DFN data. The regional-scale model is then used to simulate transient groundwater flow and salt transport and to provide the basis for particle tracking simulations.

2.2   DFN models

To generate a DFN model with DarcyTools the following data are required:

- Fracture orientation distribution (preferably univariate Fisher).
- Fracture length distribution (preferably Power-law).
- Fracture intensity.
- Fracture spatial model (preferably Poissonian).
- Fracture transmissivity and storativity.
- Fracture thickness.
- Fracture transport aperture.
- Fracture transport diffusivity.
- Fracture flow wetted surface per unit area in the plane of the fracture.

These basic data are used to define the stochastically modelled fracturing and its hydraulic properties. Additional information required for a realistic modelling of the fracture connectivity is the division of fractures into sets and the superposition of deterministically modelled fractures, e.g. deformation zones. Extra complexity can be introduced into models such as:

- Direct or partial correlations between fracture length and transmissivity.
- Heterogeneity on fractures (e.g. varying transmissivity).
- Different fracture intensities within different regions or rock types.
- Excavated damage zones around engineered structures.
- Relationships between fracture properties and directional stress tensors.

2.3   Equivalent grid cell properties

The DarcyTools code is based on a finite volume formulation of the governing differential equations for flow and mass transport. In concrete words this means that the hydraulic and transport properties of a computational grid cell are volumetric functions of:

- The chosen resolution of the computational grid.
- Deterministic deformation zone transmissivity, storativity, thickness, transport aperture, effective diffusivity and flow wetted surface.
- Stochastic fracture (DFN) orientation, intensity size and spatial model connectivity.

- Stochastic fracture (DFN) transmissivity, storativity, thickness, transport aperture, effective diffusivity and flow wetted surface.

- Background rock hydraulic conductivity, specific storage, thickness, flow porosity and effective diffusivity.

The derivation of equivalent grid cell properties in DarcyTools requires that the stochastically modelled DFN is superimposed on top of the deterministically modelled deformation zones. The explanation is that it is only the connected features that are retained, whereas all non-connected stochastic features are discarded prior to the calculation. A description of the derivation of the equivalent grid cell properties in DarcyTools is given by /Svensson, 2001a,b/.

DFN models can currently be constructed within simple structured block domains containing up to c 10 million cells using the latest version of DarcyTools (2.1) on a 32 bits PC with 4 GB RAM. The version to come within the next couple of months (3.0) will be able to treat unstructured grids as well.

2.4   Salt

Salt transport is treated by means of two processes in DarcyTools:

- advection-diffusion within the mobile pore volume in the computational grid, and

- diffusive exchange between the immobile and mobile pore volumes on a sub-grid scale (matrix diffusion).

The advection-diffusion equation in DarcyTools is written as /Svensson et al. 2004/:

$$
\frac{\partial \rho \varepsilon_p}{\partial t} + \frac{\partial}{\partial x}\left(\rho u C - \rho \gamma D_x \frac{\partial C}{\partial x}\right)
$$
$$
+ \frac{\partial}{\partial y}\left(\rho v C - \rho \gamma D_y \frac{\partial C}{\partial y}\right) \qquad (2\text{-}1)
$$
$$
+ \frac{\partial}{\partial z}\left(\rho w C - \rho \gamma D_z \frac{\partial C}{\partial z}\right) = QC + Q_c
$$

where ρ is the fluid density, ε_p is the flow porosity, (u, v, w) are the Darcy fluxes, C is the transported mass fraction of salt (kg/kg) and (D_x, D_y, D_z) are the effective diffusivities. Q and Q_c are source/sink terms, where Q_c represents the diffusive exchange of salt between the mobile and immobile pore volumes. The concept of diffusion into immobile volumes in DarcyTools ranges from the short time (fast) diffusion into the easily reached stagnant pools of water nearby a flowing feature to the long time (slow) diffusion into the less porous rock "far" away from the flowing feature, the depth of which depends on the modelled time scale. A more thorough explanation of this important concept is found in /Svensson et al. 2004/.

Figure 2-1 shows a generalised model of the transition zone between flow and immobile pore volumes as conceptualised in the TRUE project /Andersson et al. 2002b/.
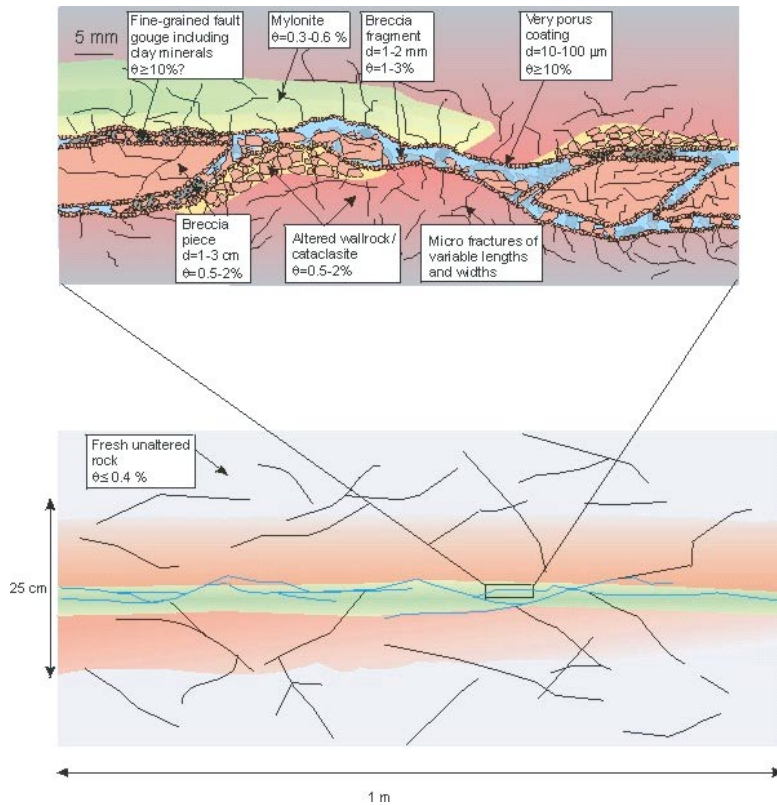
Figure 2-1. *Generalised conceptual model of a typical conductive structure involved in the tracer experiment (from /Andersson et al. 2002b/).*

The diffusive exchange of salt between the immobile and mobile pore volumes Q_c is modelled by a multi-rate diffusion process in DarcyTools. The implementation of the multi-rate diffusion process is based on the one-dimensional multi-rate diffusion model by /Haggerty and Gorelick, 1995/. One of the key parameters of the multi-rate diffusion model is the capacity ratio between the immobile and mobile pore volumes. According to /Neretniks, pers comm, 2004/ the pore volume in the rock matrix accessible for diffusion, ε_p, is expected to be 10–100 times greater than the pore volume in the water-conducting fractures, ε_f. The current working hypothesis used in DarcyTools is that the capacity ratio ought to be of the same order of magnitude.

The grid cell capacity ratio β_c in DarcyTools may be written as:

$$\beta_c = \frac{V_{im,c}}{V_{m,c}} \tag{2-2}$$

where $V_{im,c}$ and $V_{m,c}$ are the grid cell values of the immobile and mobile pore volumes, respectively.

By the same token, the total, or global, capacity ratio of the entire model domain β_G may be written as:

$$\beta_G = \frac{\sum\limits_{c} V_{im,c}}{\sum\limits_{c} V_{m,c}} \tag{2-3}$$

14

In the current version of DarcyTools it is assumed that the immobile pore volume in a grid cell is directly proportional to the accumulated flow wetted surface of all features intersecting the cell. The implication of this assumption can best be illustrated by an example:

Consider a cubic grid cell with a cell size of 100 m entirely intersected by a horizontal feature. The intersecting feature is larger than the cell size but its thickness is thinner. If the flow wetted surface per unit area in the plane of the feature is 2 m²/m², the feature's contribution to the grid cell's total flow wetted surface is 20,000 m².

Hence, if FWS_f denotes the contribution to the flow wetted surface of a grid cell from feature f and FWS_c the accumulated flow wetted surface of all features that intersect the cell, the current assumption made in DarcyTools may be written as:

$$FWS_c = \left(\sum_f FWS_f \right)_c \tag{2-4}$$

$$V_{im,c} = k \ FWS_c \tag{2-5}$$

$$\sum_c V_{im,c} = k \sum_c FWS_c \tag{2-6}$$

The ratio between the immobile pore volume in a grid cell and the total immobile pore volume may be written as:

$$\frac{V_{im,c}}{\sum_c V_{im,c}} = \frac{FWS_c}{\sum_c FWS_c} \tag{2-7}$$

If the value of the total capacity ratio of the bedrock is given, or assumed to be known, the spatial variability of the capacity ratio on the scale of a computational grid cell can be estimated by combining the definitions in Equation (2-2) and (2-3) with the assumption behind Equation (2-7), i.e.

$$\beta_c = \beta_G \left(\frac{FWS_c}{\sum_c FWS_c} \right) \left(\frac{\sum_c V_{m,c}}{V_{m,c}} \right) \tag{2-8}$$

As a consequence, the value of the proportionality constant k in Equation (2-5) and (2-6) may be written as:

$$k = \frac{\beta_G}{\left(\dfrac{\sum_c FWS_c}{\sum_c V_{m,c}} \right)} \tag{2-9}$$

A series of capacity boxes with different mass transfer coefficients α_i are used in the multi-rate model to model the diffusive exchange of matter between the mobile and immobile pore volumes /Haggerty and Gorelick, 1995; Svensson et al. 2004/. The capacity box with the lowest value of the mass transfer coefficient (α_{min}) is the slowest capacity box and vice versa, i.e. the time scale of the diffusion into the capacity boxes is $1/\alpha_i$.

In the work reported here ten capacity boxes were used. The value of α_{max} was set to $4 \cdot 10^{-7}$ s^{-1} and the value of α_{min} was set to $4 \cdot 10^{-12}$ s^{-1}. These values were fixed throughout the study and there was no particular reason for choosing these values other than that the time scale for the slowest capacity box was set to be of the same order of magnitude as the overall simulation time, i.e. c 8,000 years.

The exchange of matter by diffusion with the rock mass exposed by the flow wetted surface can be expected to be related to two parameters; the flow wetted surface per unit volume of flowing water in the flowpath, a_w, and the advective travel time, t_w. The exchange will increase with both these parameters and a new variable, the F-parameter (or the F-quotient) /Andersson et al. 1998/ has been introduced for this product:

$$F = a_w \, t_w \tag{2-10}$$

The discretised form of Equation (2-10) for a flowpath through a grid cell may be written as:

$$F_c = \left(\frac{FWS}{V_m} \right)_c \left(t_{w,exit} - t_{w,entrance} \right)_c \tag{2-11}$$

and integrating along the entire flowpath yields:

$$F = \sum_c F_c \tag{2-12}$$

The mobile pore volume of a grid cell c in DarcyTools may be written as:

$$V_{m,c} = \sum \left(\varepsilon_f \, V_f \right)_c \tag{2-13}$$

where ε_f is the flow porosity of an intersecting water-conducting feature and V_f the total volume of the feature in the cell. The flow porosity of the water-conducting feature may be written as:

$$\varepsilon_f = \frac{e_f}{b_f} \tag{2-14}$$

where e_f is the total thickness of the empty space in the feature available for flow and b_f as the geological thickness of the feature. It is noted that e_f may be thought of as the transport aperture e_t for which there exists several expressions, among which the cubic law probably is the most well known. Equation (2-15) shows one of the power-law expressions used in the TRUE project at the Äspö HRL /Dershowitz et al. 2003/,

$$e_t = 0.5 \, T^{0.5} \tag{2-15}$$

16

It is noted that Equation (2-15) is derived from tracer experiments in single fractures over short distances and that there are few if any tracer experiments conducted in deformation zones over longer distances, e.g. 100 m or more. There is also limited experience of using Equation (2-15) in regional flow studies as in the work reported here. The implication of the equations above in a large grid cell can best be illustrated by an example:

Consider a cubic grid cell with a cell size of 100 m entirely intersected by a horizontal feature. The intersecting feature is larger than the cell size but its geological thickness is thinner, e.g. 10 m, and the transmissivity is $2 \cdot 10^{-5}$ m^2/s. Equation (2-15) renders that the feature's thickness of empty space is $2.24 \cdot 10^{-3}$ m and Equation (2-14) that its flow porosity is $2.24 \cdot 10^{-4}$. Its contribution to the grid cell's total mobile pore volume is 22.4 m^3 according to Equation (2-13) and if no other features are intersecting the grid cell, the flow porosity of the grid cell becomes $2.24 \cdot 10^{-5}$.

2.5   Water types

In Chapter 3 we introduce the concept of water types and in Chapter 4 we make an attempt to make an integration with a hydrogeochemical concept known as mixing proportions as defined by the M3 method /Laaksoharju et al. 1999a,b/. More information about the conceptual meaning of water types as used in this study is given in Chapter 3. In Chapter 5 we demonstrate the practical application of the integrated approach while discussing the results of the numerical simulations.

The point made here is that the solution of the variable-density groundwater flow problem described above is supplemented by a simultaneous solution of five advection-dispersion equations describing the advective flow ($D_e \approx 0$) of five water types; one equation per water type. It is noted that the driving mechanism behind the advection is the Darcy fluxes obtained from the coupled solution of pressure and salinity in the variable-density groundwater flow problem. The use of water types can be considered to be a particular form of particle tracking where concentration is used instead of particles. In the work reported here we did not subject the simulation of water types to matrix diffusion. It is noted that the multi-rate model used for modelling diffusion of salt can be used also for modelling diffusion of water types.

3 Model setup and specifications

3.1 Modelling methodology

The modelling methodology used in this study follows SKB's systems approach for hydro-geological modelling /Rhén et al. 2003/. This approach divides the geosphere into three types of Hydraulic Domains, representing the Quaternary deposits (HSD), the deformation (fracture) zones (HCD) and the rock mass between the zones (HRD), see Figure 3-1.

In order to ease the evaluation of the impact of:

- geometrical alternatives in the structural geology and bedrock fracturing,
- variants in the initial and boundary conditions, and
- parameter uncertainties (i.e. uncertainties in the hydraulic property assignment).

on the groundwater flow system, the design of each numerical modelling study will be formalised in terms of one or several internal Task Descriptions (TD). A TD may be regarded as a guidance, or recommendation, for the workflow of the numerical modelling to be performed. Another important objective of using TDs is to promote proposals of further investigations of the hydrogeological conditions at the site. The TD for this particular study is written off as TD 1.5 the specified components and deliveries of which are listed below.
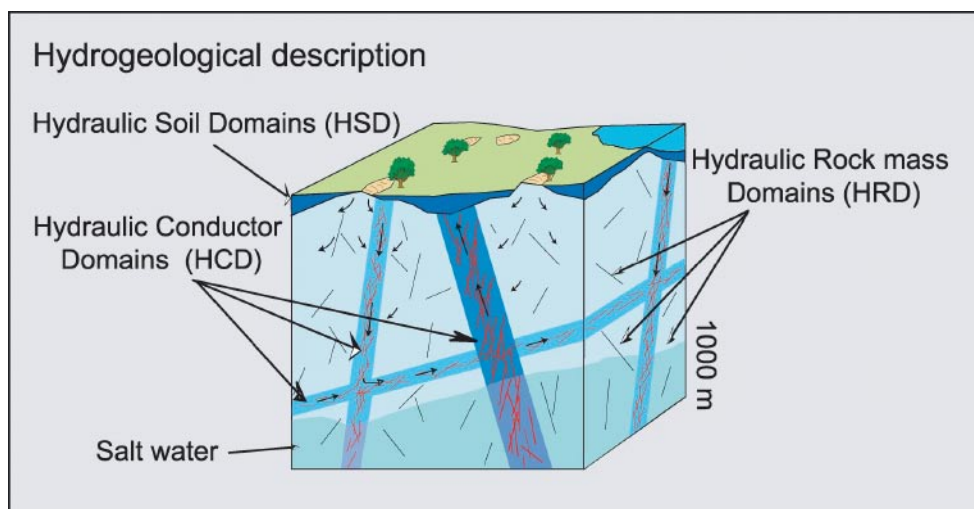
Figure 3-1. *The Quaternary deposits and the crystalline bedrock are divided into separate hydraulic domains named Hydraulic Soil Domains (HSD), Hydraulic Rock mass Domains (HRD) and Hydraulic Conductor Domains (HCD). Within each domain the hydraulic properties are represented by mean values or by spatially distributed statistical distributions. Modified after /Rhén et al. 2003/.*

The scope of the TD 1.5 is simplified concerning geometrical alternatives in the deter-ministically modelled deformation zone model, HCD. The only case treated is shown in Figure 1-1. This simplification was motivated by the incomplete development of the V1.1 deformation zone model at the start of this study. In support of the development of the next Site Description of the Simpevarp area, however, the modelling will assess the impact of the V1.2 deformation zone model as well as its accompanying geometric alternatives (if such exist). Another important simplification made in the TD 1.5 is that all deformation zones were interpreted as brittle (fracture zones) and water-conductive. Figure 3-2 shows the dimensions of the regional model domain to scale together with the location of the regional surface water divide and the deterministically modelled deformation zones.

Figure 3-3 shows the representation of discrete features as envisaged in the TD 1.5. As indicated in the figure the minimum size (length) of the deterministically modelled deformation zones (HCDs) was set to 1,000 m. In this study, the stochastic fracturing of the HRD between the HDCs was modelled as a network of discrete features representing local minor deformation zones ranging between 100 m and 1,000 m in size, each of which consisted of a large number of small fractures ranging between decimetres to metres in size (not modelled here). The properties of the Discrete Feature Network (DFN) of local minor zones were modelled by means of statistical distributions for orientation, size, intensity, spatial model and transmissivity. The sizes of the DFN were modelled as a truncated power-law size distribution.

The locations of the deterministically modelled deformation zones and their connectivity to the stochastic network govern the heterogeneity and anisotropy of the computational grid. The spatial resolution of the computational grid was set to 100 m in the horizontal plane. The choice of scale affects the derivation of the grid cell properties. In the TD 1.5 the hydraulic properties of the grid cells that were not intersected by deterministic or stochastic deformation zones were tacitly modelled as a homogeneous and isotropic continuum. Figure 3-4 shows a close up of the computational grid. The discretisation in the horizontal directions was 100 m. In the vertical direction the model domain was divided into 24 layers each of which were c 100 m thick except for the two uppermost layers, which were three and ten metres thick, respectively. The total number of grid cells in the regional model domain was 655,200.

The TD 1.5 conceptualised the near surface geological conditions in the model area to a 3 m thick layer of Quaternary deposits on top of a 10 m thick rock layer, which was more considered more fractured than the bedrock at depth. The Quaternary deposits as well as the uppermost bedrock were assigned uniform thicknesses and homogeneous and isotropic hydraulic properties, different for each layer. In reality, large parts of the Simpevarp area, in particular where the Laxemar and Simpevarp subareas are located, have almost no till, i.e. the bedrock is in practise outcropping. The till encountered has a maximum thickness of about 1–2 m /Bergman et al. 1999/.

Considering the great depth of the model domain (2.1 km) and the large amount of outcropping bedrock the rationale for incorporation a layer of Quaternary deposits into the hydrogeological model can be questioned. It was decided not to incorporate a layer of Quaternary deposits in this study but to treat the two layers closest to the ground surface as bedrock for the reasons stated above. This decision was further supported by the simplified boundary condition used on the top surface, which assumed a fixed water table following the undulating ground surface.
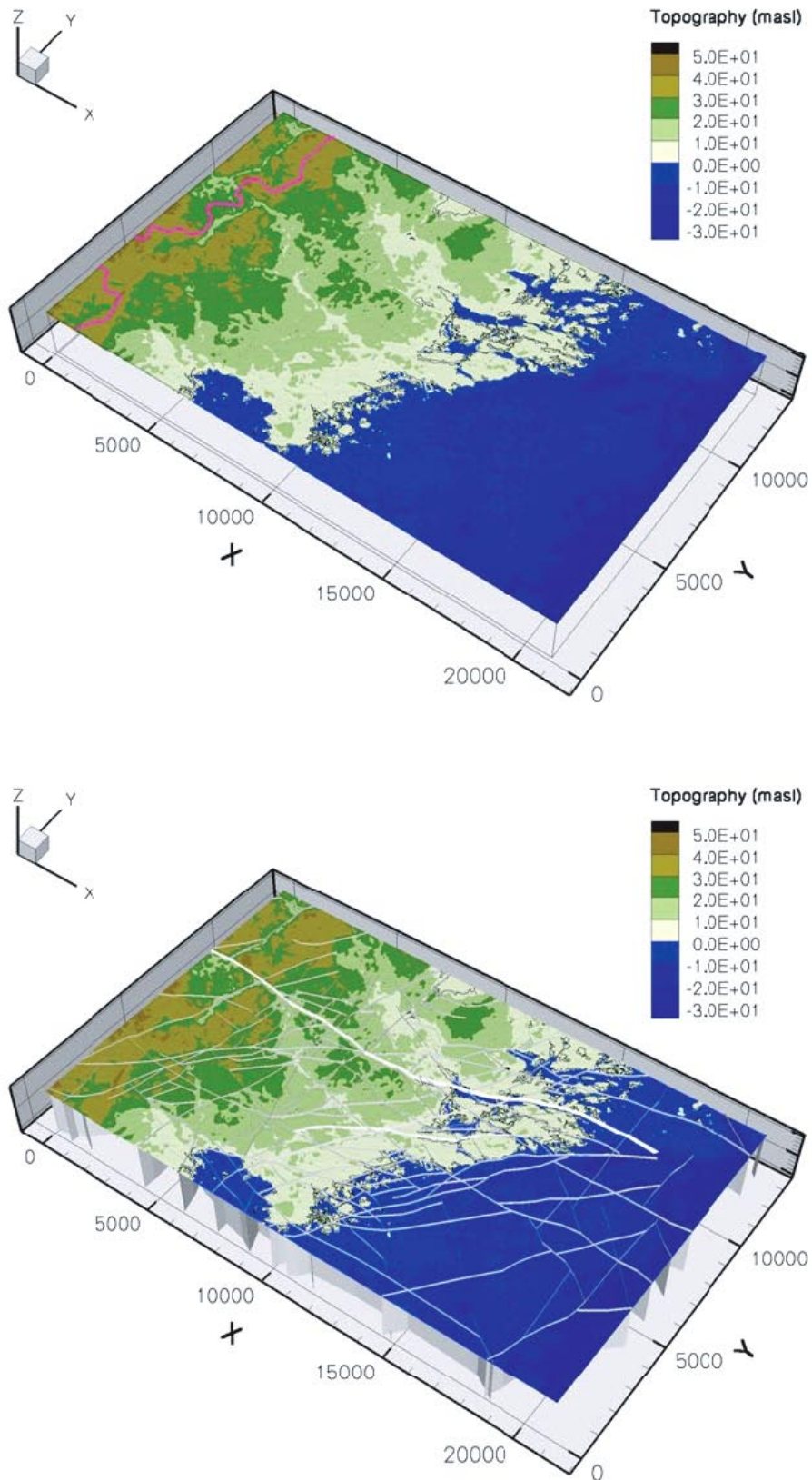
Figure 3-2. *Dimensions of the regional model domain to scale. The bottom boundary is located at (–2,100) masl. Top: The regional surface water divide (shown in pink). Bottom: The outcropping of the deterministically modelled deformation zones (shaded), see also Figure 1-1.*
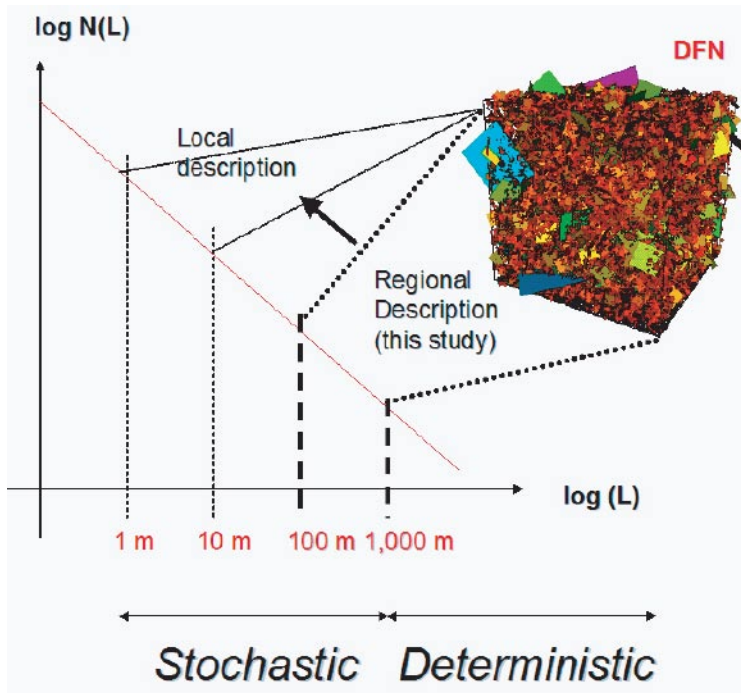
Figure 3-3. *Schematic view of the conceptual model of deformation zones described in the TD 1.5. The treatment of the bedrock in the numerical model depends on the scale and properties of the fracturing. The graph indicates that a power-law size distribution was advocated.*
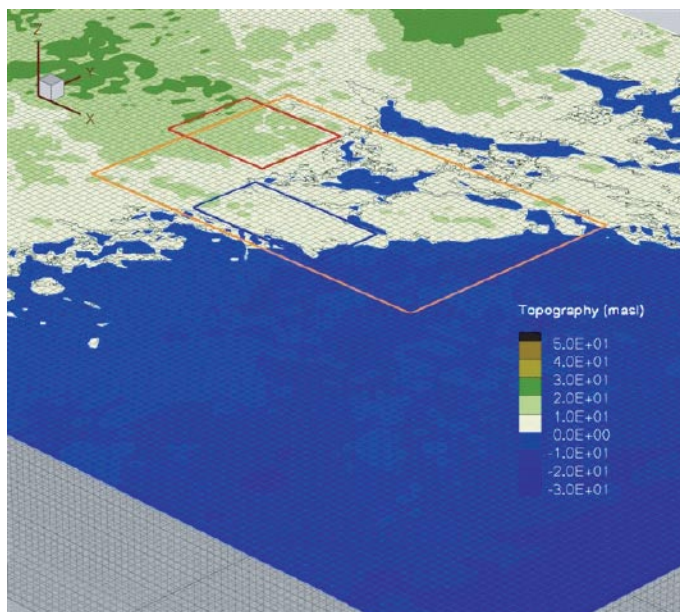
Figure 3-4. *Close up of the computational grid. The discretisation in the horizontal directions was 100 m. In the vertical direction the model domain was divided into 24 layers each of which were c 100 m thick except for the two uppermost layers. The locations of the Laxemar and Simpevarp subareas are indicated together with location of the local model area (cf Figure 1-1).*

3.2 Base Case

The modelling work specified in the TD 1.5 was formed around a Base Case and a limited number of variants. An excerpt of the major parameter settings for the Base Case is listed in Table 3-1.

While executing the modelling work specified in the TD 1.5, it was recognised that two of the Base Case specifications above led to unrealistic results, namely (i) the intensity of the DFN and (ii) the treatment of hydraulic conductivity of the background rock closest to ground surface, i.e. the uppermost rock layer.

The intensity of the DFN of the Base Case was found to be quite high and produced a quite modest heterogeneity and anisotropy in the resulting hydraulic conductivity field for the chosen grid resolution, hence quite different from the typical hydraulic behaviour of sparsely fractured crystalline rock.

Table 3-1. Excerpt of some major parameter settings of the Base Case in the TD 1.5.

Initial salinity conditions

Zero salinity down to (–550) masl. Thereafter, a linearly increasing salinity to 10% by weight at (–2,100) masl.

This setting was in this study accompanied by an assumption of 100% Glacial water and 0% old saline water ("Brine") down to (–550) masl. Thereafter, a linearly decreasing content of Glacial water to 0% at (–2,100) masl and, by the same token, a linearly increasing content of Brine to 100% at (–2,100) masl.

Processes and boundary conditions

Transient topographic pressure on the top surface as a function of the modelled shoreline displacement during the considered period of Holocene (10,000 BC and 2,000 AD).

Transient salinity on the top surface as a function of the modelled sea water changes in the Baltic region during the considered period of Holocene.

No-flow on all lateral (vertical) surfaces and on the base surface at (–2,100) masl.

Fixed salinity of 10% by weight on the base surface at (–2,100) masl.

Deterministic deformation zone transmissivity

$T = 1.3 \cdot 10^{-5}$ m²/s

Stochastic deformation zone intensity, power-law slope and spatial model in 3D

P_{32} = 0.0371 m²/m³, L > 100 m, CCDF k_r = 2.6, Poisson distributed fracture centres

Pole orientations and relative proportions of stochastic deformation zone sets

Fracture set	Mean pole trend	Mean pole plunge	Dispersion	Distribution	% of fractures
1	262	3.8	8.52	Fisher	24.9
2	195.9	13.7	9.26	Fisher	32.1
3	135.9	7.9	9.36	Fisher	25.9
4	35.4	71.4	7.02	Fisher	17.1

Stochastic deformation zone transmissivity

$T = a\,L^b$; a = $2.47 \cdot 10^{-12}$ m²/s, b = 1.791

Background rock hydraulic conductivity

$K = 1 \cdot 10^{-12}$ m/s

Top layer rock hydraulic conductivity

$K = 1 \cdot 10^{-9}$ m/s

The hydraulic conductivity of the uppermost rock layer was in the TD 1.5 taken to be three orders of magnitude greater than the hydraulic conductivity of the background rock at depth, i.e. $1 \cdot 10^{-9}$ m/s instead of $1 \cdot 10^{-12}$ m/s. This contrast in the hydraulic conductivity was tacitly assumed to be sufficient for taking the effect of an increased fracturing of the uppermost part of bedrock into account. During the modelling process, however, it was recognised that this treatment of the uppermost bedrock was too simplistic and, in fact, quite decisive for the palaeo-hydrogeological question. In concrete words the concept of a homogeneous conductive uppermost rock layer with a constant hydraulic conductivity of $1 \cdot 10^{-9}$ m/s was found to rule out the impact of outcropping high transmissive deterministically modelled deformation zones, which affected the flushing of rock.

Table 3-2 shows how the treatment of the uppermost rock layer as specified in the TD 1.5 affected the vertical component of the hydraulic conductivity tensor. The effect is shown for two different values of the DFN intensity P_{32}, $3.71 \cdot 10^{-2}$ m²/m³ and $7.42 \cdot 10^{-3}$ m²/m³. Also shown in Table 3-2 is the modified treatment of the uppermost rock used in the present study.

The conclusion drawn from Table 3-2 is that the transmissivity of the deterministically modelled deformation zones as well as the conceptual model for their outcropping is of great importance for the hydraulic contact with the top boundary conditions and thus for the hydraulic behaviour of the entire flow model. The stochastically modelled deformation zones have random orientations in space and are not sufficiently transmissive to have an equally significant impact on the results. However, the intensity of the stochastically modelled deformation zones has a strong impact on the heterogeneity and anisotropy in the resulting conductivity field between the deterministically modelled deformation zones. Table 3-3 lists the properties of the Base Case in the TD 1.5 and the modifications made and used in this study. The most important changes are underlined.

Table 3-2. The treatment of the uppermost rock layer as specified in the TD 1.5 affected the hydraulic contact between the bedrock and the top boundary. The percentages in the table refer to the total number of K_z values within the local model area (1,664). Results for two different stochastic deformation zone intensities are shown. The roles of the intensity of the stochastic deformation zones and the transmissivity of the deterministicaly modelled deformation zones are readily seen in the statistics.

	High DFN intensity $P_{32} = 3.71 \cdot 10^{-2}$ m²/m³	Low DFN intensity $P_{32} = 7.42 \cdot 10^{-3}$ m²/m³
Example distributions of grid cell K_z for the uppermost rock layer based on the outcropping of deterministic and stochastic deformation zones	13% $K_z < 10^{-9}$ m/s	49% $K_z < 10^{-9}$ m/s
	47% $K_z = 10^{-9}$–10^{-8} m/s	14% $K_z = 10^{-9}$–10^{-8} m/s
	17% $K_z = 10^{-8}$–10^{-7} m/s	14% $K_z = 10^{-8}$–10^{-7} m/s
	23% $K_z = 10^{-7}$–10^{-6} m/s (Deterministic zones)	23% $K_z = 10^{-7}$–10^{-6} m/s (Deterministic zones)
Base Case setting of the uppermost rock layer as specified in the TD 1.5	100% $K_z = 10^{-9}$ m/s	100% $K_z = 10^{-9}$ m/s
Modified treatment of the uppermost rock layer as used in this study	13% $K_z = 10^{-9}$ m/s	49% $K_z = 10^{-9}$ m/s
	87% $K_z = 10^{-9}$–10^{-6} m/s	51% $K_z = 10^{-9}$–10^{-6} m/s

Table 3-3. Detailed comparison between the suggested Base Case parameter settings in the TD 1.5 and the final Base Case parameter settings as used in this study.

Parameter	Suggested Base Case TD 1.5	Base Case This study
Quaternary deposits K (m/s), ε_p (–) and t (m)	$1.5 \cdot 10^{-5}$, $5 \cdot 10^{-2}$, 3	Not included
Position of the initial salinity interface (masl)	–500	–550
Deterministic deformation zone T (m²/s)	$1.3 \cdot 10^{-5}$	$1.3 \cdot 10^{-5}$
Deterministic deformation zone b_f (m)	10–50	20
Deterministic deformation zone S (–)	$2 \cdot 10^{-5}$	0
Deterministic deformation zone ε_f (–)	–	$5 \cdot 10^{-3}$
Deterministic deformation zone D_e (m²/s)	–	$5 \cdot 10^{-12}$
Stochastic deformation zone 3D CCDF k_r (–)	2.6	2.6
Stochastic deformation zone minimum L_0 (m)	100	100
Stochastic deformation zone maximum L (m)	1,000	1,000
Stochastic deformation zone P_{32} L > 100 m (m²/m³)	$3.71 \cdot 10^{-2}$	$7.42 \cdot 10^{-3}$
Stochastic deformation zone a; $T = a\, L^b$	$2.47 \cdot 10^{-12}$	$2.47 \cdot 10^{-12}$
Stochastic deformation zone b (–); $T = a\, L^b$	1.791	1.791
Stochastic deformation zone b_f (m)	0.5–2	0.01L
Stochastic deformation zone S (–)	$2 \cdot 10^{-6}$–$1 \cdot 10^{-5}$	0
Stochastic deformation zone ε_f (–)	$2 \cdot 10^{-6}$–$1 \cdot 10^{-5}$	$5 \cdot 10^{-3}$
Stochastic deformation zone D_e (m²/s)	$2 \cdot 10^{-14}$–$1 \cdot 10^{-13}$	$5 \cdot 10^{-12}$
Background rock K (m/s)	$1 \cdot 10^{-12}$	$1 \cdot 10^{-12}$
Background rock S_s (m⁻¹)	–	$1 \cdot 10^{-9}$
Background rock ε_p (–)	$1 \cdot 10^{-5}$	$1 \cdot 10^{-5}$
Background rock D_e (m²/s)	–	$1 \cdot 10^{-15}$
Background rock β_G (–)	–	10
Specific flow wetted surface per unit area (m²/m²)	–	2
Uppermost rock K (m/s)	$\equiv 1 \cdot 10^{-9}$	$> 1 \cdot 10^{-9}$
Uppermost rock S_s (m⁻¹)	–	$1 \cdot 10^{-6}$
Uppermost rock b (m)	10	13
Uppermost rock ε_p (–)	–	$1 \cdot 10^{-3}$
Uppermost rock D_e (m²/s)	–	$1 \cdot 10^{-12}$

3.3 DFN model of stochastically modelled deformation zones

Two of the more important assumptions of the DFN model of the stochastically modelled deformation zones (SDZ) are the power-law distribution for their sizes and the model for their spatial distribution in space. A pertinent reference of this study for both of these matters is the recent work by /Darcel, 2003/, who treated data on various scales from the Äspö subarea. In this study we comment briefly comment on the former assumption, whereas the latter assumption is tacitly accepted/adopted.

The slope of the CCDF plot for 2D size (trace length) is of uttermost importance for hydrogeology as it affects both the connectivity of the stochastically modelled deformation zones and the relationship between zone size and transmissivity, $T = a\, L^b$. Figure 3-5 shows a CCDF plot of the V0 deterministically modelled deformation zone traces (DDZ). The

traces were formed by means of a linked lineament analysis, some of which was based on airborne geophysics. The blue line is this graph is subjectively matched. The slope of the blue line is 1.6 which is the 2D equivalence of the 3D value specified in the in the TD 1.5. The conclusion drawn here is that the power-law slope can not be determined with certainty and that a CCDF slope of 1.6 in 2D can neither be rejected nor supported on behalf of Figure 3-5. It is noted, however, that a 2D slope of 1.2 produces a better statistical fit than 2D slope of 1.6.

The result of using a power-law size distribution, a Poisson process for the stochastic deformation zone centres are exemplified in Figure 3-6 through Figure 3-10. The fracturing for two different values of the SDZ intensity are visualised in Figure 3-6 and Figure 3-7. The higher intensity value ($3.71 \cdot 10^{-2}$ m^2/m^3) corresponds to the Base Case in the TD 1.5 and rendered c 740,000 stochastic deformation zones and a mean flow porosity of $1.1 \cdot 10^{-3}$ within the regional model domain. The lower intensity value, ($7.42 \cdot 10^{-3}$ m^2/m^3) corresponds to the chosen Base Case for this study and rendered c 131,000 stochastic deformation zones and a mean flow porosity $3.8 \cdot 10^{-4}$. In both cases the cut-off size is 100 metres.

The total number of grid cells at repository depth within the local model area is 1,664. The lower intensity value renders that c 3.5% of grid cells at this level were not intersected by stochastic deformation zones in any direction and that c 13.5% grid cells were not intersected by stochastic deformation zones in at least one direction. For the higher intensity value all grid cells were intersected by stochastic deformation zones in all directions. Hence, the lower intensity value resulted in a flow medium that is much more heterogeneous and anisotropic.
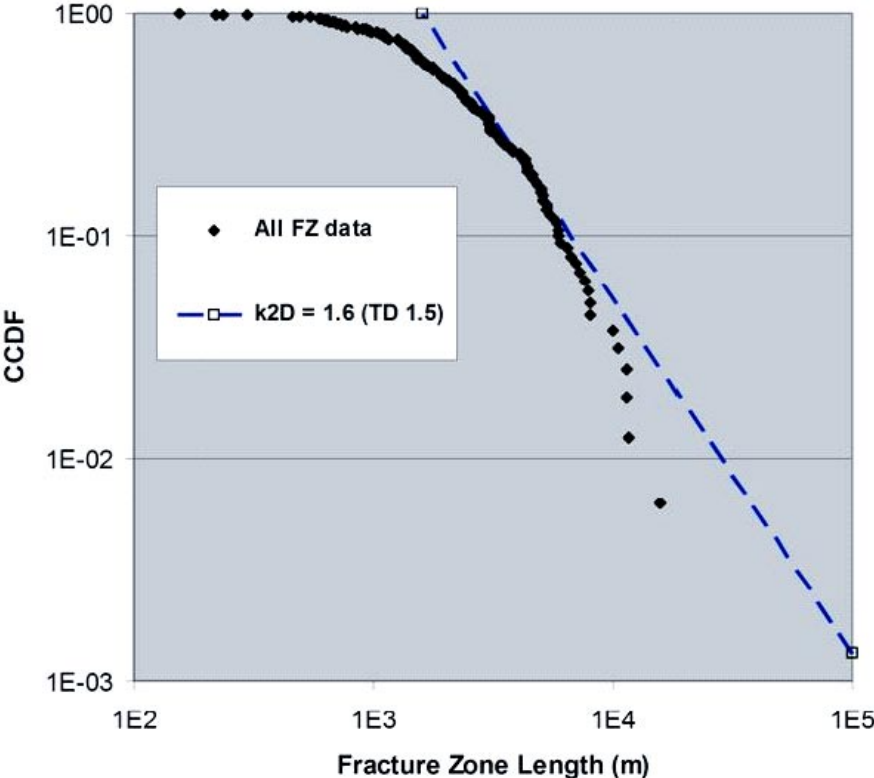
Figure 3-5. *CCDF plot for the trace lengths of the deterministically modelled deformation zones (DDZ). It is noted that a number of the V0 deformation zone traces are shorter than 1,000 m.*
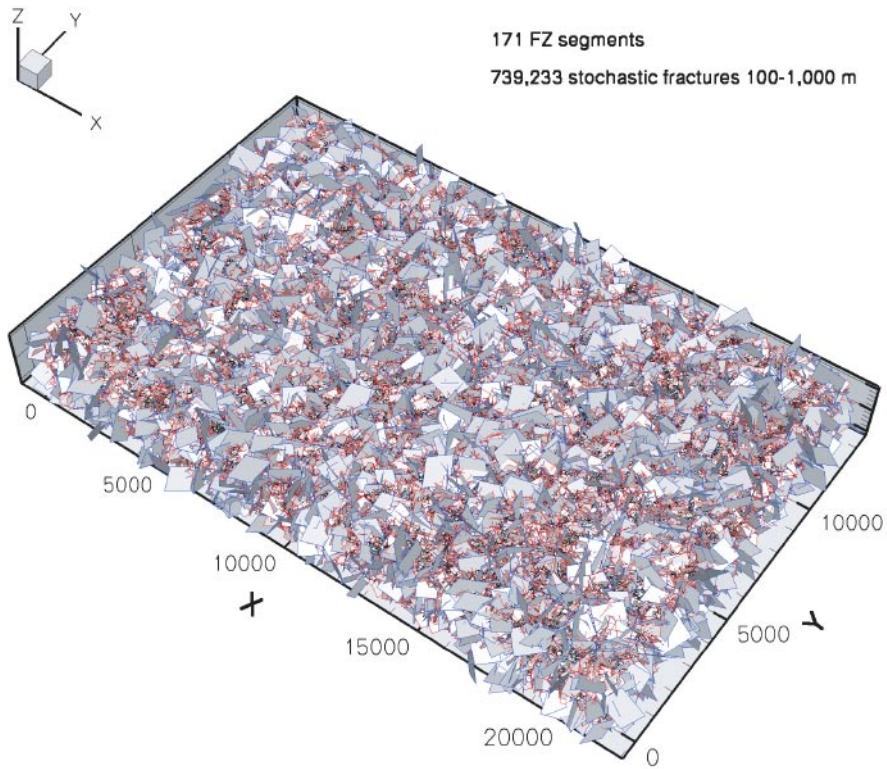
Figure 3-6. *The intensity value for the Base Case as specified in the TD 1.5 rendered c 740,000 stochastic deformation zones (SDZ) within the regional model domain.*
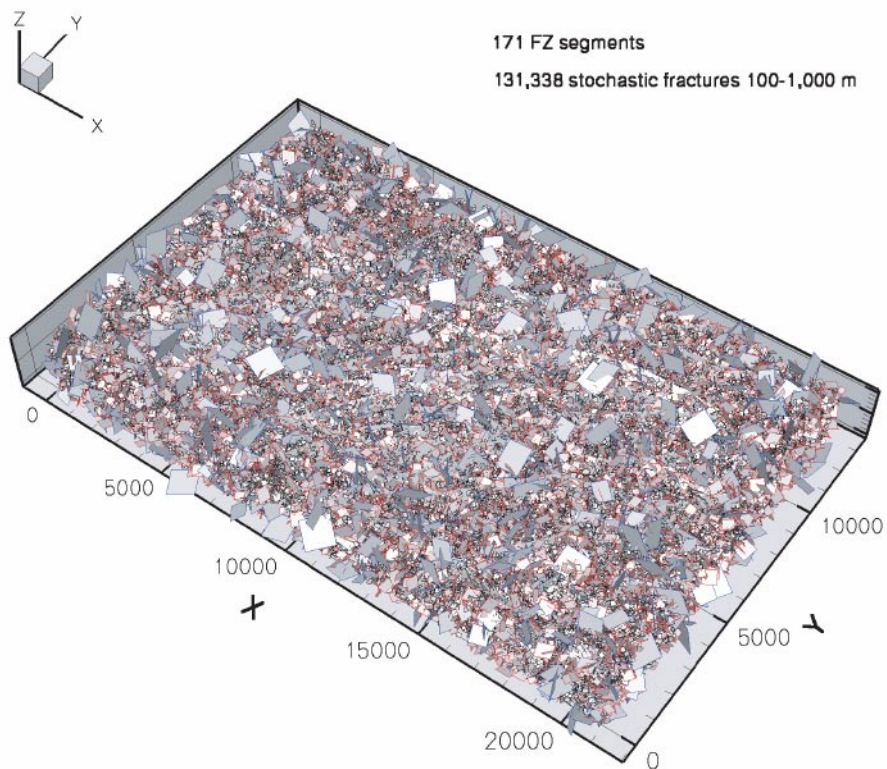
Figure 3-7. *The intensity value for the modified Base Case as used in this study rendered c 131,000 stochastic deformation zones (SDZ) within the regional model domain.*

27

171 FZ segments

608,341 stochastic fractures 100-200 m

171 FZ segments

103,317 stochastic fractures 100-200 m
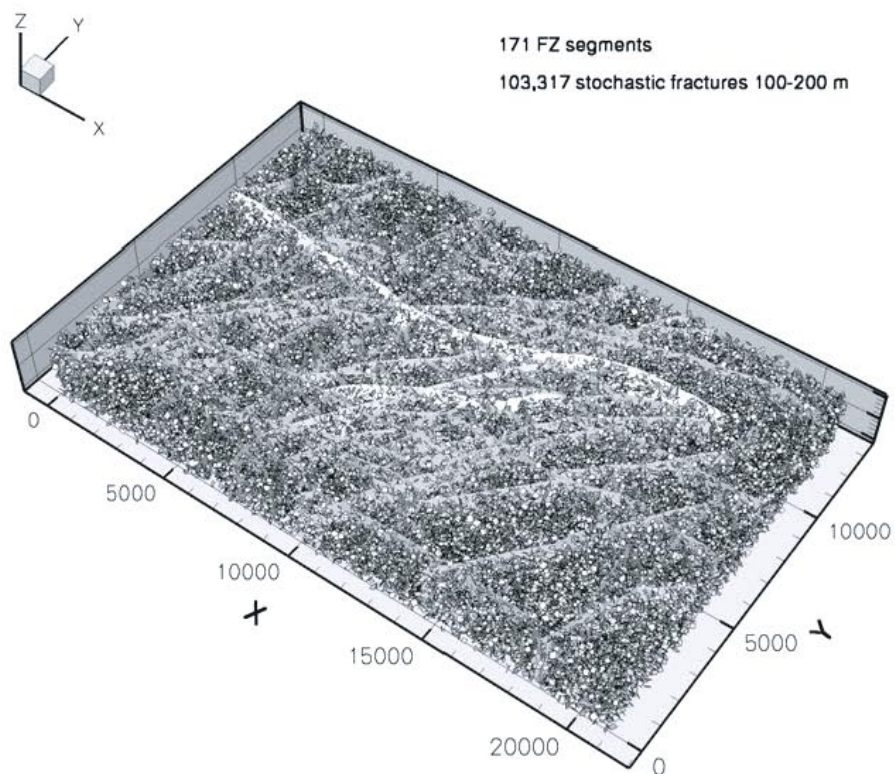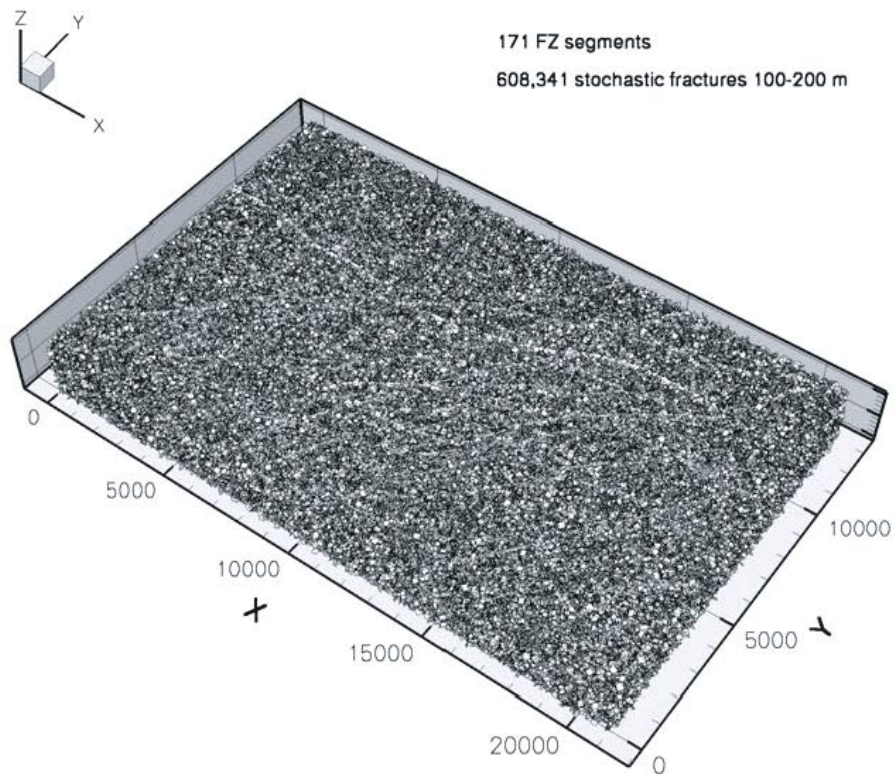
Figure 3-8. *Visualisation of stochastic deformation zones (SDZs) in the range 100–200 m. Top: The Base Case specified in the TD 1.5. Bottom: The modified Base Case as used in this study. The large features seen behind the SDZ are the DDZs.*

171 FZ segments

118,539 stochastic fractures 200-500 m

171 FZ segments

25,527 stochastic fractures 200-500 m
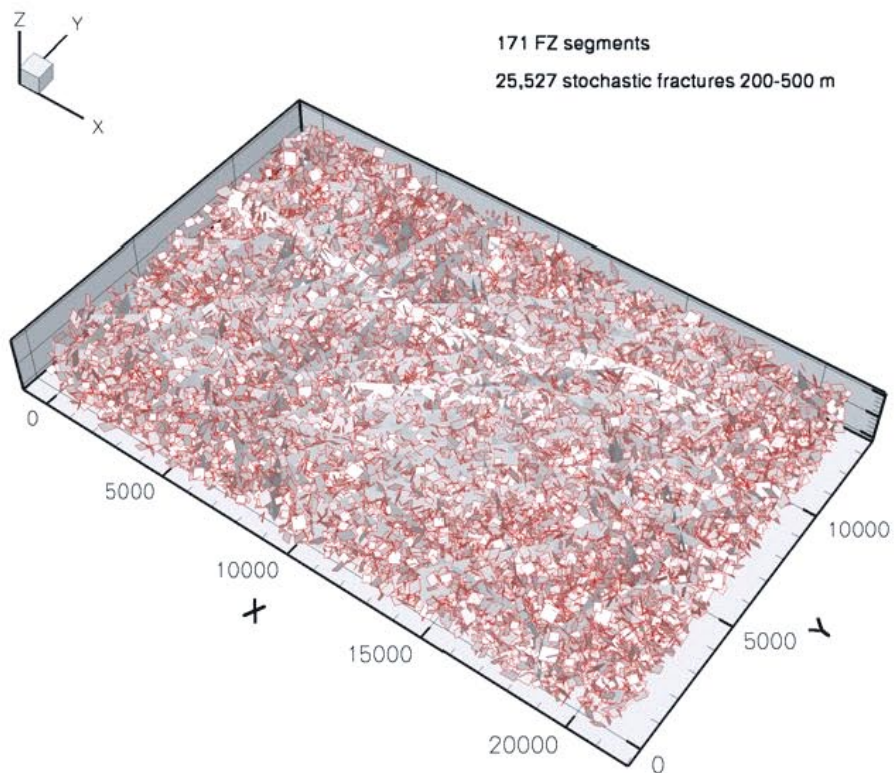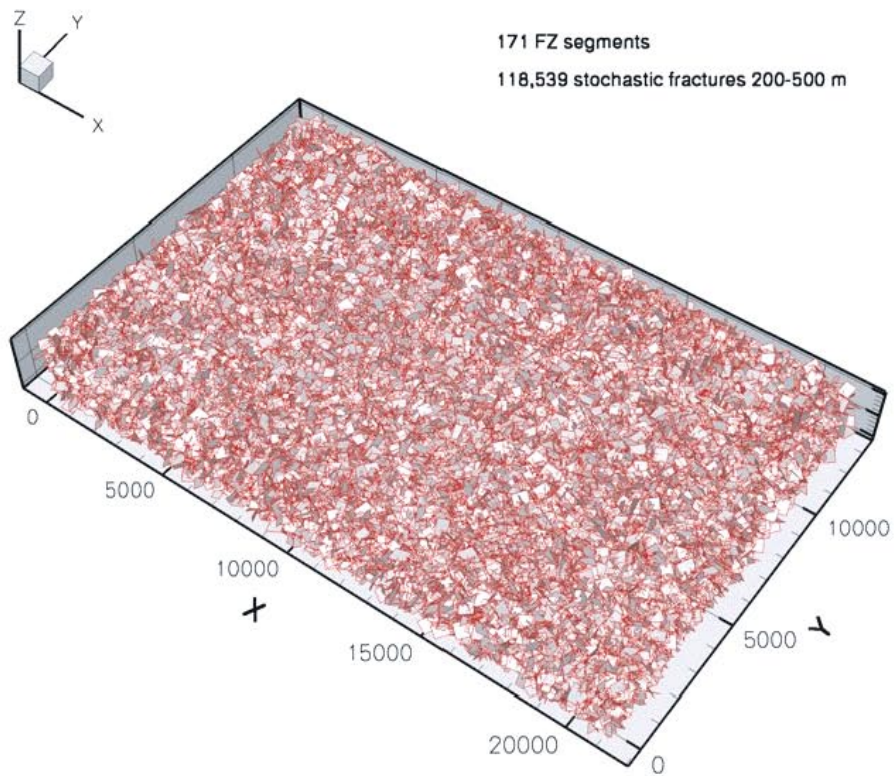
Figure 3-9. *Visualisation of stochastic deformation zones (SDZs) in the range 200–500 m. Top: The Base Case specified in the TD 1.5. Bottom: The modified Base Case as used in this study. The large features seen behind the SDZ are the DDZs.*

29

171 FZ segments

12,353 stochastic fractures 500-1,000 m

171 FZ segments

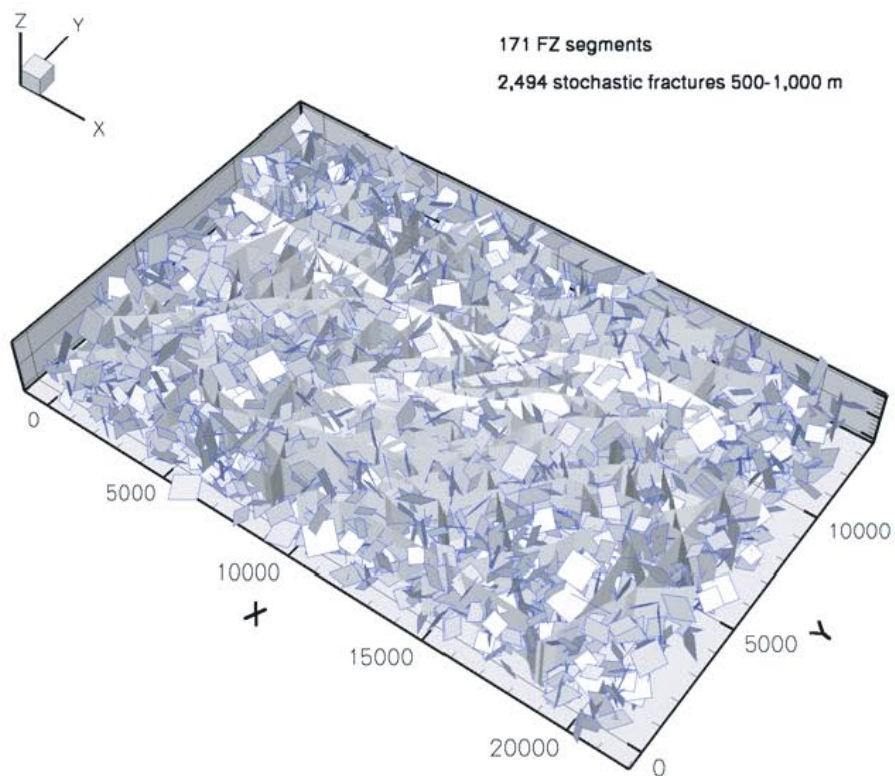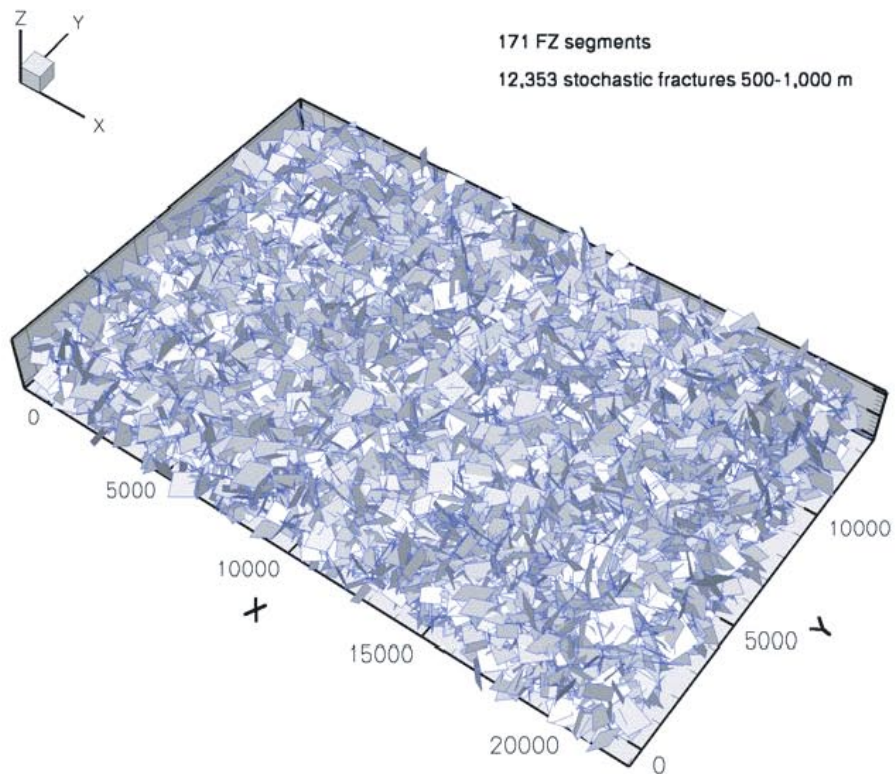2,494 stochastic fractures 500-1,000 m

Figure 3-10. *Visualisation of stochastic deformation zones (SDZs) in the range 500–1,000 m. Top: The Base Case specified in the TD 1.5. Bottom: The modified Base Case as used in this study. The large features seen behind the SDZ are the DDZs.*

3.4   Sensitivity study

The modelling work with DarcyTools comprised a large number of simulations of variable-density groundwater flow. These were performed to investigate the influence of conceptual and parameter uncertainties relating to initial and boundary conditions, DFN data interpretation, and background rock properties including properties affecting the rock matrix diffusion. Some of these simulations were along the original intensions of the TD 1.5, whereas others extended the scope of work significantly. The rationale for executing the extended work was to promote the inter-disciplinary discussions about the role of geological, hydrogeochemical and hydrogeological parameter uncertainties. As such, the present study contributes not only to the modelling project for Simpevarp but also to the modelling project for Forsmark. An overview of the different model variations studied in this study is shown in Table 3-4 and is further commented below.

Model #1 meets more or less the Base Case specifications in the TD 1.5, cf Table 3-3, and constitutes the reference case for Models #2–4. The results led to choosing the parameter values of Model #5 as the Base Case for the work presented in this report.

Model #2 investigates the sensitivity to a lower flow porosity of all deformation zones.

Model #3 investigates the sensitivity to a lower DFN intensity.

Model #4 investigates the sensitivity to both a lower flow porosity and a lower DFN intensity in combination.

Model #5 is the chosen modification of Model #1 and constitute the Base Case for this study and is, consequently, the reference case for Models #6–14.

Model #6 investigates the sensitivity to a deeper initial position of the salinity interface.

Model #7 investigates the sensitivity to a shallower initial position of the salinity interface.

Model #8 investigates the sensitivity to a smaller regional model domain approximately mimicking the anticipated effect of a surface water divide, i.e. a no flow boundary.

Model #9 investigates the sensitivity to a lower flow porosity of all deformation zones.

Model #10 investigates the sensitivity to a doubled capacity ratio (cf Chapter 2).

Model #11 investigates the sensitivity to a five-doubled capacity ratio (cf Chapter 2).

Model #12 investigates the sensitivity to another seed, i.e. stochastic DFN realisation.

Model #13 investigates the sensitivity to less transmissive DFN (SDZs).

Model #14 investigates the sensitivity to less transmissive DDZs.

The fixed correlation between transmissivity T and size L for the DFN is probably one of the more hesitant assumptions of this study. Since there were no data from the data freeze 1.1 to support a site specific relationship/assumption it was decided to use the preliminary expression derived in the V1.1 Site Description for Forsmark /SKB, 2004/. It is noted, however, that the expression used is very tentative and based on a number of assumptions, some of which may show up not be applicable at all as more data are gathered. In addition, correlations between T and L, if they exist, may be site specific.

Table 3-4. Overview of studied models. Model #1 meets the Base Case specification in the TD 1.5. The results of Models #1–4 led to Model #5, which constitutes the Base Case for this study and the reference case for Models #6–14. Blank fields in the table means 'no change'.

Parameter	#1	#2	#3	#4	#5	#6	#7	#8	#9	#10	#11	#12	#13	#14
Pos. of the salinity interface (masl)	–550				–550	–1,050	–100							
Water divide/no flow boundary	No				No			Yes						
Determ. deform. zone T (m²/s)	1.3E–5				1.3E–5									1.3E–6
Determ. deform. zone t (m)	20				20									
Determ. deform. zone S (–)	2.5E–6				2.5E–6									
Determ. deform. zone ε_r (–)	5E–3	1E–3		1E–3	5E–3				1E–3					
Determ. deform. zone D_e (m²/s)	5E–12	1E–12		1E–12	5E–12				1E–12					
Random number seed (–)	1234				1234							5678		
Stoch. deform. zone spatial model	Poisson				Poisson									
Stoch. deform. zone CCDF 3Dslope (–)	2.6				2.6									
Stoch. deform. zone minimum L (m)	100				100									
Stoch. deform. zone maximum L (m)	1,000				1,000									
Stoch. deform. zone P_{32c} (m²/m³)	3.71E–2		7.42E–3	7.42E–3	7.42E–3									
Stoch. deform. zone a (m²/s); T = a L^b	2.47E–12				2.47E–12								2.47E–13	2.47E–13
Stoch. deform. zone b (–); T = a L^b	1.791				1.791									
Stoch. deform. zone t (m)	0.01L				0.01L									
Stoch. deform. zone S (–)	2.5E–6				2.5E–6									
Stoch. deform. zone ε_r (–)	5E–3	1E–3		1E–3	5E–3				1E–3					
Stoch deform. zone D_e (m²/s)	5E–12	1E–12		1E–12	5E–12				1E–12					
Background rock K (m/s)	1E–12				1E–12									
Background rock S_s (m⁻¹)	1E–9				1E–9									
Background rock ε_p (–)	1E–5				1E–5									
Background rock D_e (m²/s)	1E–15				1E–15									
Background rock ε_r (–)	10				10					20	50			
Spec. flow wetted surface (m²/m²)	2				2									
Uppermost rock K (m/s)	1E–9				> 1E–9									
Uppermost rock S_s (m⁻¹)	1E–6				1E–6									
Uppermost rock t (m)	13				13									
Uppermost rock ε_p (–)	1E–3				1E–3									
Uppermost rock D_e (m²/s)	1E–12				1E–12									
Commented in Chapter 5 (Flow)	No	No	Yes	No	Yes	Yes	Yes	Yes	Yes	Yes	Yes	Yes	Yes	Yes
Commented in Chapter 6 (Transport)	Yes	No	Yes	No	Yes	No	Yes	Yes	Yes	No	No	Yes	Yes	Yes

## 3.5   Processes, boundary and initial conditions

Two closely associated hydrogeological processes were considered in the numerical simulations; shoreline displacement due to glacial rebound and changes in the salinity of the Baltic Sea. Figure 3-11 shows the modelled shoreline displacement and Figure 3-12 the modelled changes in the sea water salinity during the considered period of Holocene (10,000 BC–2,000 AD). The approximate starting times of the different sea water periods and their maximum salinities as modelled in the work presented here are indicated in Figure 3-11 and in Table 3-5.

The solution of the variable-density groundwater flow problem was supplemented by a simultaneous solution of the equations describing the advective flow ($D_e \approx 0$) of the different water types; one equation per water type, cf Section 2.5. It is noted that the driving mechanism behind the advection is the Darcy fluxes obtained from the solution of the variable-density groundwater flow problem.
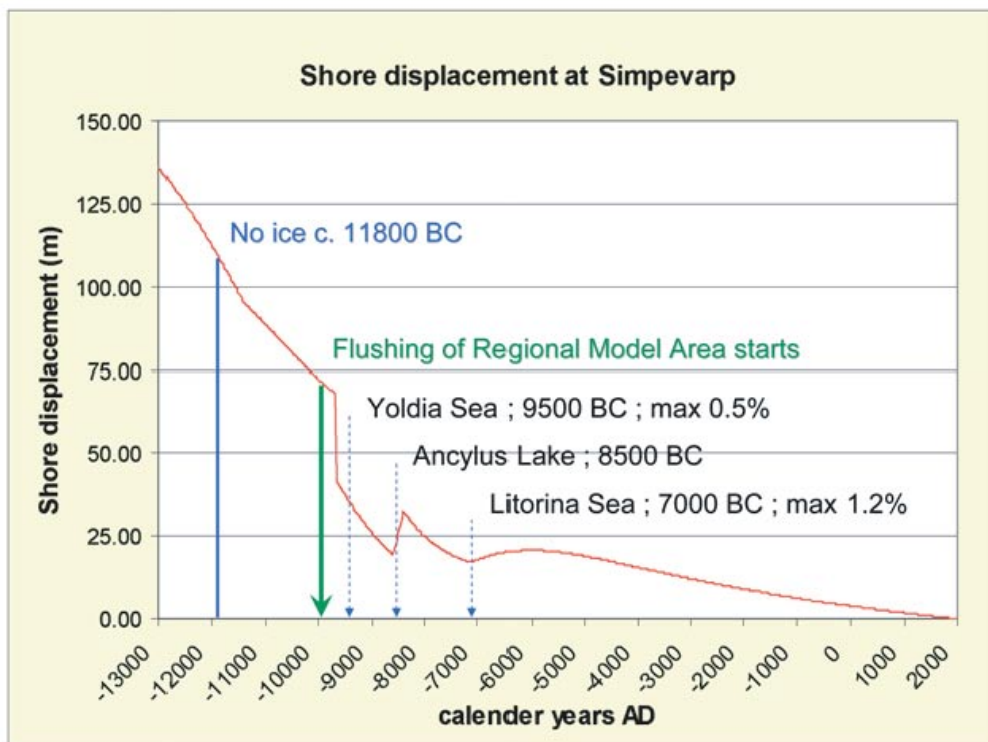
Figure 3-11. *Schematic view of the shoreline displacement in the Simpevarp area as modelled during the considered period of Holocene. The starting times of the different sea water periods and their maximum salinities are indicated. Modified after /Påsse, 1996/.*
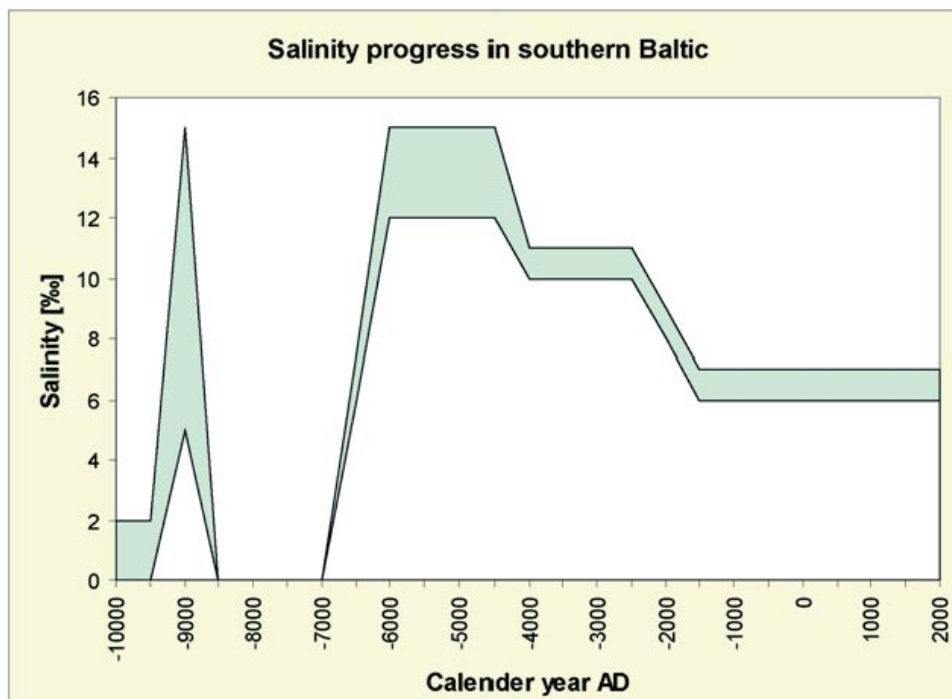
Figure 3-12. *Schematic view of the changes in the sea water salinity in the Baltic region as modelled during the considered period of Holocene. The width of the green field indicates the salinity uncertainty. Modified after /Westman et al. 1999/.*

Table 3-5. Summary of modelled approximate starting times (calender years) and durations of the different sea water periods as considered in the simulations in this report (cf Figure 3-12).

Water type / Initial Conditions	Start	Duration
Fixed Brine/Old saline groundwater of 10% by weight at (–2,100) masl and linearly decreasing to 0% at (–500) masl	10,000 BC	12,000
100% fresh Glacial groundwater down to (–500) masl and linearly decreasing to 0% at (–2,100) masl	10,000 BC	Flushed
Water type / Top boundary Conditions	**Start**	**Duration**
100% Yoldia Sea water (slightly brackish)	9,500 BC	1,000
100% Ancylus Lake water (fresh)	8,500 BC	1,500
100% Littorina Sea water (clearly brackish)	7,000 BC	5,500
100% Meteoric water (fresh) on outcropping rock	10,000 BC	12,000
Baltic Sea water (slightly brackish)	1,500 BC	3,500

Figure 3-13 shows the location of the shoreline in the Simpevarp area in plane view at six different time slices coinciding with the start of each sea water period. The location of borehole KLX02 is above the sea water level prior to the start of the Littorina period. In the beginning of the Littorina period, however, the area was subjected to a transgression which lasted for about 1,000 years. The maximum water depths in the model at the location of KLX02 is circa three metres and at KLX01 circa five metres.
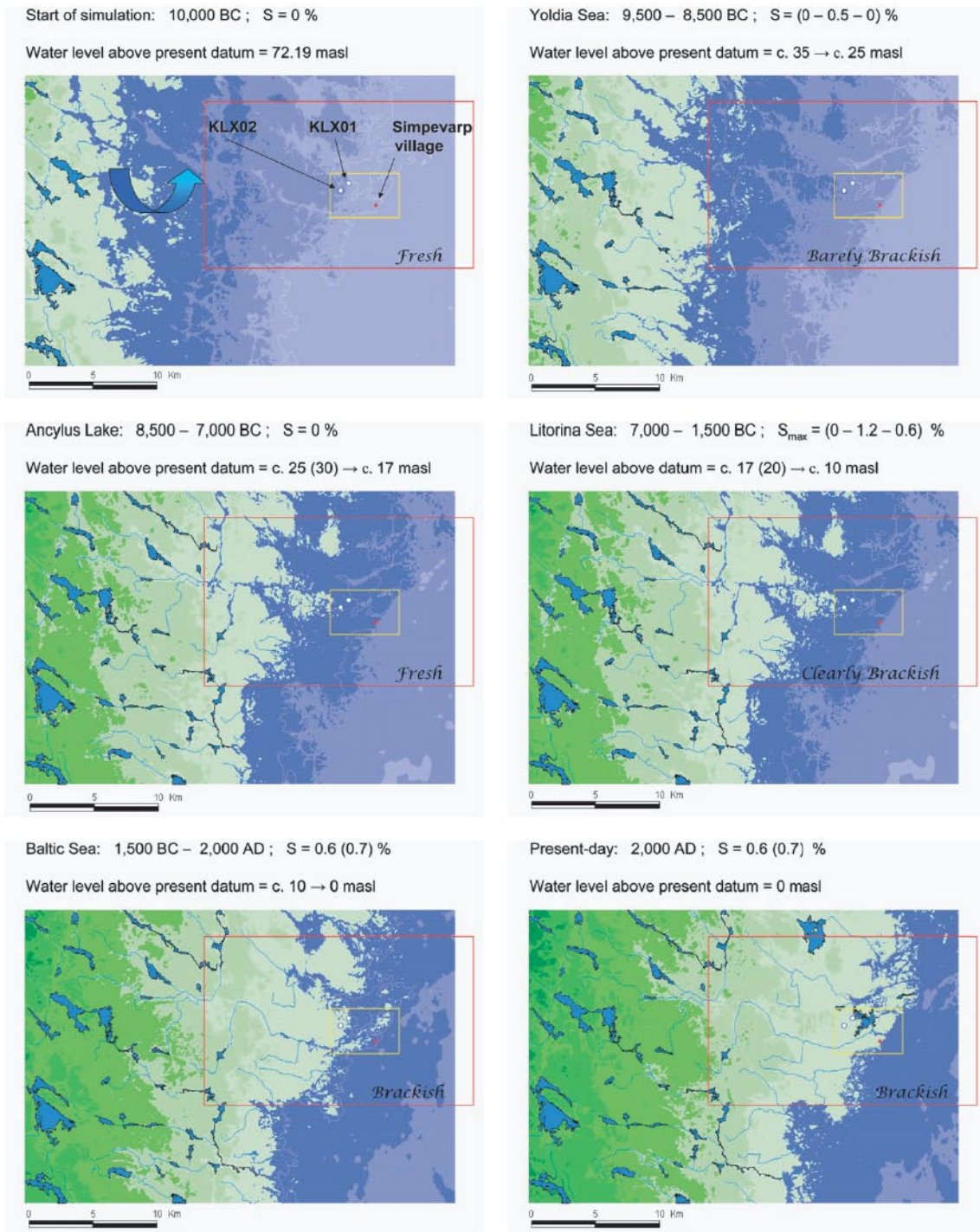
Figure 3-13. *Plane view of the shoreline displacement in the Simpevarp area as modelled during the considered period of Holocene. Modified after /Brydsten, 1999/.*

The general modelling approach used in this study is to keep the model domain fixed (i.e. same x, y and z coordinates at all times), and modify the residual pressure and salinity on the top according to Figure 3-11 and Figure 3-12. The approach tacitly assumes that the subsurface is fully saturated at all times and that the local topography is the main mechanism for the superficial spatial distribution of recharge and discharge. That is, surface water and superficial groundwater flow divides coincide and the body of the groundwater recharge at ground surface discharges locally.

No attempt was made in this study to calibrate the flux across the top surface against the specific runoff, which is the maximum recharge value possible without lowering the groundwater table. The reason for this limitation is the simplified treatment of the top boundary condition and the exclusion of the Quaternary deposits, see Section 2-1. However, recharge profiles were calculated while comparing Models #3 and 5 in Table 3-4. The results of the recharge profile calculations are presented in Section 5.1.

The assumed initial spatial distributions of Brine and Glacial water at the onset of the simulation period (10,000 BC) are schematically shown in Figure 3-14. This figure also illustrates the assumed locations of the initial salinity interface, cf Models #5–7 in Table 3-4, together with the two boundary conditions used to address the role of the regional surface water divide, cf Models #5 and 8 in Table 3-4. Figure 3-15 shows a plan view of the difference between Models #5 and 8.

Finally, an important assumption was made concerning the hydraulic properties. These were assumed to be constant at all times despite the glacial rebound. The glacial rebound is believed to increase the porosity and the permeability of the rock /Lars O Ericsson, pers comm, 2004/ due to a volumetric expansion close to ground surface. Observations in field data that may support this is discussed by, e.g. /Rohr-Torp, 2000/.
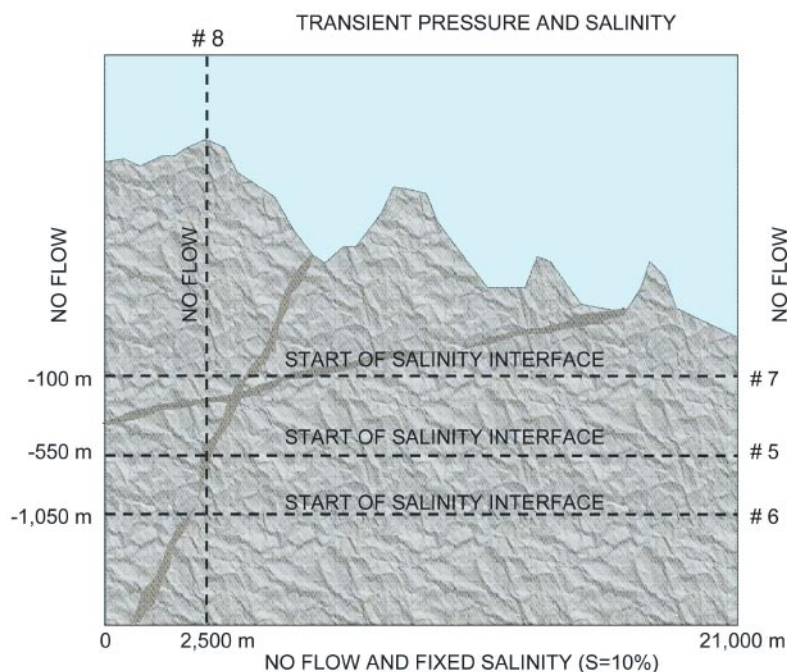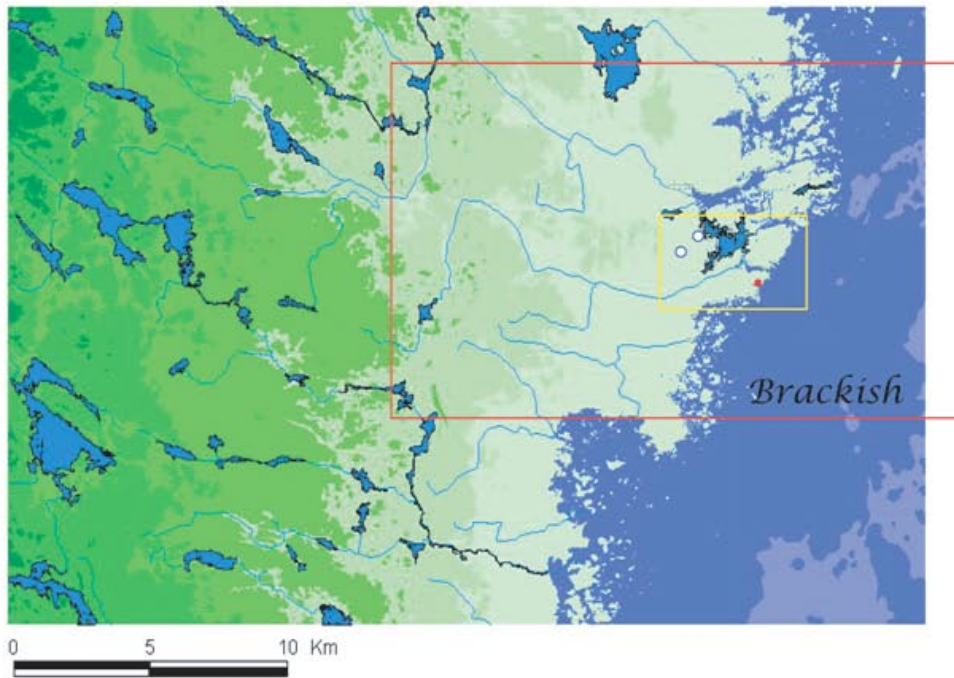

Figure 3-14. *Schematic illustration of the initial and boundary conditions studied.*
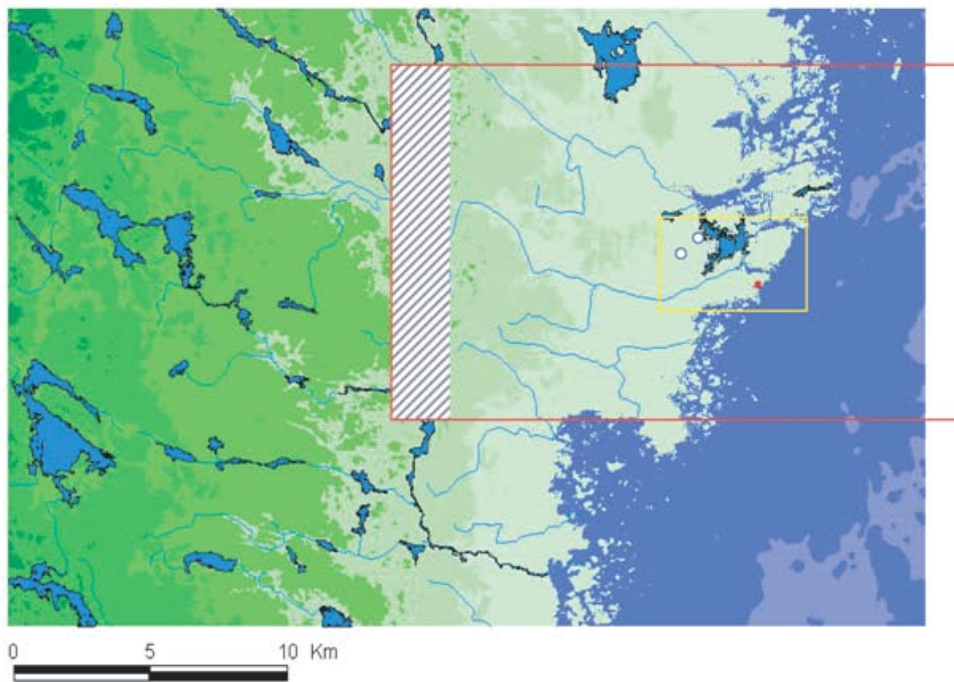
Present-day: 2,000 AD ; S = 0.6 (0.7) %

Water level above present datum = 0 masl

Shifted location of the upstream boundary of the model domain
to match the location of the regional surface water divide

*Figure 3-15. Schematic illustration in plan view of the differences in model domain/boundary
condition between Models #5 (full size) and 8 (reduced).*

3.6 Topographic data and model domain

Topographic data was supplied on two scales, 50 m and 10 m. Since the 10 m data covered the entire regional-scale model area defined in the TD, this data set was used both to define the model area as well as to set the topography of the top surface. Figure 3-16 shows an overview of the topographic data and surface water divides along with the regional model domain as proposed in the TD. As already mentioned the grid resolution was set to 100 m in the horizontal directions in accordance with the TD 1.5.

Figure 3-17 shows the topography and bathymetry of the 10 m data set. The maximum and minimum elevations within the regional model area are c 50 masl and c (–30) masl, respectively. It is noted that the elevation scale shown in the figure is quite exaggerated.
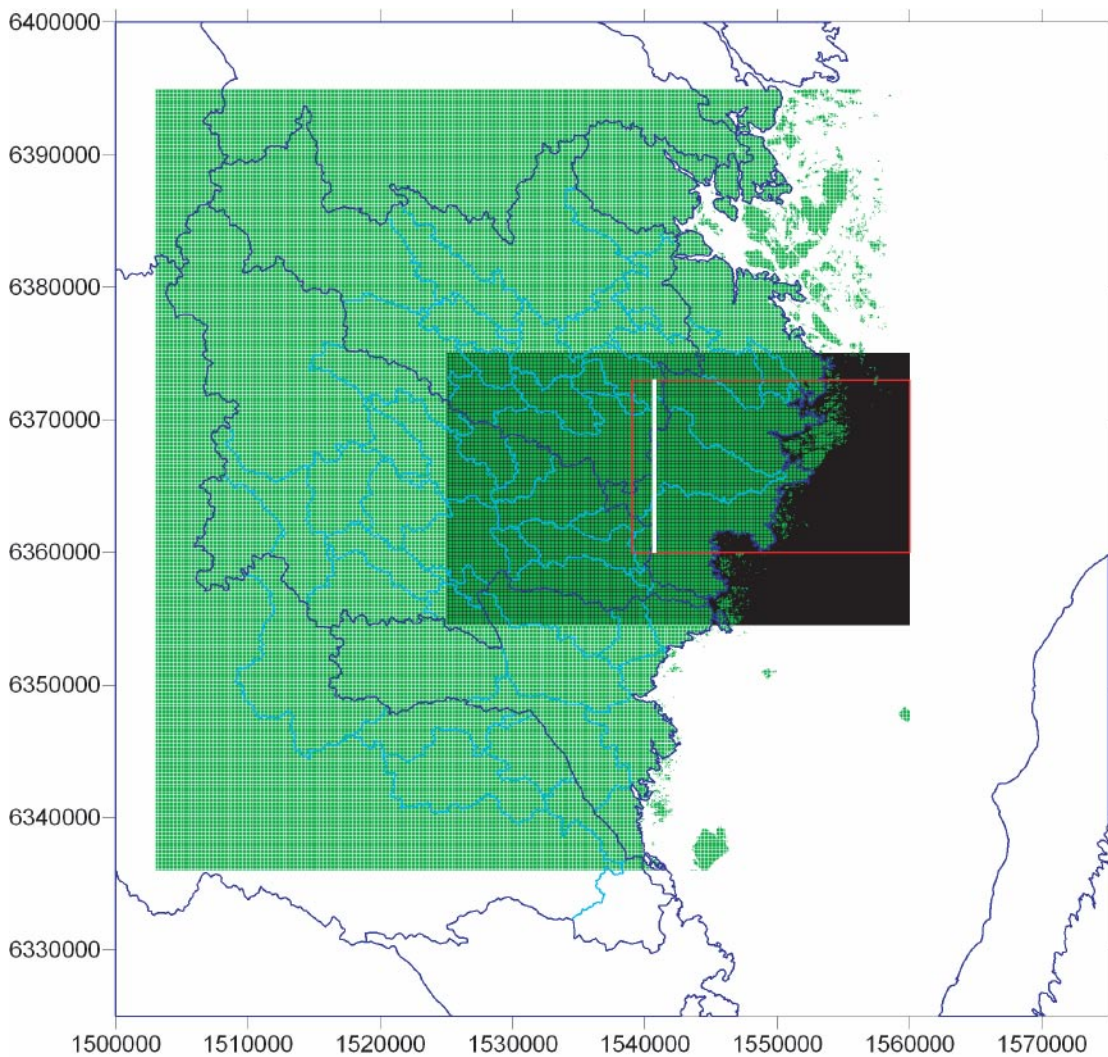
Figure 3-16. *Overview of available topographic data: 10 m grid (dark green), 50 m grid (light green), SMHI's regional water divides (dark blue), SMHI's local water divides (light blue), and the suggested regional-scale model area (red). The white line shows the location of the western boundary of smaller regional model domain studied in Model #8.*
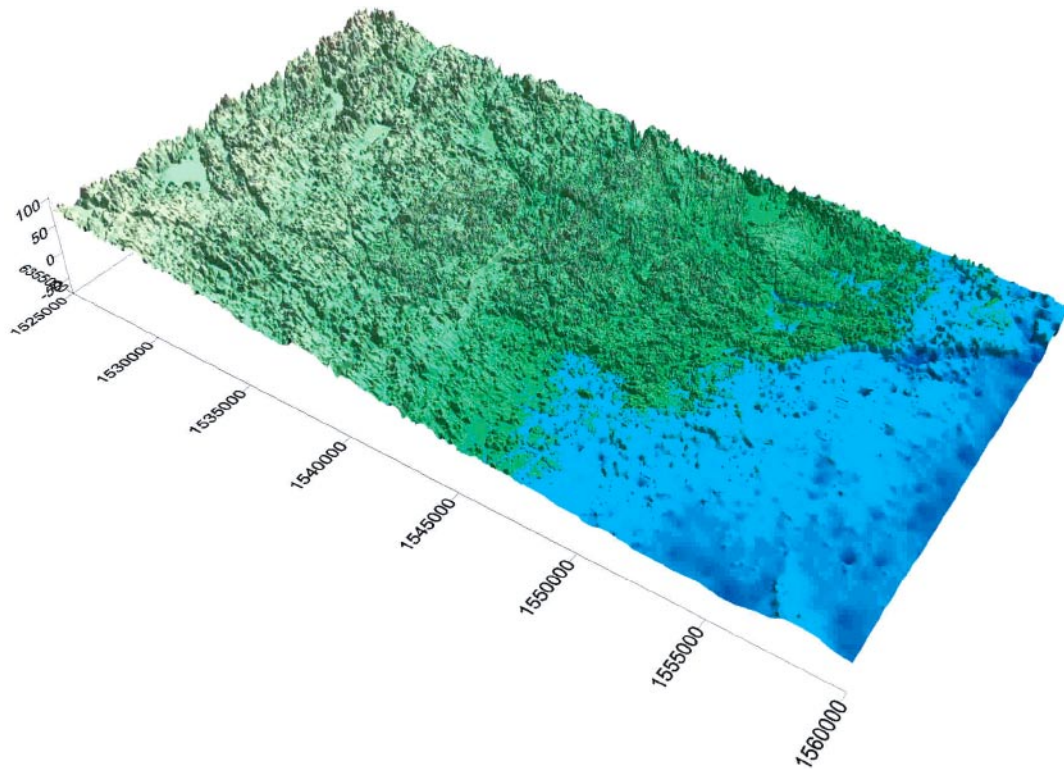
Figure 3-17. *Topography and bathymetry of the 10 m data set. The elevations are exaggerated. The maximum and minimum elevations are c 50 masl and c (–30) masl, respectively.*

3.7   Deliverables of groundwater flow

A number of deliverables are specified in the TD 1.5. In terms of developing the understanding of the palaeo-hydrogeological situation at the site, the following results were requested:

- Visualisations showing the transient evolution of the groundwater salinity in 3 W-E profiles (parallel to the regional model boundaries) and in one N-S profile through KLX01. Figures showing the groundwater salinity for the same section at three different time slices: 5,000BC; 0 BC; 2,000AD.

- Visualisation showing the present-day salinity distribution between (–2,100) masl and ground surface with a vertical W-E cross-section sweeping from north to south.

- Figures showing the present-day groundwater salinity distribution at (–10), (–100), (–500) and (–1,000) masl. Figures showing the present day Darcy flux component in the z-direction at (–10), (–100), (–500) and (–1,000) masl and the average value of the Darcy flux component in the z-direction as a function of depth.

Due to practical reasons as well as time constraints it was not possible to incorporate visualisations from all simulations in the report.

The visualisations shown in the report treat above all the present-day distribution of the mobile groundwater salinity in W-E profiles running through the locations of the two deep core drilled boreholes KLX01, c (–1,100) masl, and KLX02, c (–1,700) masl. The borehole locations are indicated in Figure 1-1 and Figure 1-2.

39

Also treated in this study was the advection of different water types, i.e. water parcels of conceptually different origin (in space and time). The simulated advection of the considered water types was governed by the transient solution of the variable-density groundwater flow.

The considered water types were conceptually thought to represent:

1. Old saline groundwater at depth (in study simplistically denoted by "Brine").
2. Glacial groundwater/Baltic Ice Lake water (fresh).
3. Yoldia Sea water (slightly brackish).
4. Ancylus Lake water (fresh).
5. Littorina Sea water (clearly brackish).
6. Meteoric water (fresh).
7. Baltic Sea water (slightly brackish).

3.8   Deliverables of particle tracking

Additional results were required to assess the implications for performance measures relating to safety assessment. For instance, using the velocity field at 2,000 AD particles were released at (–500) masl distributed over the Simpevarp subarea and the Laxemar subarea, respectively. The location of the two subareas is shown in Figure 1-1 and Figure 1-2.

For each subarea statistics, graphs and pictures for all cases were produced showing the:

- Advective travel times t_w of all particles.
- The Darcy flux at the starting positions.
- End values for the F-parameter (or F-quotient) for all particles plotted at the starting positions.
- Discharge positions of particles.

4 Calibration targets

4.1 General

As already mentioned the hydrogeochemical flow modelling performed in this study was purposely set to exploit hydrogeochemical data from the Laxemar subarea solely. Below we present the hydrogeochemical data used in the numerical simulations as calibration targets. In particular, we discuss the role of some issues that may affect the quality of the hydrogeochemical data and their potential impact on the objectives of the study.

The hydrogeochemical data considered in this study consisted originally of salinity data only. During the course of modelling the salinity data base was supplemented by hydrogeochemical information from the multivariate mixing and mass balance method (M3) /Laaksoharju et al. 1999a,b/. The latter type of information was matched with the water type simulations described in Chapter 3.

4.2 Salinity profiles in KLX01 and KLX02

The simulated salinity in the mobile pore volume was compared with the measured salinity profiles along the core drilled boreholes KLX01 and KLX02. The locations of the boreholes are shown in Figure 1-1 and Figure 1-2. The exact positions of the two boreholes are given in Table 4-1.
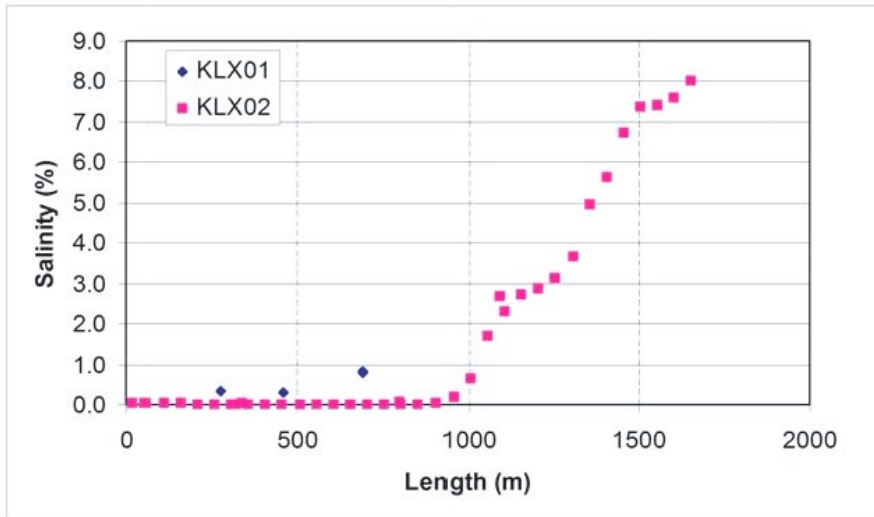
The measured salinity profiles along KLX01 and KLX02 are shown in Figure 4-1. The profiles were delivered to the modelling teams at the start of the numerical modelling.

Due to the limited information provided for KLX01 and the almost linear salinity increase in KLX02 below c (–1,000) masl it was decided in this study to use one calibration point for KLX01 and two calibration points for KLX02 for the comparison with simulations. Figure 4-2 shows the calibration points chosen.

Table 4-1. Coordinates of the used calibration targets, boreholes KLX01 and KLX02.

Name	X	Y	Ztop	Length	Bearing	Inclination
KLX01	1549923.093	6367485.516	16.77	1,077.99	358.119	–85.3
KLX02	1549224.090	6366768.985	18.40	1,700.50	9.119	–85.0

Figure 4-1. *Measured salinity profiles in KLX01 and KLX02 provided to the modelling teams at the start of the numerical modelling.*
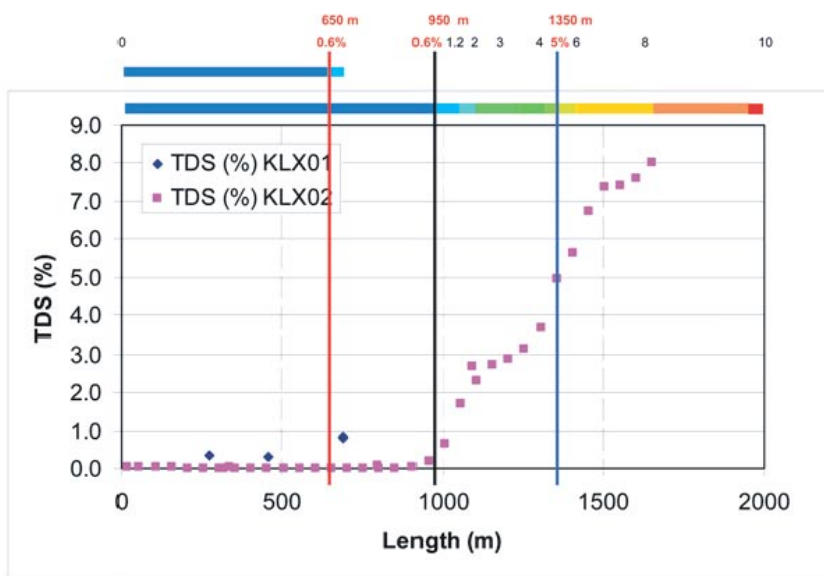
Calibration criteria : KLX01: 0.6% at c. 650 m
KLX02: 0.6% at c. 950 m
KLX02: 5% at c. 1350 m

Figure 4-2. *Selected calibration points for the comparison between simulated and measured salinities in core boreholes KLX01 and KLX02. The colouring of the line markers will be used as refrencences in the visualisations shown in Chapter 6.*

4.3   Water types

The aforementioned water type simulations were compared with calculated values based on the multivariate mixing and mass balance method (M3) /Laaksoharju et al. 1999a/. The M3 method is based on a principal component analysis of the chemical composition of water samples. It is used by SKB in many projects to trace the origin of groundwater, to calculate the mixing proportions of different end-members and for mass balance calculations (reactions with the bedrock) /Laaksoharju et al. 1999b/.

The mixing proportions of different end-members are of particular interest for the water type simulations conducted in this study. The end-members used in the M3 modelling are defined by their different chemical signatures (composition of chemical constituents). Among the different end-members we note, in particular, the definition of Glacial water, Littorina Sea water, Meteoric water (precipitation), Baltic Sea water and Brine type high-salinity water.

It is noted that a heuristic reasoning was adopted while exploring the possibilities for matching the results from the water type simulations in this study with the M3 results available for KLX02. The M3 results for KLX02 are shown in Figure 4-3 and were obtained upon request from /Marcus Laaksoharju, written comm, 2004/.

The M3 results shown in Figure 4-3 suggest that the water samples analysed consist mainly three end-members, Meteoric water, Glacial water and Brine. The meteoric water dominate the M3 calculations down to c (–1,000) masl. Between c (–1,000) masl and c (–1,500) masl there is a significant amount of both Glacial water and Brine in the water samples according to the M3 results. By comparing Figure 4-3 with the salinity profile for KLX02 shown in Figure 4-1 it is noted that salinities up to c 6% may contain significant fractions of Glacial water according to the M3 results.
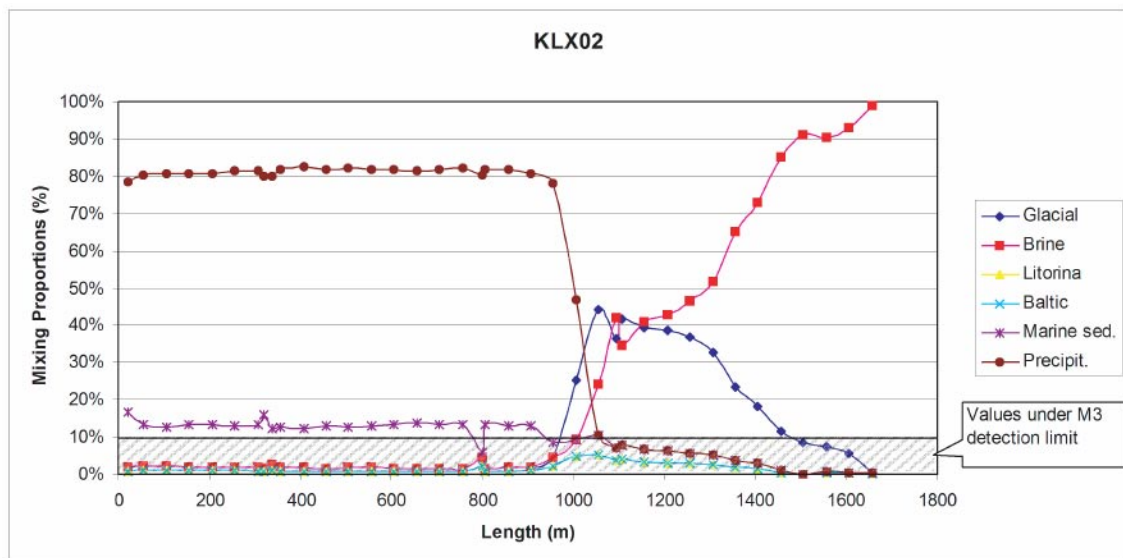

Figure 4-3. M3 results for KLX02 /Marcus Laaksoharju, written comm, 2004/.

In conclusion, the M3 results shown in Figure 4-3 suggest that the body of Glacial water in the terrestrial part of the model domain was flushed out by Meteoric water as a result of the shoreline displacement and the subsequent outcropping of land. The present-day occurrence of Glacial water in Figure 4-3 is found in the transition zone between Meteoric water and Brine. A possible explanation for this occurrence is that the historic interface between Glacial water and Brine was not sharp when the Simpevarp area was freed from the ice cap. Another explanation is that the fracture network between the DDZs is not sufficiently well hydraulically connected and that stagnant volumes of isolated water types therefore exist in the bedrock.

An interesting result from the M3 results is the absence of Littorina water. As pointed out previously, the location of the deep core drilled borehole KLX02 was above the sea water level at the start of the Littorina period. The Littorina period began with a transgression which lasted for about 1,000 years. The simulated maximum water depth at the location of KLX01 is circa five metres and at KLX02 circa three metres. Hence, it may be concluded that Littorina Sea water has the possibility to recharge directly into bedrock at the Laxemar subarea, at least in the numerical model. The selected calibration points for the comparison between simulated water types and modelled mixing of end-member proportions in core borehole KLX02 are:

- 50% Brine at c 1,300 m.

- 10% Glacial water at c 950 m and 40% at c 1,150 m.

- 80% Meteoric water at c 950 m and 50% at 1,000 m.

4.4   Uncertainties

During the course of the numerical modelling it was concluded that it was difficult to match the salinity profiles in KLX01 and KLX02 shown in Figure 4-2 using the initial DFN (SDZ) intensity defined in the TD 1.5 (Model #1 in Table 3-4). The reason for this difficulty could of course be sought in the conceptualisation of fractured rock as a porous medium, or in the numerical model, e.g. an insufficient vertical and horizontal resolution in the mesh discretisation with regards to the short lateral distance between the two boreholes. Another explanation in turn, could be an inappropriate assumption regarding the initial salinity condition at the start of the simulation period.

One after the other these sources for uncertainty were incorporated into the sensitivity study through a number of model variations, see Table 3-4. Among these, a lower DFN (SDZ) intensity was found to the most important factor next to the treatment of the uppermost rock layer and the transmissivity of the DDZs.

In the follow-up discussions about uncertainties, the methods used for taking point water samples in KLX01 and KLX02 were examined. The reason for the discussion was the clear difference between the salinity profiles in KLX01 and KLX02. It was concluded that the water sampling in KLX01 was probably satisfactory (made between packers), whereas the water sampling in KLX02 was uncertain for a number of reasons. Among other things, it was discovered that different types of methods have been used and that the prerequisites for taking undisturbed point water samples were unsatisfactory. The borehole was drilled in the beginning of the 90's and has been left open for long time periods, i.e. without inflated packers at the fracture zone intersections. Thus, data above the salinity interface are considered more uncertain..

Posterior to the modelling work reported here more data have been obtained for KLX01. This information has not been accounted for in the sensitivity analysis. For the sake of clarity, however, the M3 results of the water samples taken in KLX01 are shown in Figure 4-4. The results are not sufficiently addressed in this study to allow for comments, but it is noted that Littorina water was not detected by the M3 modelling and that the flushing of Glacial water by Meteoric water is not as extensive as for KLX02. Perhaps a valid comment here is that borehole KLX01 is located closer to the coast than KLX02.

The additional information for KLX01 also concerns the salinity profile. The values provided for the calibration are shown in Figure 4-1. However, there are more measurements at greater depths. The additional information was presented, e.g. in the documentation of the V1.1 Preliminary Site Description of the Forsmark area /SKB, 2004/. For the sake of clarity, it is shown also in Figure 4-5. The data in this figure are not sufficiently addressed in this study to allow for comments, but it is noted that besides more data for KLX01 the figure also contains more data for KLX02 (representing different methods) and data from the Olkiluoto and Forsmark areas.

It may be concluded that the calibration carried out in this study was made on an incomplete data set for KLX01 and on an uncertain data set for KLX02.

I addition to the above uncertainties it is noted that the M3 calculations has a detection threshold of 0.1 (10%) and that the maximum uncertainty in any calculated value is of the order ± 0.1 ($\pm 10\%$). Further, the representation of a borehole in the numerical flow model is limited by the grid resolution which is 100 by 100 m in the horizontal directions, whereas the diameter of a cored borehole is 0.076 m. Hence, there comparison between simulated concentrations on a 100 m grid requires a considerable amount of homogeneity in the water chemistry in order to allow for comparisons with borehole data, see Figure 4-6.
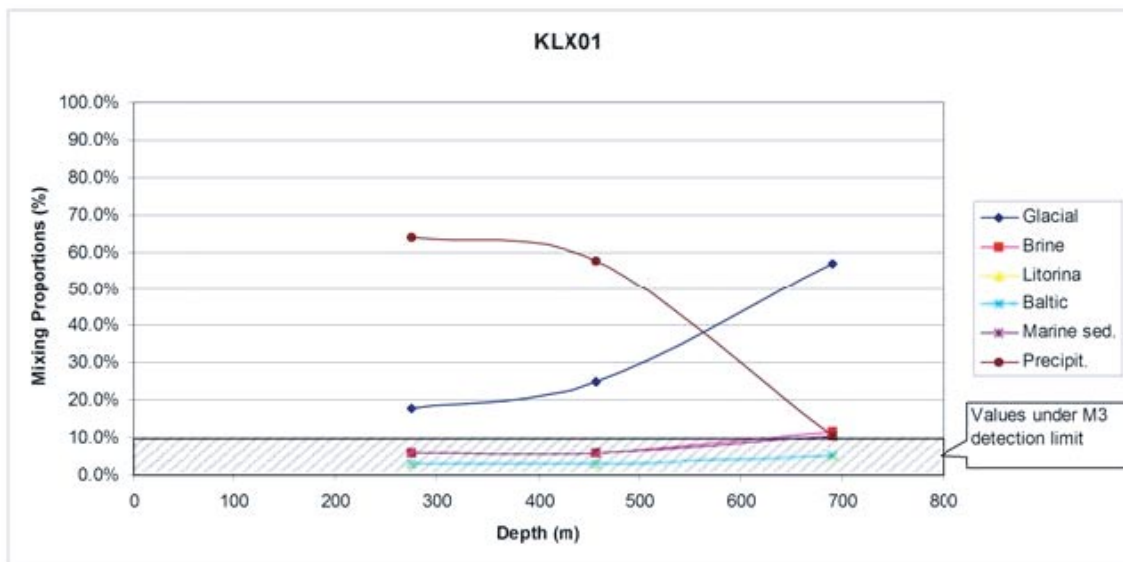
Figure 4-4. *M3 results for KLX01 /Marcus Laaksoharju, pers comm, 2004/.*
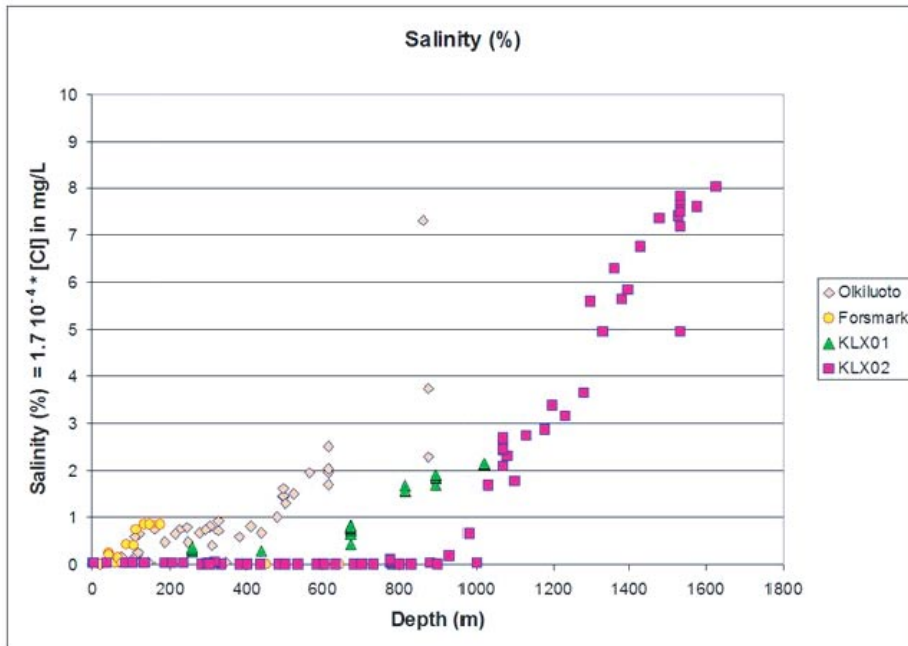
Figure 4-5. *Measured salinity profiles in KLX01 and KLX02 together with data from the Olkiluoto and Forsmark areas /SKB, 2004/.*
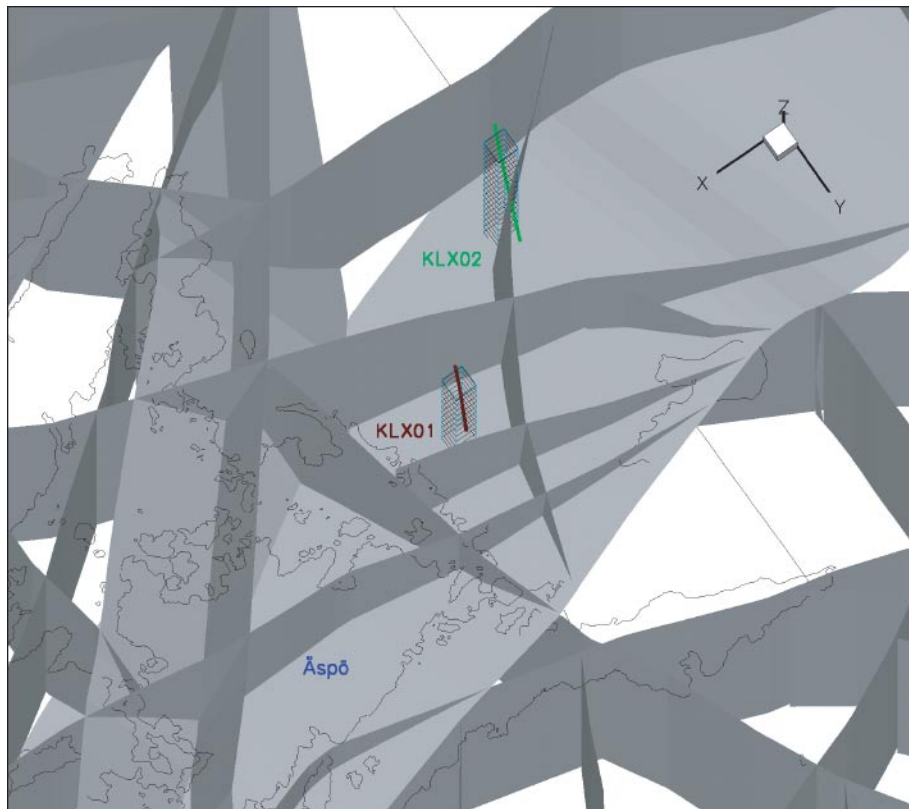
Figure 4-6. *View of the coastal area between Äspö and Laxemar. Gray shades represent the V0 DDZs. The layered columns circumventing the partially shown boreholes KLX01 and KLX02 are "borehole grid cells", i.e. the grid cells that are closest to inclined boreholes.*

5 Transient flow and salinity simulations

5.1 General

As already mentioned in Section 3.4 the simulations carried out with DarcyTools were performed to investigate the influence of conceptual and parameter uncertainties relating to initial and boundary conditions, DFN data interpretation, and background rock properties including properties affecting the rock matrix diffusion. Some of these simulations were along the original intensions of the TD 1.5, whereas others extended the scope of work significantly. The rationale for executing the extended work was to promote the inter-disciplinary discussions about the role of geological, hydrogeochemical and hydrogeological parameter uncertainties.

In what follows below we treat the model's sensitivity to the following topics:
- the conductivity of the uppermost rock layer (Section 5.2),
- the initial position of the salinity interface (Section 5.3),
- a smaller regional model domain (Section 5.4),
- the deformation zone flow porosity (Section 5.5),
- the global capacity ratio (Section 5.6),
- the DFN (SDZ) realisation (Section 5.7),
- the magnitude of $T = T(L)$ of the DFN (Section 5.8), and
- the transmissivity of the DDZs (Section 5.9).

5.2 Sensitivity to the treatment of the uppermost rock layer

The conductivity setting proposed in the TD 1.5 concerning the uppermost rock layer significantly decreased the hydraulic contact of the deterministically modelled deformation zones with the transient top boundary conditions. In conclusion, a low conductivity resulted in a lower flushing rate, cf Table 3-2.

Figure 5-1 shows the simulated present-day salinity distribution for Models #3 and 5 along two profiles running through KLX01 and KLX02. The two profiles demonstrate the sensitivity to the treatment of the uppermost rock layer. Figure 5-2 and Figure 5-3 demonstrate the corresponding sensitivity of the different water types.
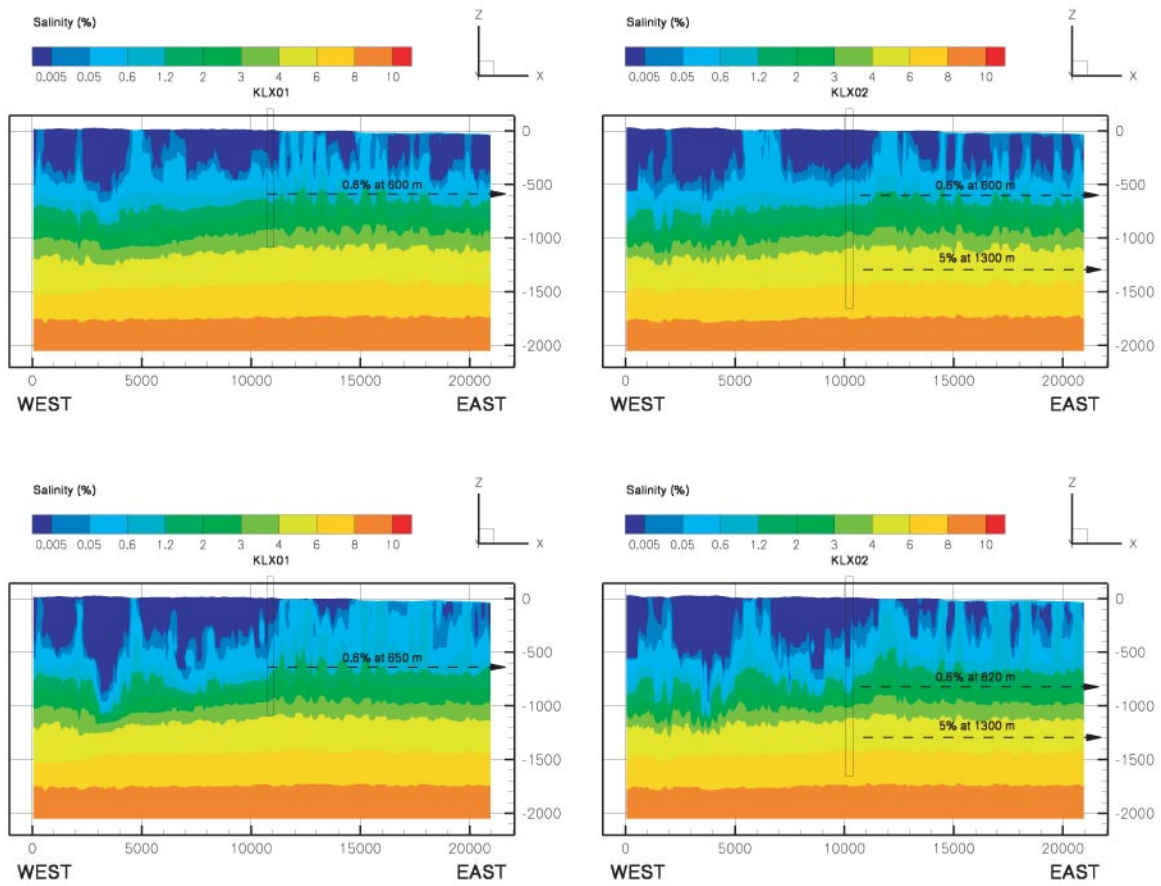
Figure 5-1. *Profiles running through KLX01 and KLX02 showing the sensitivity to the treatment of the uppermost rock layer. The top row shows the results for Model #3 and the bottom row for Model #5. The incorrectly modelled uppermost rock layer effectively prohibit sea water infiltration.*

48
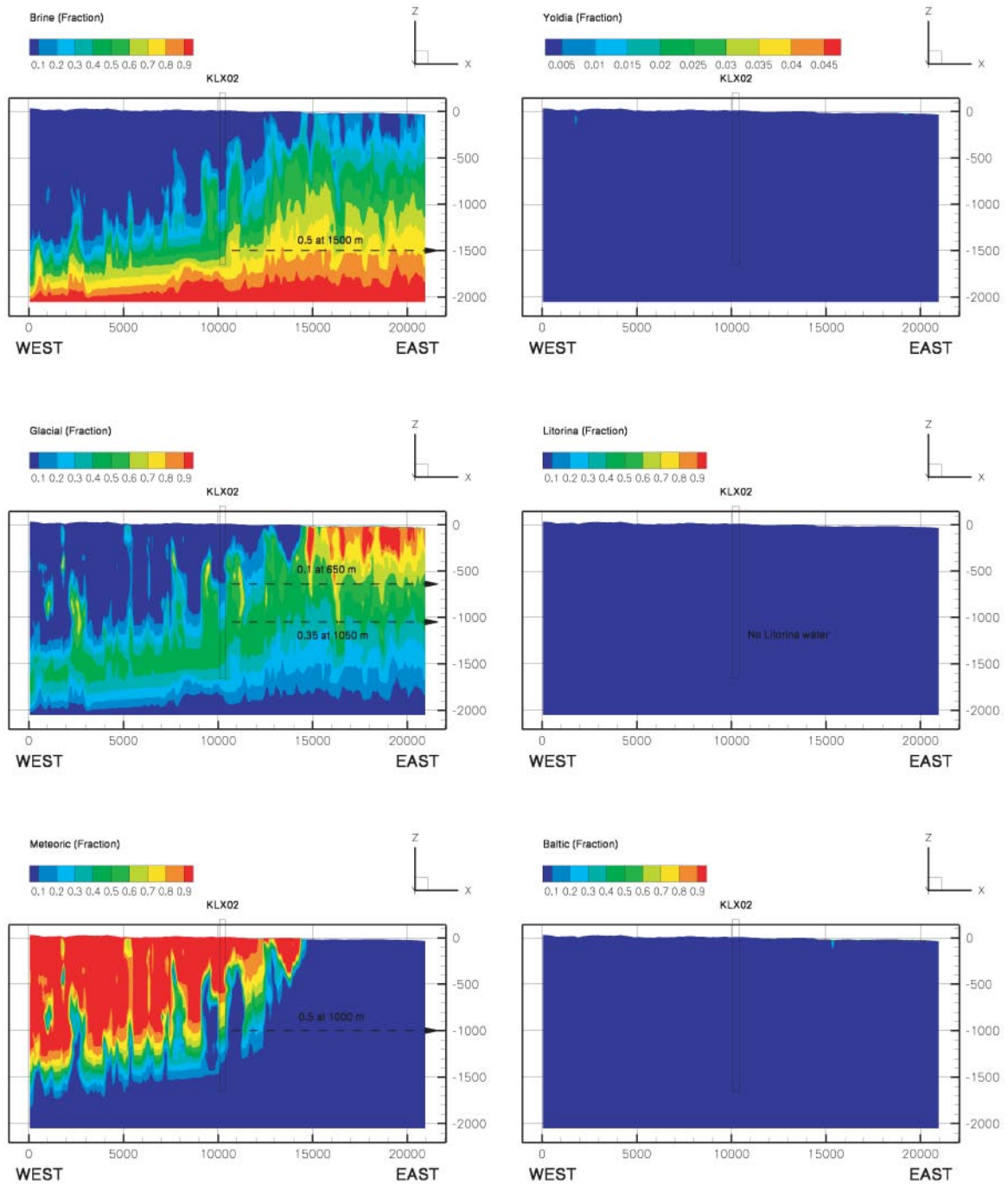
Figure 5-2. *Model #3. Visualisation of the fractional occurrence of Brine, Glacial water, Meteoric water (left column) and Yoldia Sea, Littorina Sea and Baltic Sea (right column) at 2,000 AD in a profile running from west to east through KLX02. The incorrectly modelled uppermost rock layer effectively prohibit any infiltration of sea water (Yoldia, Littorina and Baltic).*
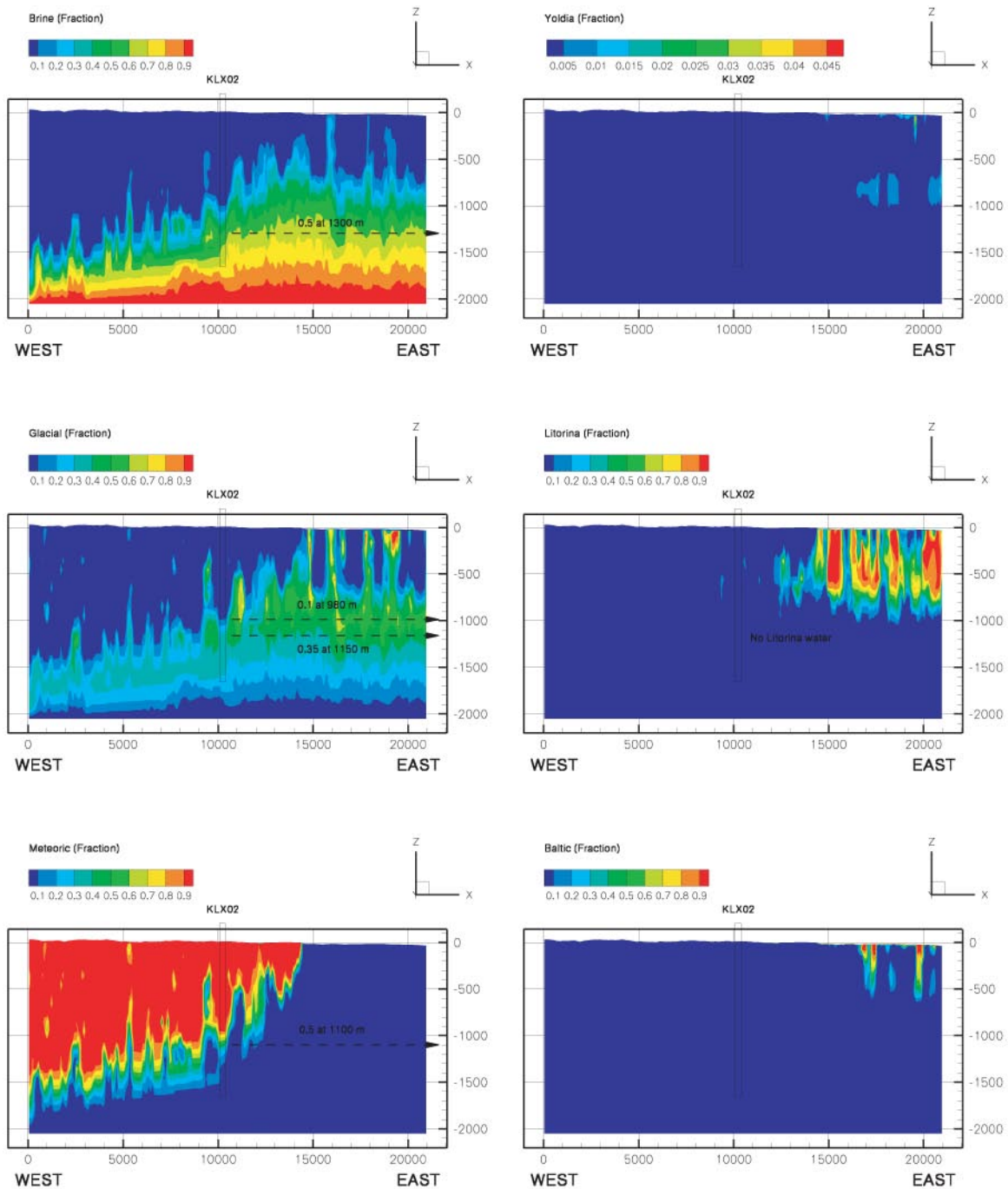
Figure 5-3. *Model#5. Visualisation of the fractional occurrence of Brine, Glacial water, Meteoric water (left column) and Yoldia Sea, Littorina Sea and Baltic Sea (right column) at 2,000 AD in a profile running from west to east through KLX02.*

Figure 5-4 shows the computed mean recharge rates into the bedrock versus depth for the two subareas, Simpevarp and Laxemar. The recharge rates were defined as the sum of all downward fluxes normalised to the total areas of the two subareas, respectively. In Model #3 the hydraulic conductivity of the uppermost rock layer was fixed to $1 \cdot 10^{-9}$ m/s, whereas in Model #5 there were was no limit on the maximum value, i.e. $> 1 \cdot 10^{-9}$ m/s. The simulations suggest a difference of about one order of magnitude between the models down to c (–500) masl. At (–1,000) masl the difference appears to even out, which suggests that the body of the flow in the model occurs within the uppermost one kilometre of the bedrock.

The mean recharge rate across the top boundary into the bedrock is c 8–12 mm for Model #5. The annual mean specific runoff in Southeast Sweden is estimated to be c 100–200 mm/y /Antal et al. 1998/. In conclusion, the simulated mean recharge across the top surface into the bedrock for Model #5 is c 5–10% of the annual mean specific runoff. At repository depth the mean recharge rate decreased to c 1%. As a comparison /Holmén et al. 2003/ concluded that only a small fraction, 1–2%, of the annual mean specific runoff can be expected to reach greater depths in crystalline rock.
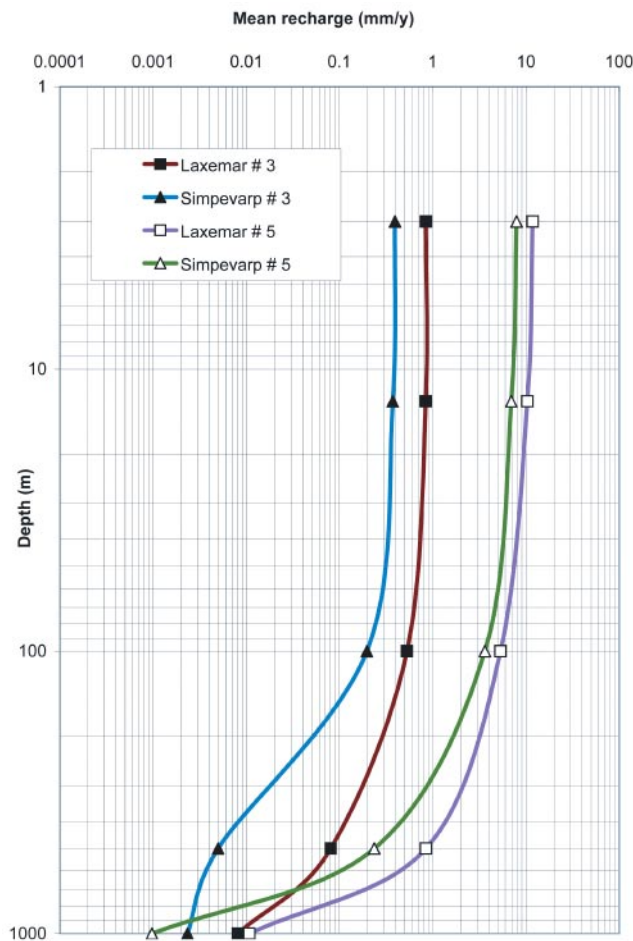
Figure 5-4. *Simulated present-day recharge profiles to the bedrock at the Laxemar and Simpevarp subareas versus depth. The uppermost rock layer is treated as homogeneous and isotropic in Model #3 and heterogeneous and anisotropic in Model #5.*

We end this section by concluding that the treatment of the uppermost rock layer has a strong impact on the palaeo-hydrogeological question. The simulations conducted show that a poor contact with surface boundary condition results in very little density-driven infiltration from the Yoldia Sea, Littorina Sea and the Baltic Sea. The effect on the particle tracking and the flow related transport parameters are commented in Chapter 6.

Before proceeding to the remaining sections of this chapter the spatial distribution of recharge and discharge within the Laxemar and Simpevarp subareas is visualised for Model #5 (Base Case). The simulation results are shown in Figure 5-5 through Figure 5-7. The figures show the areal distribution of recharge and discharge at different depths for the two subareas of interest. The simulation results suggest that recharging flow conditions occur at repository depth in Laxemar subarea in contrast to the Simpevarp subarea, which is predominantly subjected to discharging flow conditions.
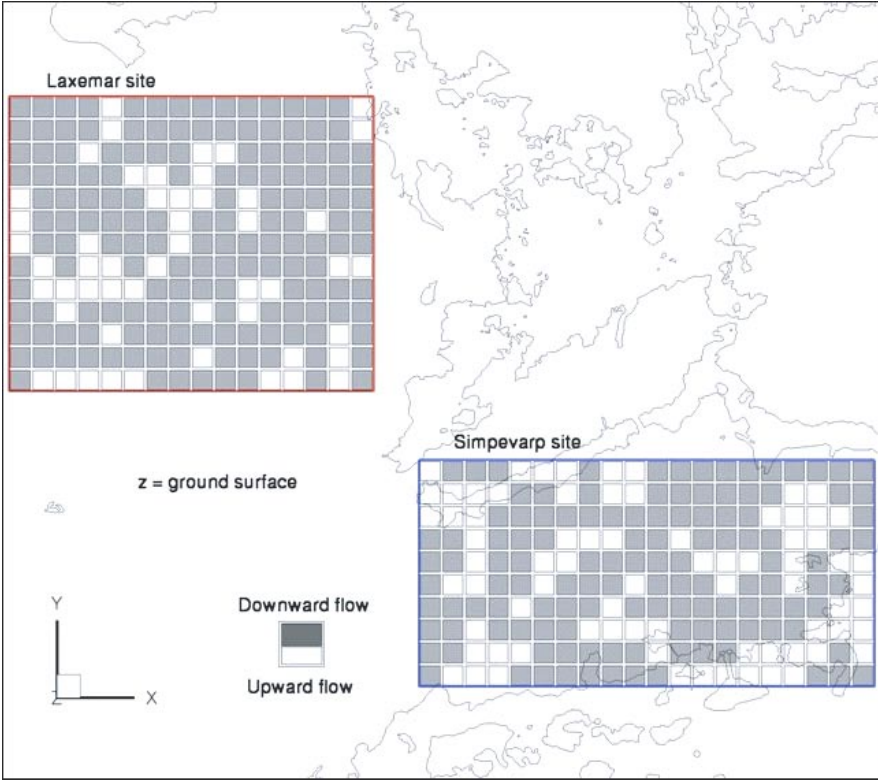
Figure 5-5. *Example visualisation of the areal distribution of recharge and discharge the Laxemar and Simpevarp subareas at ground surface.*
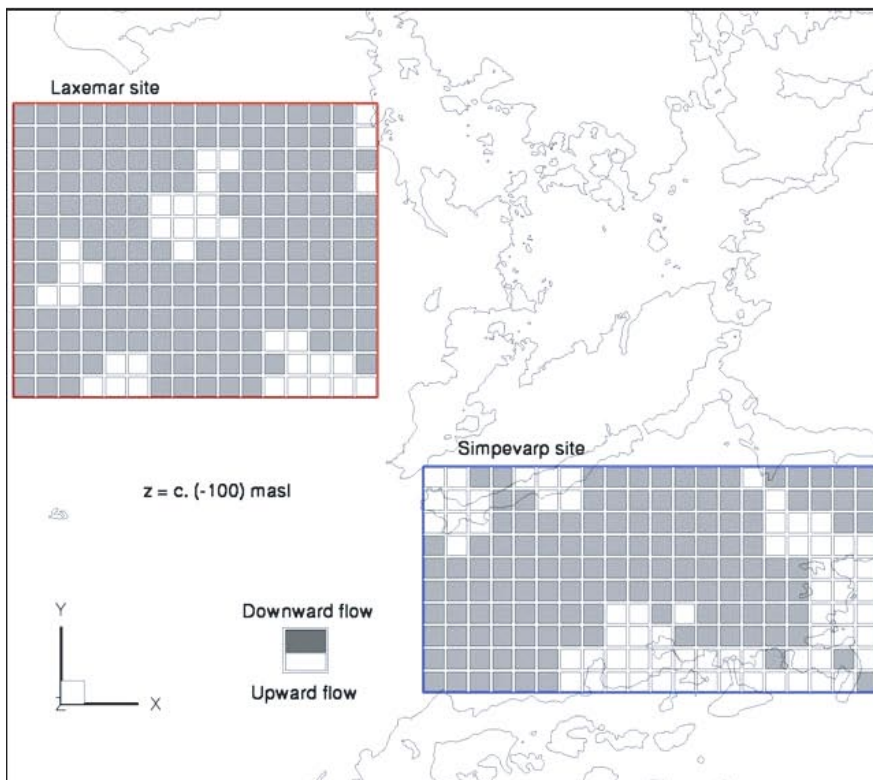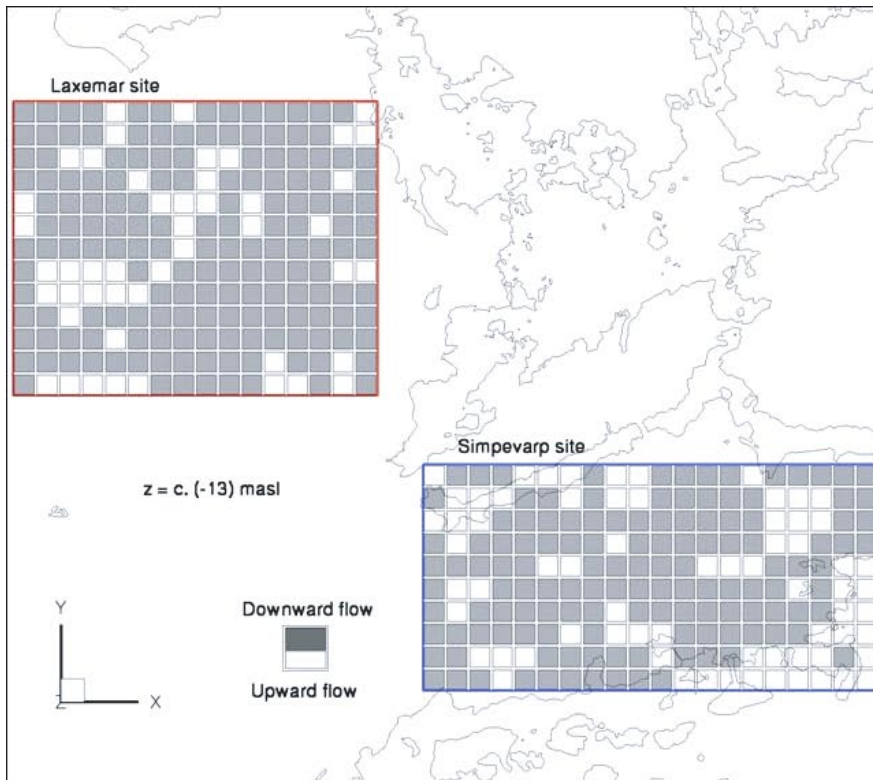
Figure 5-6. Example visualisation of the areal distribution of recharge and discharge the Laxemar and Simpevarp subareas at (–13) masl (top) and at (–100) masl (bottom).
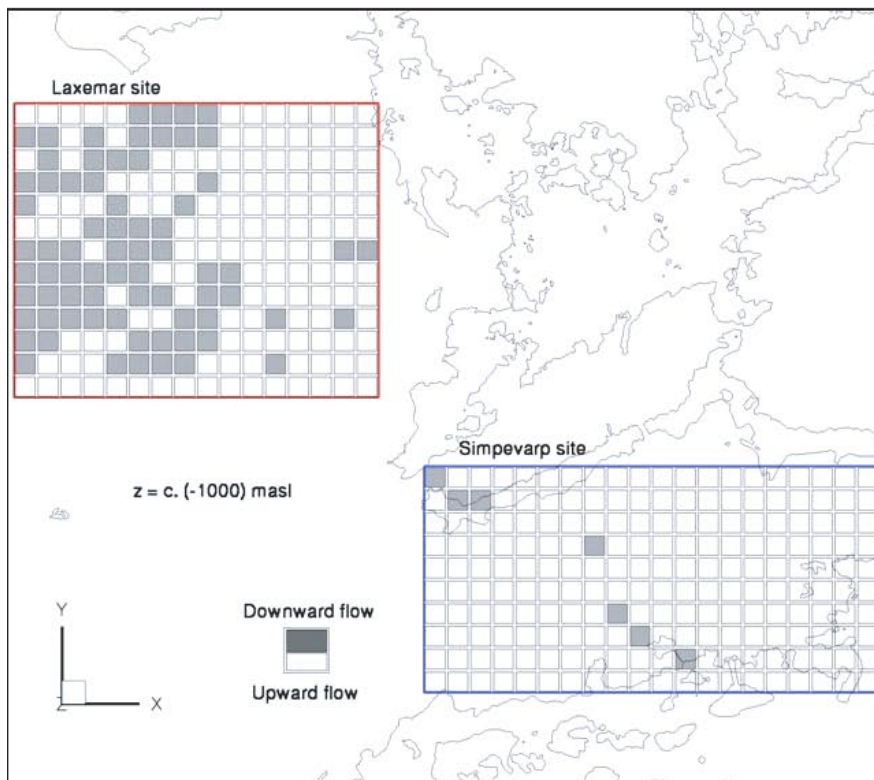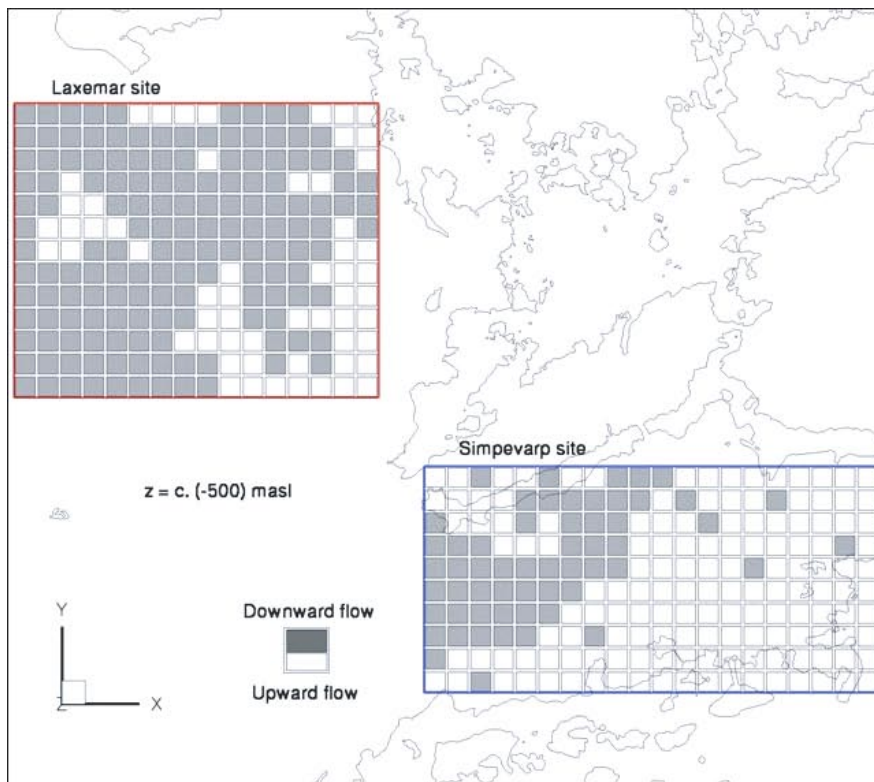
Figure 5-7. *Example visualisation of the areal distribution of recharge and discharge the Laxemar and Simpevarp subareas at (–500) masl (top) and at (–1,000) masl (bottom).*

54

5.3 Sensitivity to the initial position of the salinity interface

The calibration criteria discussed in Section 4.1 and Section 4.2, respectively, are shown in Figure 5-8 together with the initial salinity conditions for Models #5–7. The same DFN realisation was used in the three simulations. The locations of the two boreholes are indicated in the figures showing the results.

Figure 5-9 through Figure 5-12 demonstrate the sensitivity of the simulated salinity and the different water types to the assumption about the position of the initial salinity condition at 10,000 BC. The simulated flushing of the model area by the Littorina Sea is visualised for Model #5 in Figure 5-13 and Figure 5-14. Figure 5-15 shows simulated and measured conductivity profiles versus depth at the locations of the cored boreholes KLX01 and KLX02. No attempt was made in this study to calibrate the simulation to match the measured conductivities. The simulated conductivity values represent geometric means of the directional components on each level. The measured values were obtained by an integration of measurement results on a much smaller test scale, see /Follin et al. 2000/. It is also noted that both boreholes are intersected by DDZ, which strongly affect the simulated conductivities. KLX02, e.g. runs close to one of the deterministically modelled deformation zones.
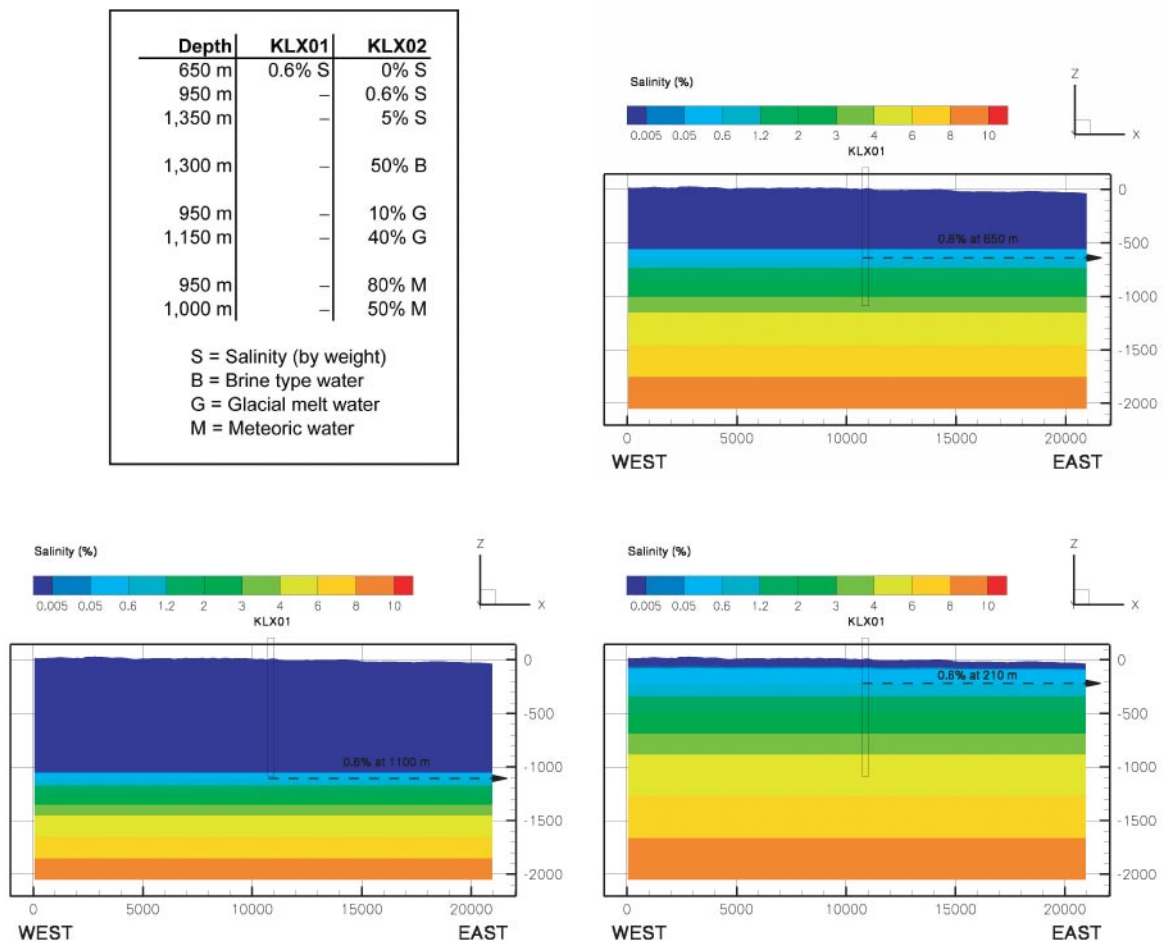
Figure 5-8. *Initial salinity conditions for Models # 5 (top), 6 (left) and 7 (right).*
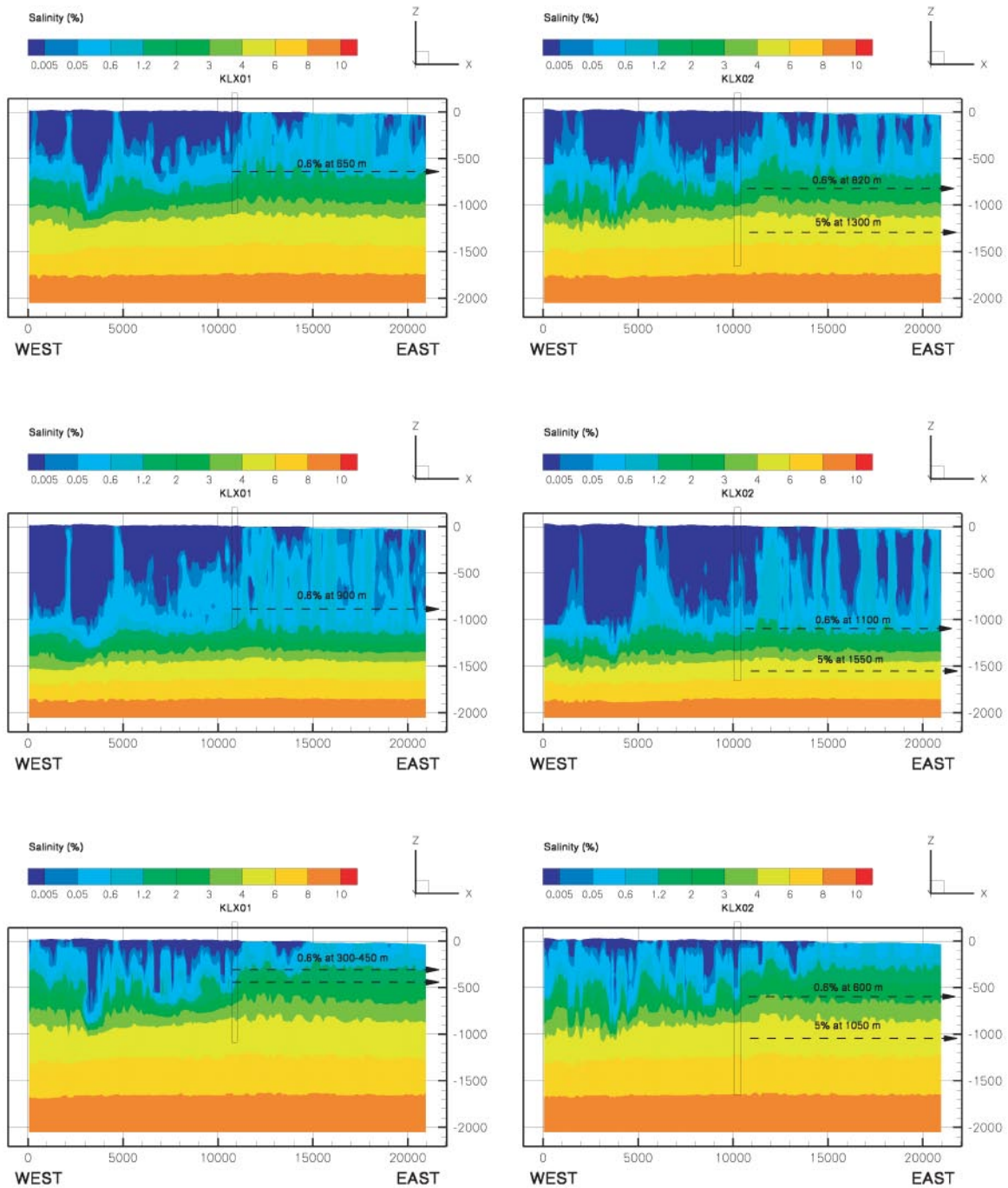
Figure 5-9. *Visualisation of the salinity in the groundwater at 2,000 AD in two parallel profiles running from west to east through the locations of the boreholes KLX01 (left column) and KLX02 (right column). The top row, the middle row and the bottom row show the results for Models #5–7, respectively.*
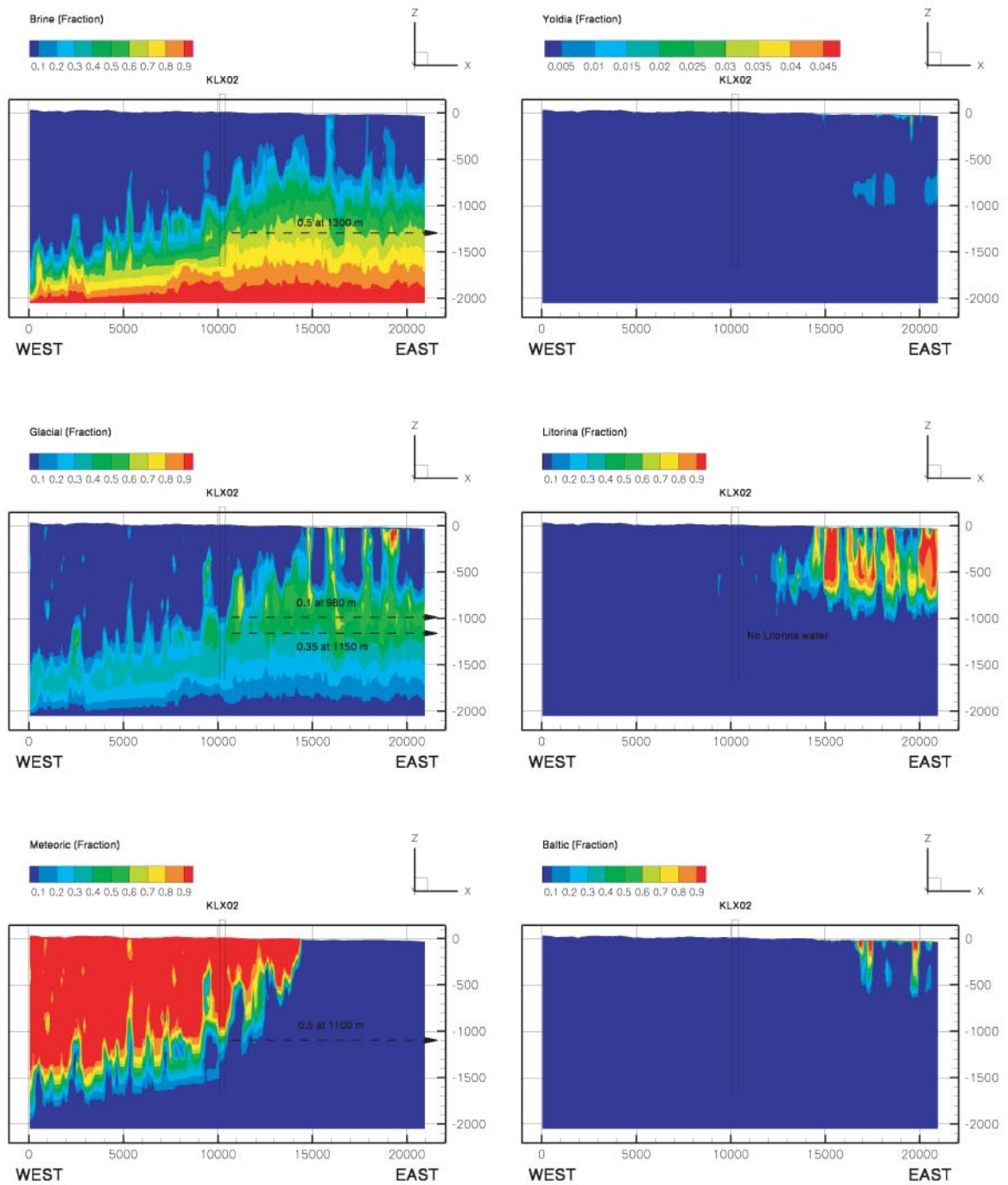
Figure 5-10. *Model #5. Visualisation of the fractional occurrence of Brine, Glacial water, Meteoric water (left column) and Yoldia Sea, Littorina Sea and Baltic Sea (right column) at 2,000 AD in a profile running from west to east through KLX02.*
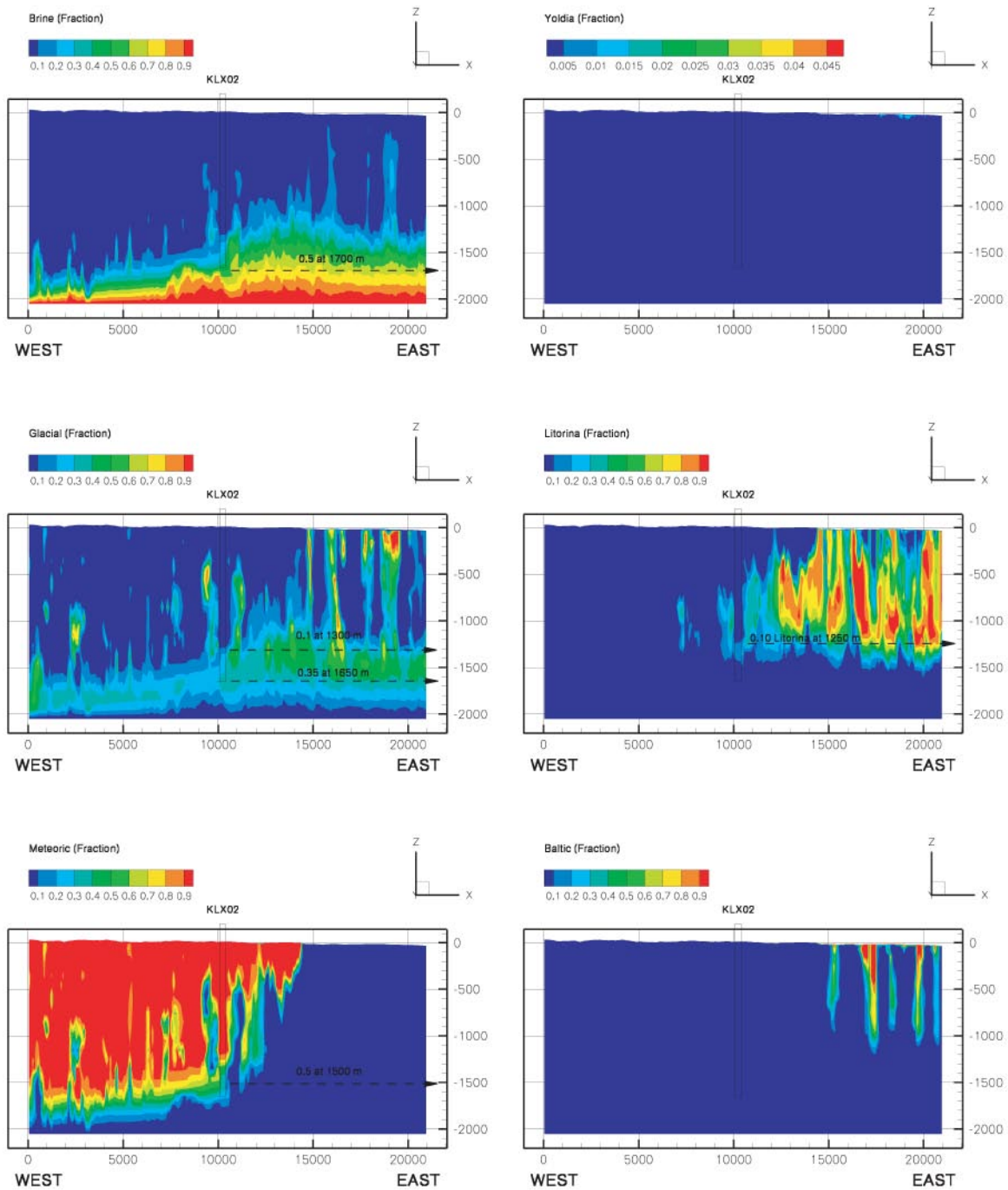
Figure 5-11. *Model #6. Visualisation of the fractional occurrence of Brine, Glacial water, Meteoric water (left column) and Yoldia Sea, Littorina Sea and Baltic Sea (right column) at 2,000 AD in a profile running from west to east through KLX02.*
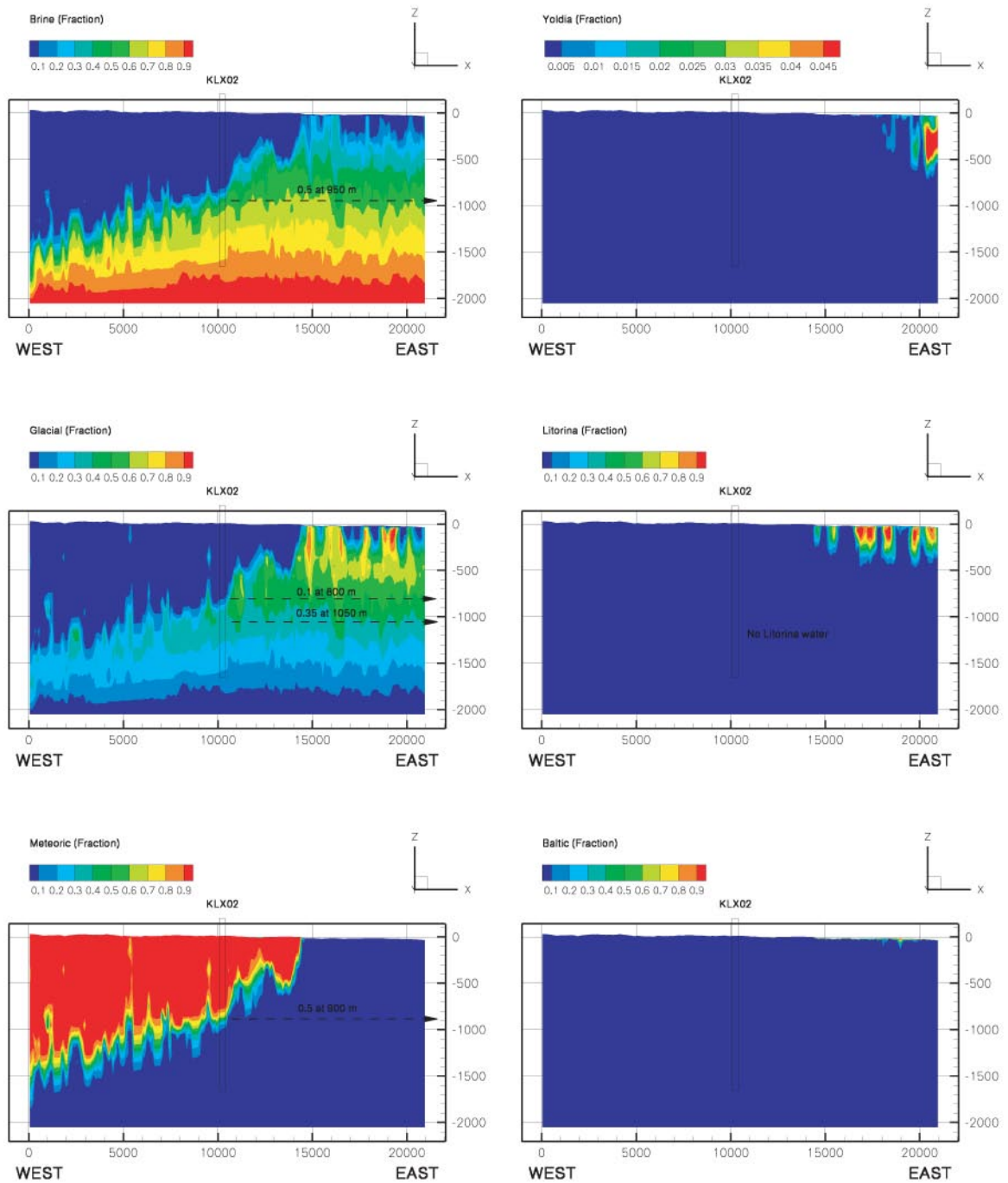
Figure 5-12. *Model #7. Visualisation of the fractional occurrence of Brine, Glacial water, Meteoric water (left column) and Yoldia Sea, Littorina Sea and Baltic Sea (right column) at 2,000 AD in a profile running from west to east through KLX02.*
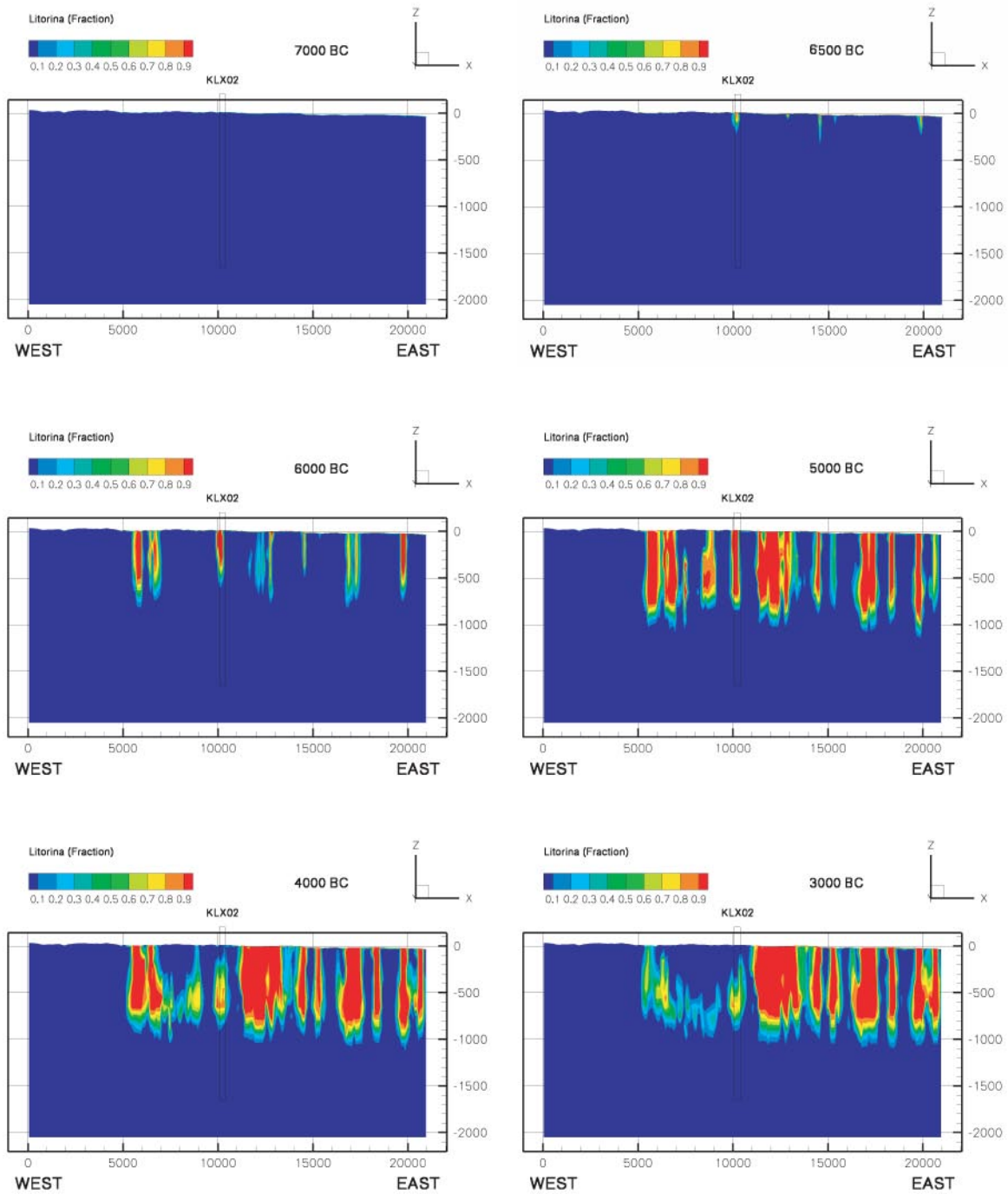
Figure 5-13. *Model #5. Visualisation of the simulated intrusion and subsequent flushing of Littorina Sea water between 7,000 BC and 3,000 BC.*
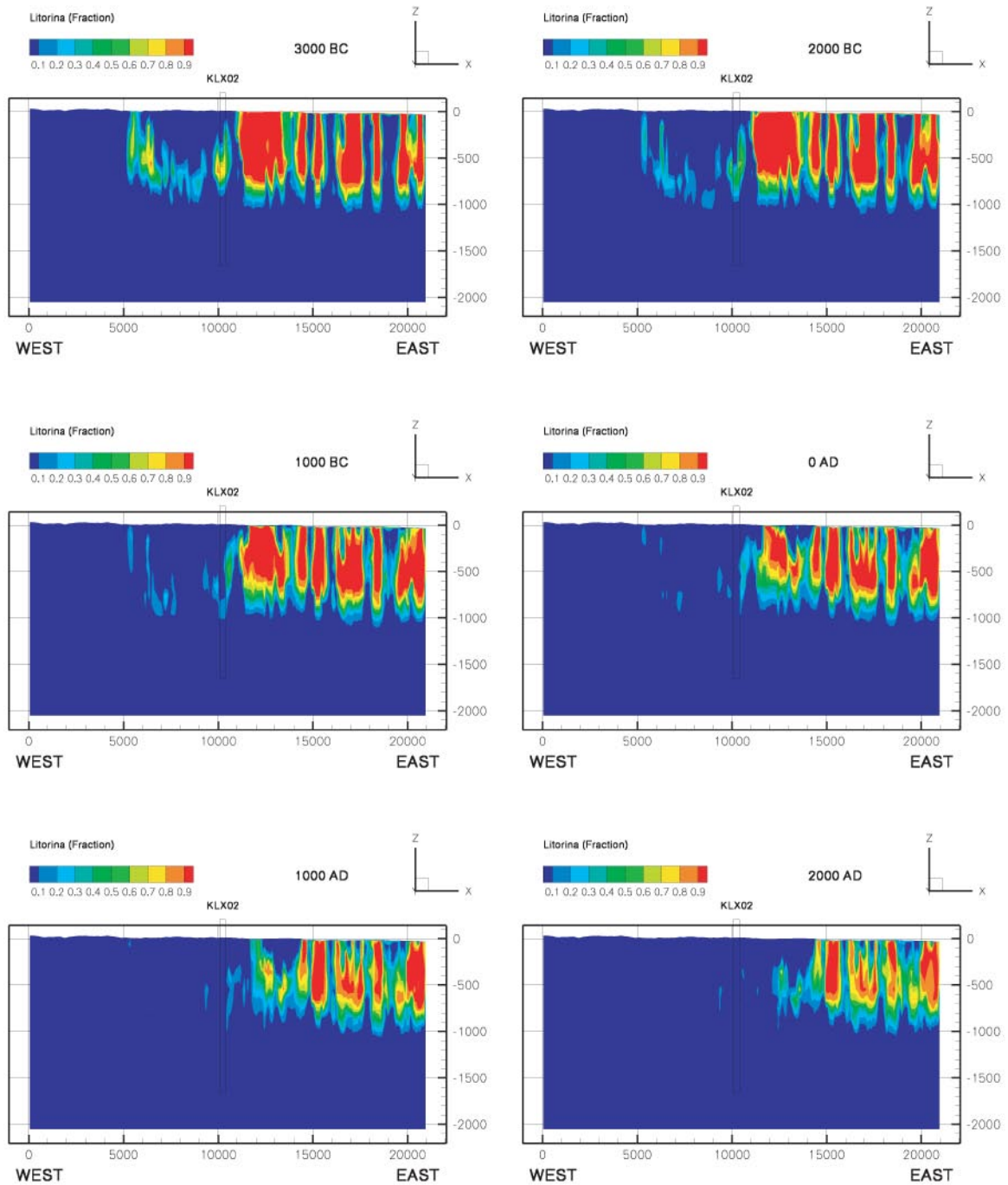
Figure 5-14. *Model #5. Visualisation of the simulated intrusion and subsequent flushing of Littorina Sea water between 3,000 BC and 2,000 AD.*
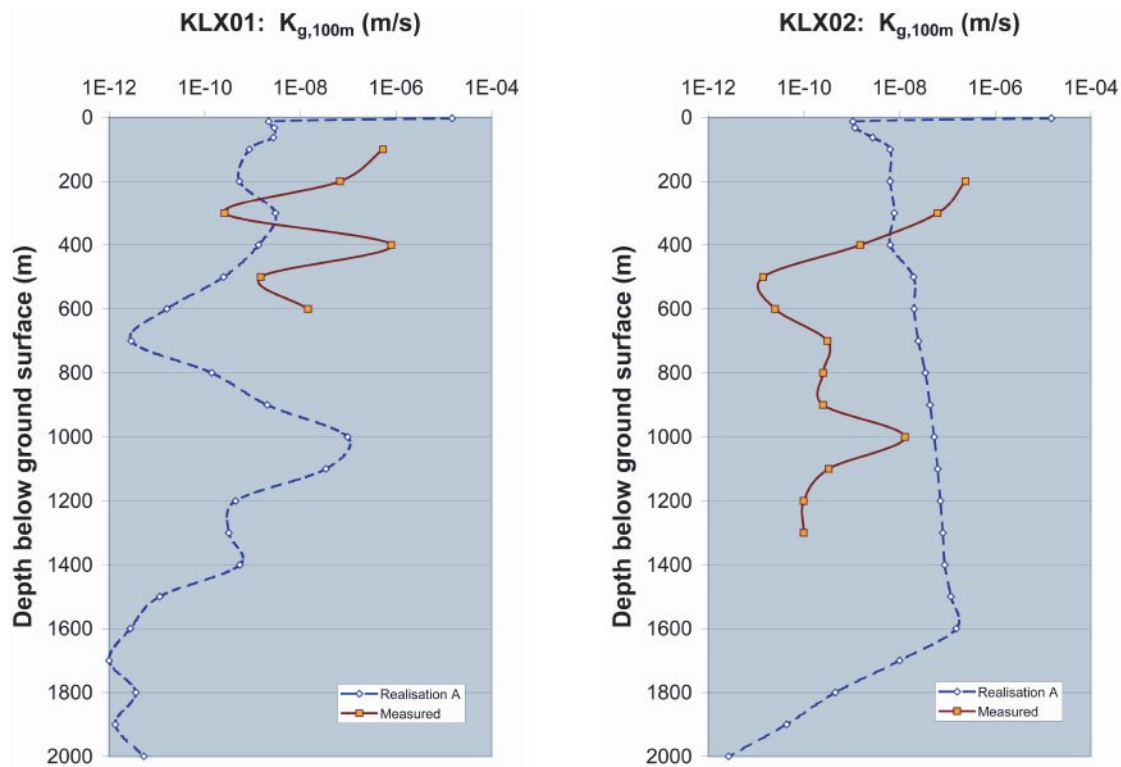
Figure 5-15. *Simulated and measured conductivity profiles versus depth at the locations of the cored boreholes KLX01 and KLX02. It is noted that no attempt was made in this study to calibrate the simulation to match the measured conductivities. The simulated conductivity values represent geometric means of the directional components on each level. The measured values were obtained by an integration of measurement results on a much smaller test scale, see /Follin et al. 2000/.*

The simulation results shown for Models #5–7 imply that:

- Both boreholes are intersected by deterministically modelled deformation zones, which strongly affect the simulated conductivities locally; KLX02 runs quite close to one of the deterministically modelled deformation zones and KLX01 is intersected by a deterministically modelled deformation zone between 900–1,100 metres below ground surface. Measured conductivities differ significantly from the simulated conductivities.

- Despite the significant deviation in hydraulic conductivity, the simulated DFN realisation in combination with the initial salinity position of Model #5 yield excellent matches with regards to the chosen calibration criteria for the groundwater salinity and the water types. In contrast, Models #6 and #7 yield poor results.

- The flushing of the computational grid is strongly affected by the outcrop and transmissivity of the deterministically modelled deformation. The maximum flushing depth of the Littorina Sea for Model #5 is c 1,000 m.

- The chosen DFN intensity yields an irregular flushing of the computational grid with isolated volumes of apparently anomalous water chemistry.

5.4 Sensitivity to a smaller regional model domain

The sensitivity to a smaller regional model domain was approximately studied in Model #8. By assigning very low values to the grid cell hydraulic conductivity and flow porosity within a limited part of the regional model domain, the effect of a "surface water divide/no flow boundary" was mimicked. The region with altered hydraulic properties encompassed all grid cells to the west of x = 2,600 m, which corresponds to c 12% of the regional model domain. The chosen region coincides with the existing regional surface water divide, see Figure 3-16. The values used were $1 \cdot 10^{-14}$ m/s for the hydraulic conductivity and $1 \cdot 10^{-7}$ for the flow porosity.

The motivation for using altered material properties instead of limiting the model domain physically was the desire to keep the (stochastic) DFN realisation unchanged in the active part of the model domain in order to allow for a direct comparison. That is, the deterministically and stochastically modelled deformation zones in Model #5 and #8 were identical. Figure 5-16 shows the simulation results for the two model runs.
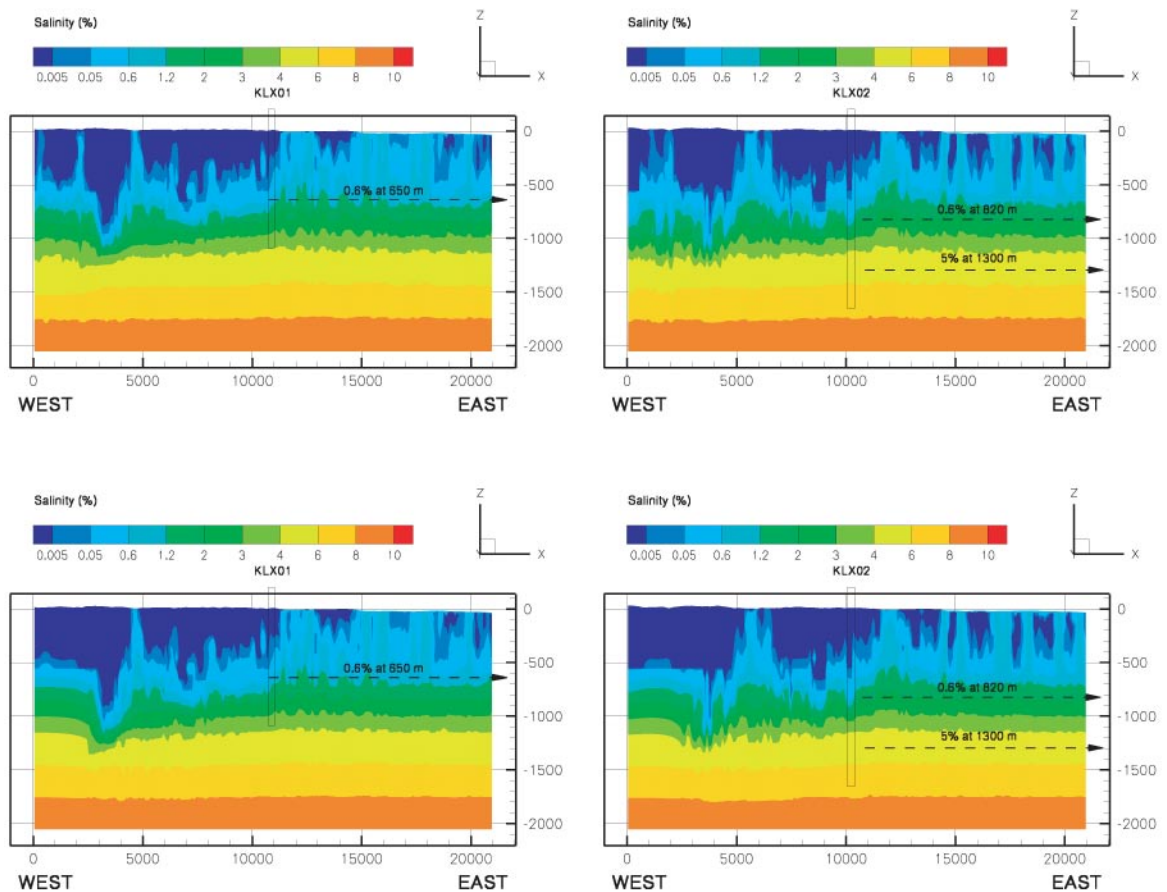
Figure 5-16. *Profiles running through KLX01 and KLX02 showing the sensitivity to altered material properties approximately micking the sensitivity to a smaller regional model domain. The top row shows the result for Model #5 and the bottom row for Model #8.*

The results shown in Figure 5-16 imply that the smaller model domain appears to be of little impact for the salinity distribution, i.e. the simulation results close to the boundary are almost identical for the two cases studied. The interpretation made here is that the geometry and hydraulic properties of the deterministically modelled deformation zones together with the local topography (top boundary condition) by and large govern the simulation results. The flow results show strong local flow cells. The effect on the particle tracking and the flow related transport parameters are commented in Chapter 7.

It is noteworthy , however, that the obtained results may only reflect the nature of the V0 DDZ model, which consists of more or less vertical DZs all of which have a fixed transmissivity at all depths. In addition, the water table follows the topographic variations.

5.5 Sensitivity to the deformation zone flow porosity

The hydraulic properties of the grid cells not intersected by deformation zones were tacitly modelled as a homogeneous and isotropic continuum of "background rock" in accordance with the specifications made in the TD 1.5. As mentioned in Section 2.3 the setting of "background rock" properties affected c 3.5% of the model domain volume in the case of lower deformation zone intensity (Model #3–14).

Table 5-1 shows the relative sensitivity of the global mean flow porosity of the regional model domain between (–100) masl and (–2,100) masl to the flow porosity values of the deformation zones and the "background rock", respectively.

The salinity distributions for the two values of the deformation zone flow porosity are shown in Figure 5-17. All other parameter values are unchanged. The differences are clearly visible despite the chosen scale of the images. However, the differences at the locations of the two boreholes KLX01 and KLXC02 are negligible.

The global mean flow porosity for Model #5 (left column in Figure 5-17) is five times greater than for Model #9, which means that there is five times more water of Glacial and Brine type at the start of the simulation period. In result, the difference in the deformation zone flow porosity affects the initial content of salt at 10,000 BC. As a consequence, the flushing of Model #5 differs from that of Model #9. The effect of these differences on the Darcy flux field, the particle tracking and the flow related transport parameters are commented in Chapter 7.

Table 5-1. Global mean grid cell flow porosity for the model domain between (–100) masl and (–2,100) masl as a function of (i) the flow porosity of the deterministic and stochastic deformation zones and (ii) the flow porosity of the "background rock" (i.e. grid cells not intersected by deterministic and/or stochastic deformation zones.

Deformation zone flow porosity	"Background rock" flow porosity	
	$1 \cdot 10^{-5}$	$1 \cdot 10^{-4}$
$1 \cdot 10^{-3}$	$7.6 \cdot 10^{-5}$	$7.9 \cdot 10^{-5}$
$5 \cdot 10^{-3}$	$3.8 \cdot 10^{-4}$	$3.8 \cdot 10^{-4}$
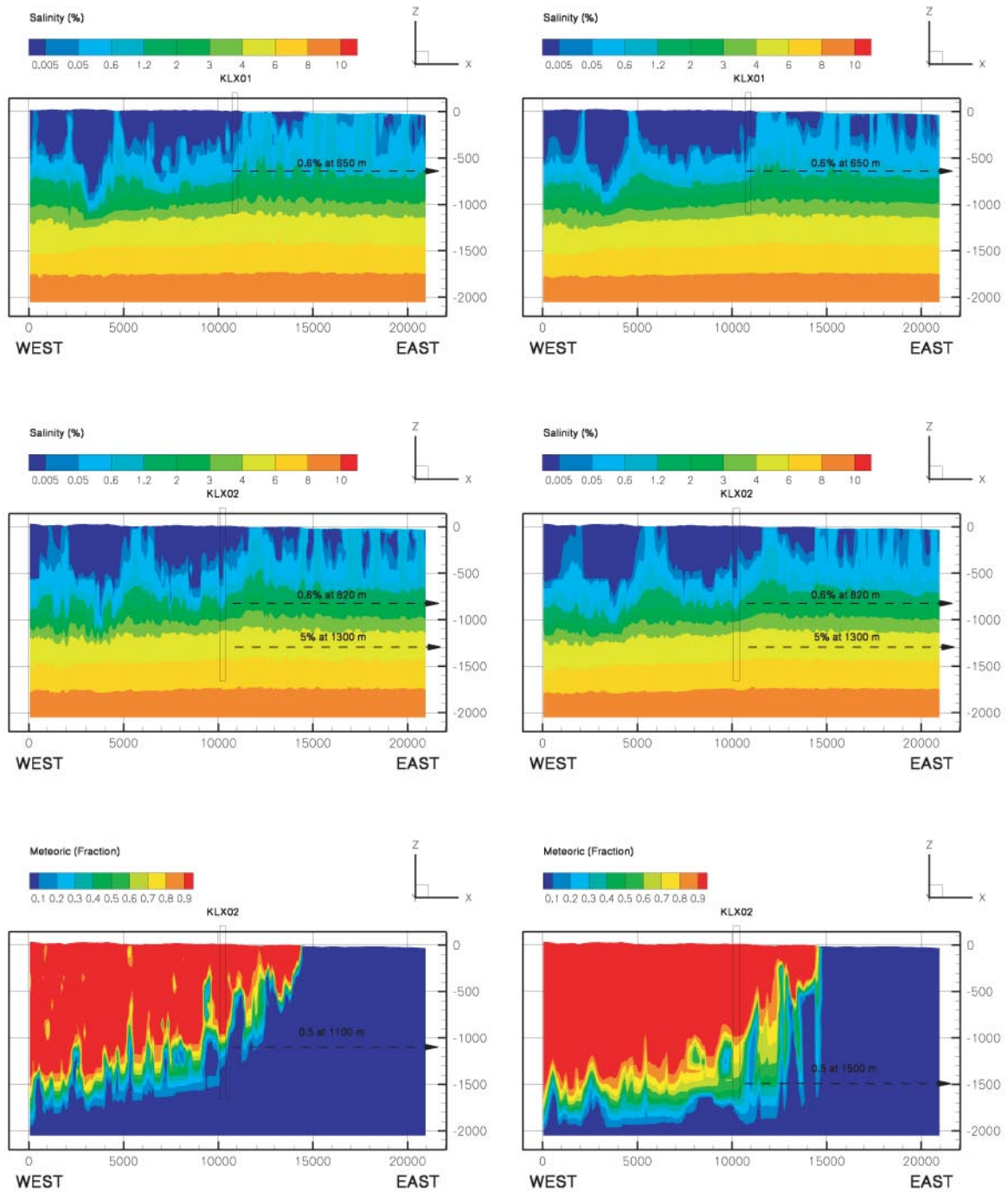
Figure 5-17. *Visualisation of the salinity in the groundwater as a function of the flow porosity of the deterministic fracture zones and the stochastic fractures. Left column: Salinity and Meteoric water distribution for Model #5. Right column: Salinity and Meteoric water distribution for Model #9.*

5.6   Sensitivity to the capacity ratio

The purpose of Figure 5-18 and Figure 5-19 is to demonstrate the functionality of the multi-rate diffusion model as implemented into DarcyTools 2.1. Both figures show results from a single DFN realisation. Figure 5-18 shows the salinity in the mobile pore volume for three values of the global capacity ratio, β_G =10, 20 and 50, corresponding to Models #5, 10 and 11. Figure 5-19 shows the salinity in the mobile pore and immobile pore volumes for Model #11.

The differences between the three model simulations are hard to detect in Figure 5-18 due to size of the insets. Notwithstanding, the simulation corresponding to Model #11 reveals that the greater the value of β_G, the more salinity is initially loaded into the immobile pore volume from the onset of the simulation. Consequently, the flushing of the salt in the mobile pore volume of Model #11is counteracted by the diffusion of salt out of the immobile pore volume into the mobile for a longer period of time.
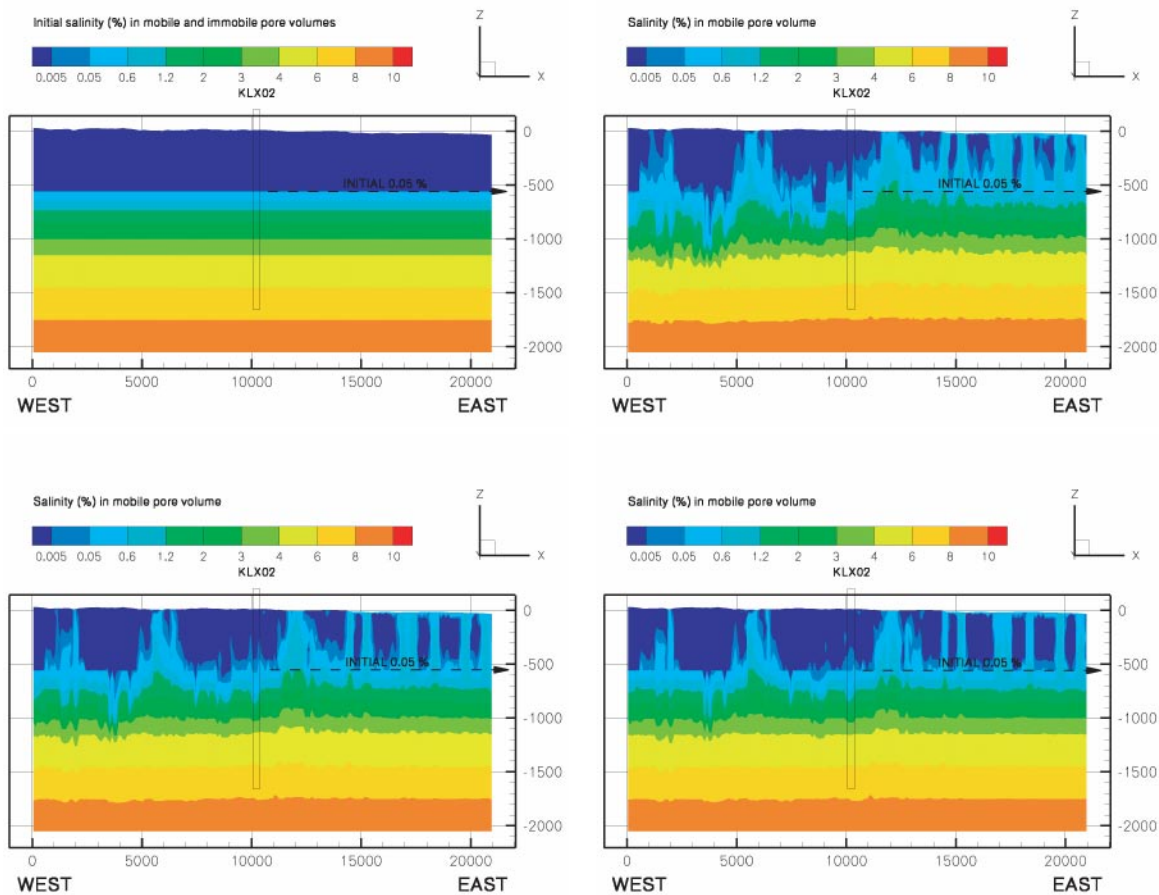
Figure 5-18. *Visualisation of the sensitivity of the salinity field to the global capacity ratio between the immobile and mobile pore volumes. The initial salinity field is shown in the upper left inset. The upper right inset shows the final mobile salinity field for Model #5; the lower left for Model #10 and the lower right for Model #11.*

In Figure 5-19 the salinity in the immobile pore volume is demonstrated by showing the salinity in three capacity boxes; a fast box, a medium fast box and a slow box. The differences are hardly visible except for the slowest capacity box, which is the box that best preserves the initial conditions.

In the work reported here we make no conclusions about the studied parameter settings of the multi-rate diffusion model. We simply conclude that the implementation of the multi-rate diffusion model for salt into DarcyTools 2.1 appears to behave as intended, but that more experience is needed for its practical use in numerical modelling of large-scale groundwater flow with variable-density flow, salt transport and different water types. Ongoing work addresses, among other things, the realism of using a multi-rate diffusion model for both salinity and water types in a coarse computational grid intersected by a sparse number of large deformation zones.
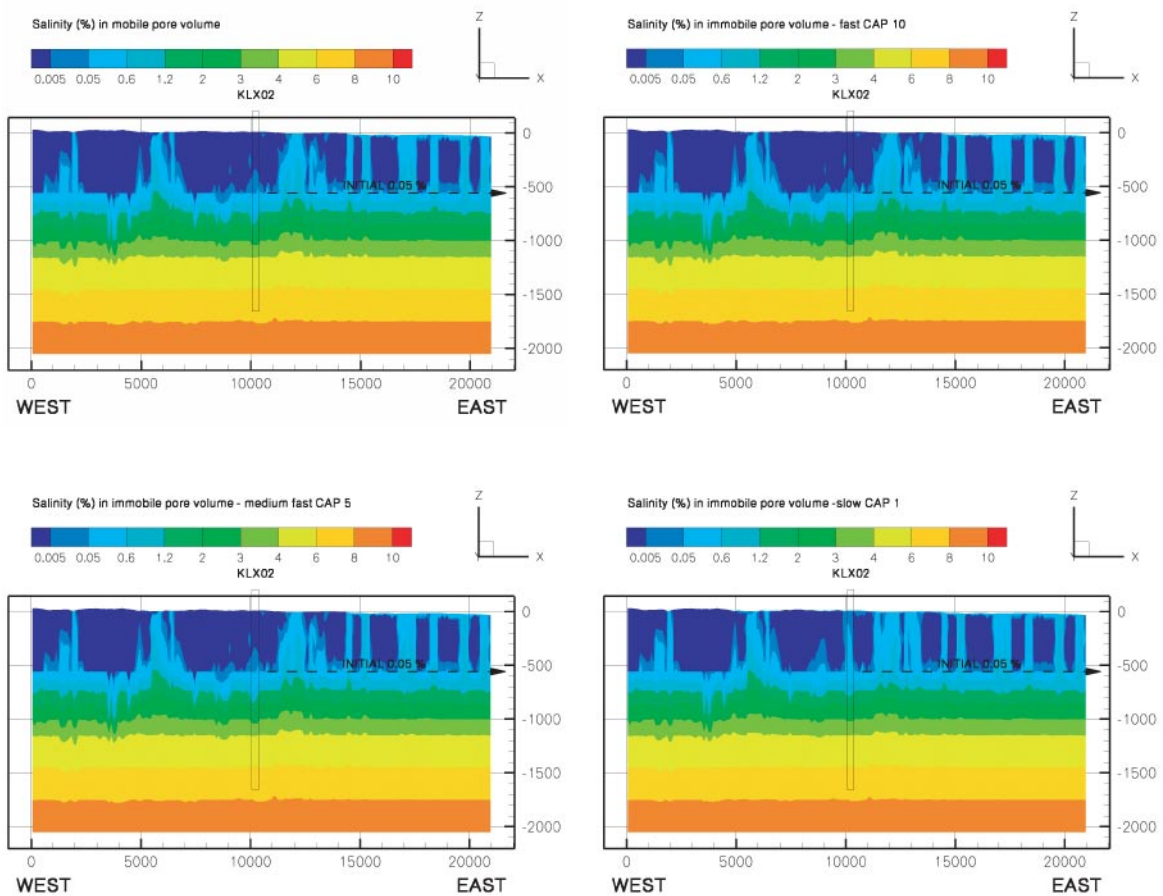
Figure 5-19. *Visualisation of the salinity in the mobile and immobile pore volumes for Model #11. Upper left: The salinity in the mobile pore volume. Upper right: The salinity in the fastest capacity box. Lower left: The salinity in a medium fast capacity box. Lower right; The salinity in the slowest capacity box.*

5.7   Sensitivity to the DFN realisation

The results shown in previous sections of this chapter all represent the outcome of a single DFN realisation but for varying parameter settings. In this section we compare the results for Model #5 (Base Case) with the outcome of a second realisation, Model #12. The realisations behind Model #5 and 12 are in this section denoted by A and B, respectively.

The number of stochastic deformation zones in realisation A is 131,338 and 130,570 in B, see Figure 5-20 and Figure 5-21. Table 5-2 shows the geometric means of the grid cell hydraulic conductivities within the local model domain at three different elevations. The values show that realisation A is slightly more conductive than realisation B owing to the difference in the number of larger deformation zones bearing in mind that transmissivity was assumed to be positively correlated to size.

Figure 5-22 shows the simulated and measured conductivity profiles versus depth at the locations of the cored boreholes KLX01 and KLX02. The simulated values represent the geometric means of the directional components on each level. The measured values were obtained by integrating measurement results on a smaller test scale, see /Follin et al. 2000/. It is noted that KLX02 runs quite close to one of the deterministically modelled deformation zones and KLX01 is intersected by a deterministically modelled deformation zone between 900–1,100 metres below ground surface.
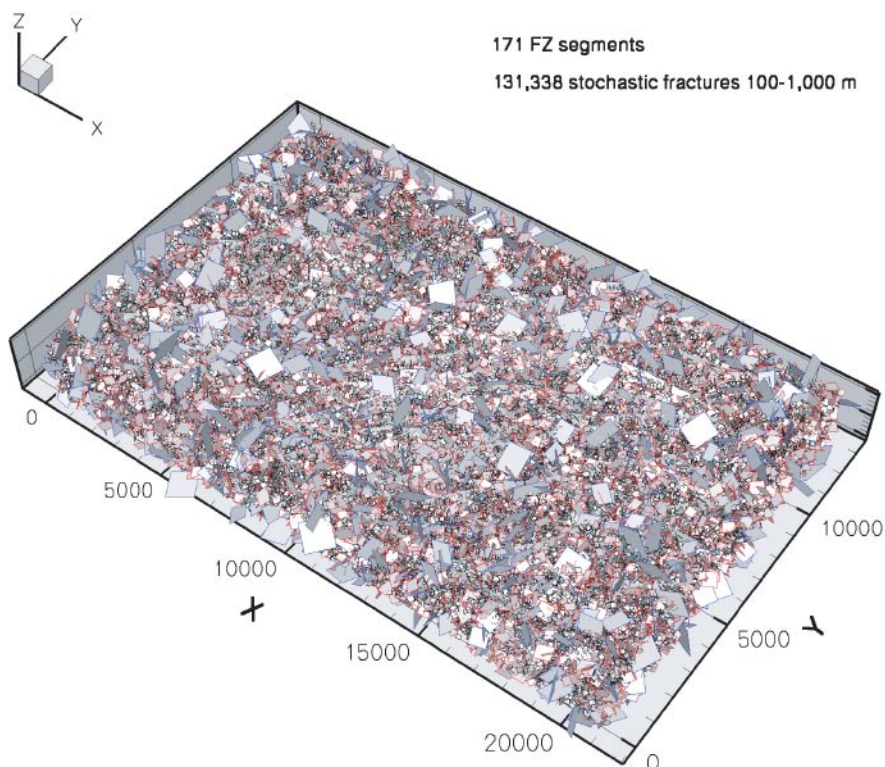
Figure 5-20. *Realisation A (Model #5). The figure is rotated 180° in order to ease the comparison with Figure 5-21.*

171 FZ segments

130,570 stochastic fractures 100-1,000 m
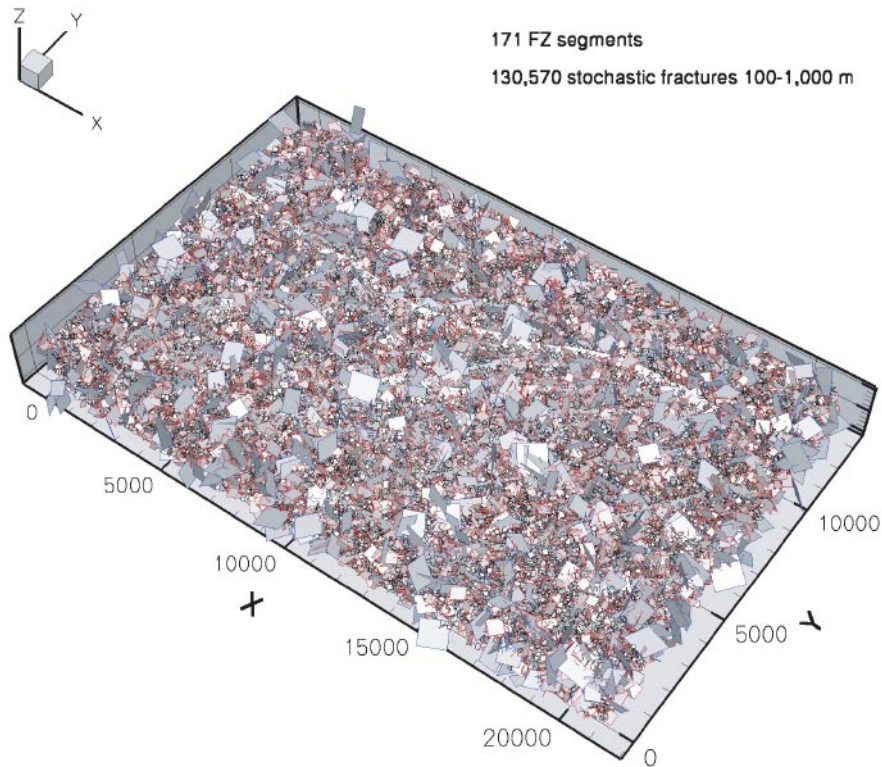
Figure 5-21. *Realisation B (Model #12).*

Table 5-2. Comparison between realisations A and B. The table shows the geometric means of the grid cell conductivities within the local model domain. Values for three elevations (–1,000) masl, (–500) masl and c (–13) masl are shown.

z = (-1,000) masl			
$K \times 10^{-9}$ (m/s)	Kxx	Kyy	Kzz
Real. A	1.48	1.45	1.44
Real. B	1.32	1.25	1.24
A/B	1.13	1.16	1.16

z = (-500) masl			
$K \times 10^{-9}$ (m/s)	Kxx	Kyy	Kzz
Real. A	1.26	1.32	1.31
Real. B	1.03	1.1	1.13
A/B	1.23	1.20	1.16

z = (-13) masl			
$K \times 10^{-9}$ (m/s)	Kxx	Kyy	Kzz
Real. A	2.44	2.17	3.62
Real. B	2.52	2.23	3.73
A/B	0.97	0.97	0.97

Number of fractures			
Size (m)	(100-200)	(200-500)	(500-1,000)
Real. A (131,338)	2,494	25,527	103,317
Real. B (130,570)	2,437	23,906	104,227
A/B	1.02	1.07	0.99

69
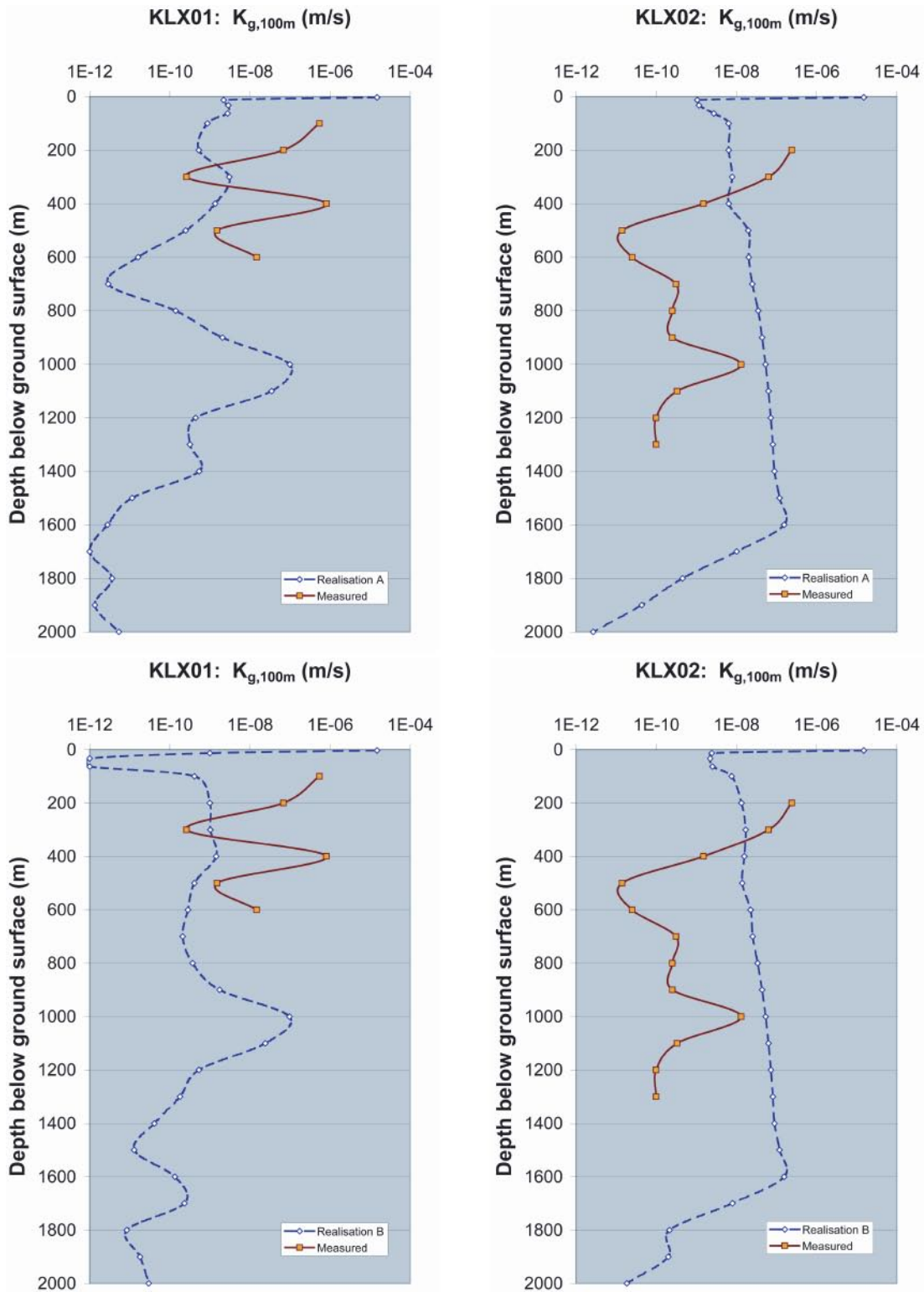
Figure 5-22. *Grid cell conductivity profiles at the locations of the cored boreholes KLX01 and KLX02. Upper row: Realisation A. Lower row: Realisation B.*

Figure 5-23 and Figure 5-24 show the differences between realisation A and B; Figure 5-23 shows the salinity profiles and Figure 5-24 shows the water type profiles. The simulation results show that:

• Realisation B renders worse matches with the chosen calibration criteria at borehole KLX01 than realisation A. In contrast, the two realisations render similar results at borehole KLX02 owing to its close vicinity to a deterministically modelled deformation zone.

The observation indicates that multiple realisations of the stochastic DFN are required. In addition, profile measurements in boreholes drilled at some distance from the deterministically modelled deformation are probably preferred.
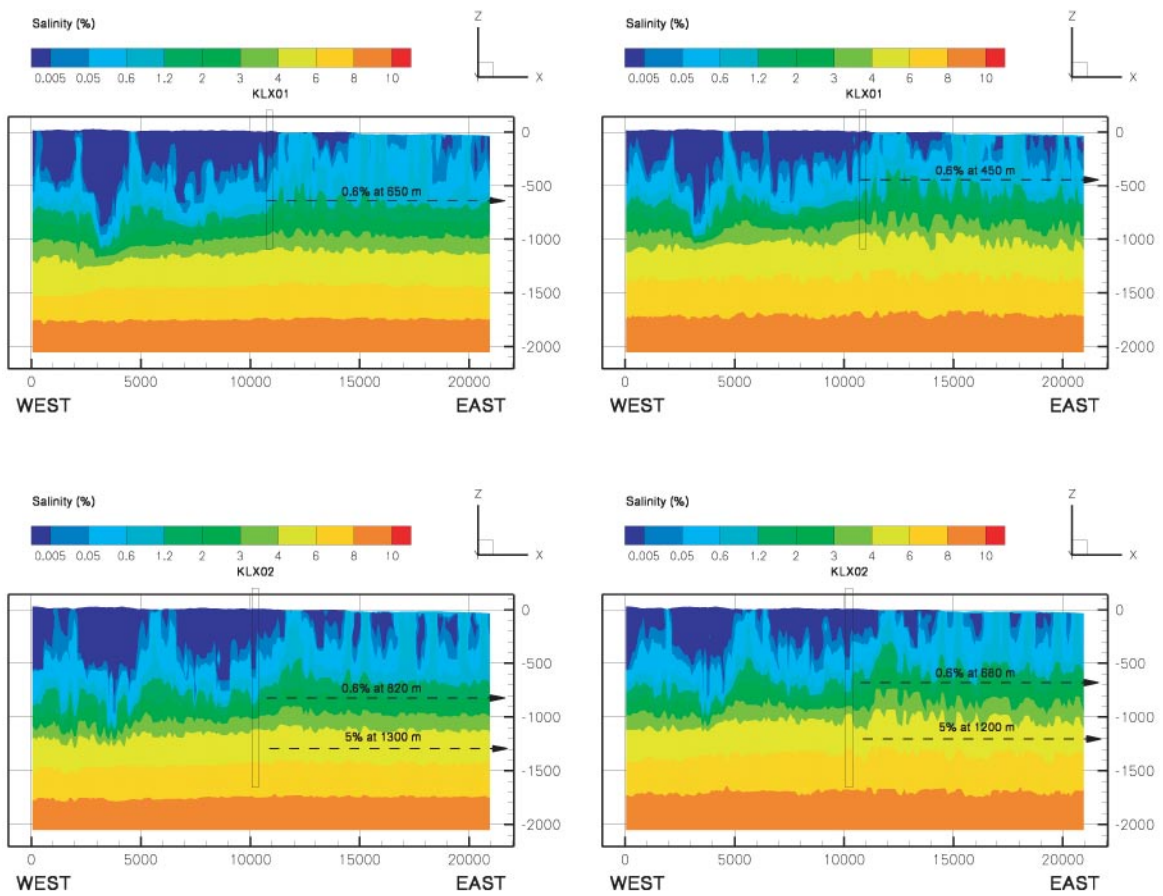
Figure 5-23. *Visualisation of the salinity field for realisations A (left column) and B (right column).*
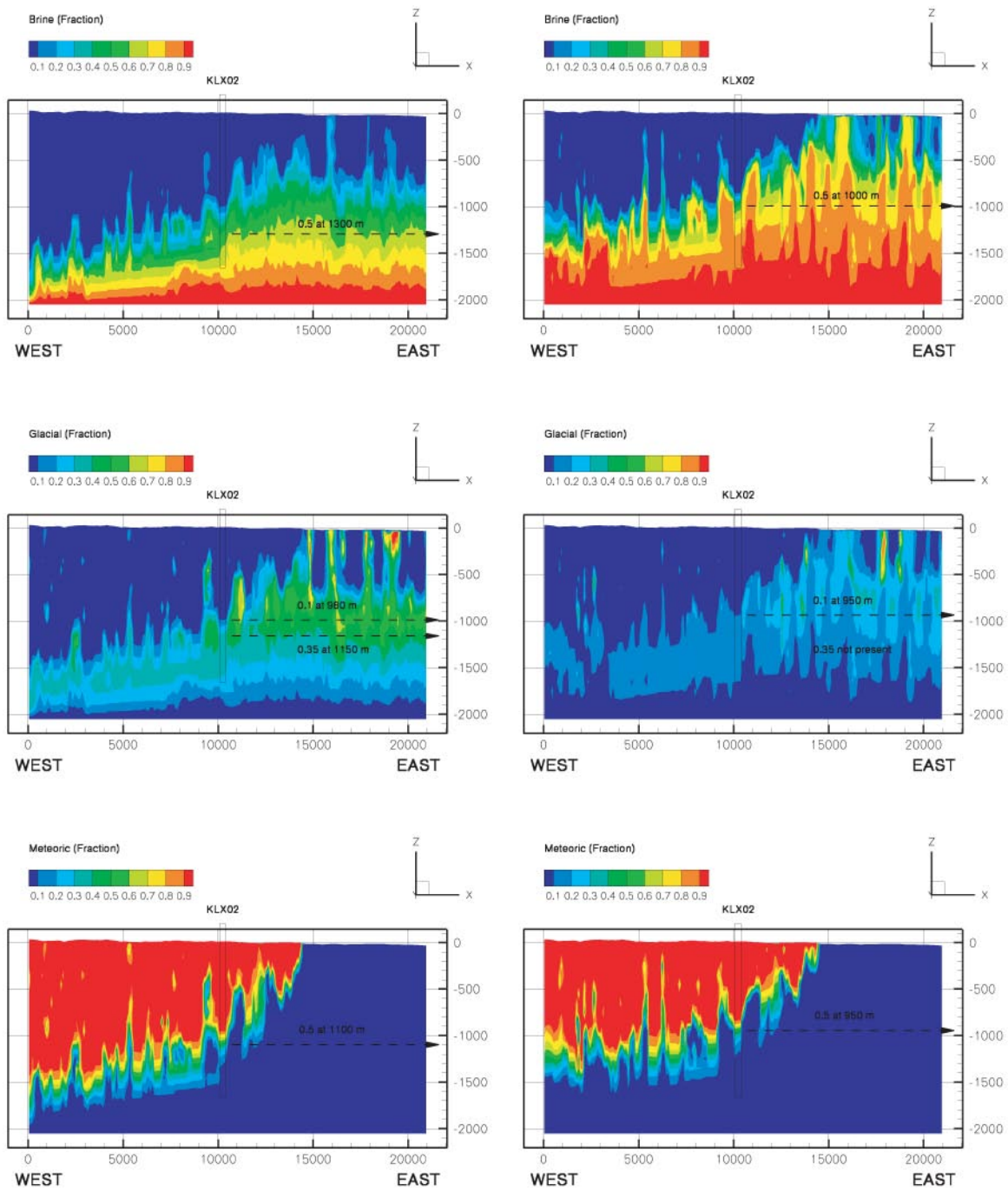
Figure 5-24. *Comparison of water type distributions between realisations A (left column) and B (right column). The flushing is deeper for realisation A.*

5.8   Sensitivity to the magnitude of T = T(L) of the DFN

The previous section addressed the sensitivity to a different realisation, i.e. a different DFN geometry. In this section we decrease the specified correlation between size and transmissivity for Model #5 by an order of magnitude while keeping all other parameter values unchanged including the transmissivity of the deterministically modelled deformation zones. The decreased correlation corresponds to Model #13 in Table 3-4. In what follows, Model #5 and 12 are denoted by realisations A and C, respectively.

The geometric means of the grid cell hydraulic conductivities within the local model domain are shown in Table 5-3. Realisation A is more conductive than realisation C, but the difference is less than an order of magnitude owing mainly to the deterministic fracture zones, the transmissivities of which were unchanged.

Figure 5-25 shows the simulated and measured conductivity profiles versus depth at the locations of the cored boreholes KLX01 and KLX02. The simulated values represent the geometric means of the directional components on each level. The measured values were obtained by integrating measurement results on a smaller test scale, see /Follin et al. 2000/. It is noted that KLX02 runs quite close to one of the deterministically modelled deformation zones and that KLX01 is intersected by a deterministically modelled deformation zone between 900–1,100 metres below ground surface.

Table 5-3. Comparison between realisations A and C. The table shows the geometric means of the grid cell conductivities within the local model domain at three elevations (–1,000) masl, (–500) masl and c (–13) masl.

$K \times 10^{-9}$ (m/s)	z = (-1,000) masl		
	Kxx	Kyy	Kzz
Real. A	1.48	1.45	1.44
Real. C	0.47	0.46	0.45
A/C	3.14	3.20	3.21

$K \times 10^{-9}$ (m/s)	z = (-500) masl		
	Kxx	Kyy	Kzz
Real. A	1.26	1.32	1.31
Real. C	0.45	0.47	0.45
A/C	2.78	2.83	2.88

$K \times 10^{-9}$ (m/s)	z = (-13) masl		
	Kxx	Kyy	Kzz
Real. A	2.44	2.17	3.62
Real. C	1.05	0.93	1.40
A/C	2.33	2.33	2.59

| Size (m)	Number of fractures		
	(100-200)	(200-500)	(500-1,000)
Real. A (131,338)	2,494	25,527	103,317
Real. C (131,338)	2,494	25,527	103,317
A/C	1.00	1.00	1.00

73
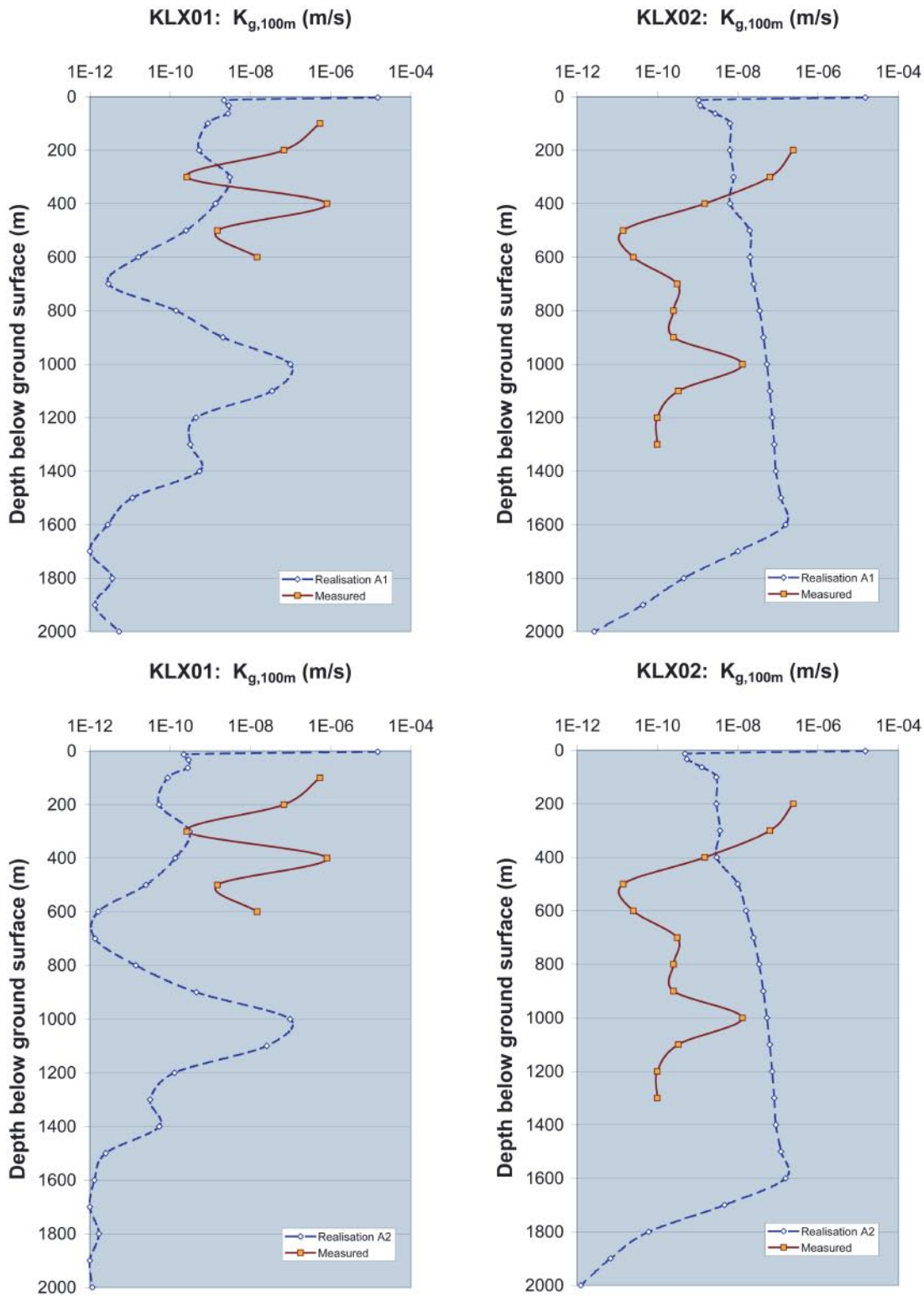
Figure 5-25. *Grid cell conductivity profiles at the locations of the cored boreholes KLX01 and KLX02. Upper row: Realisation A. Lower row: Realisation C.*

Figure 5-26 and Figure 5-27 show the differences between realisation A and C; Figure 5-26 shows the salinity profiles and Figure 5-27 shows the water type profiles. The simulation results show that realisation A and C are fairly alike concerning the salinity distribution but not concerning the distribution of different water types.

The observation suggests that salinity alone may not be a sufficiently sensitive calibration target and that model calculations of different water types may be useful as guidance in the calibration process.
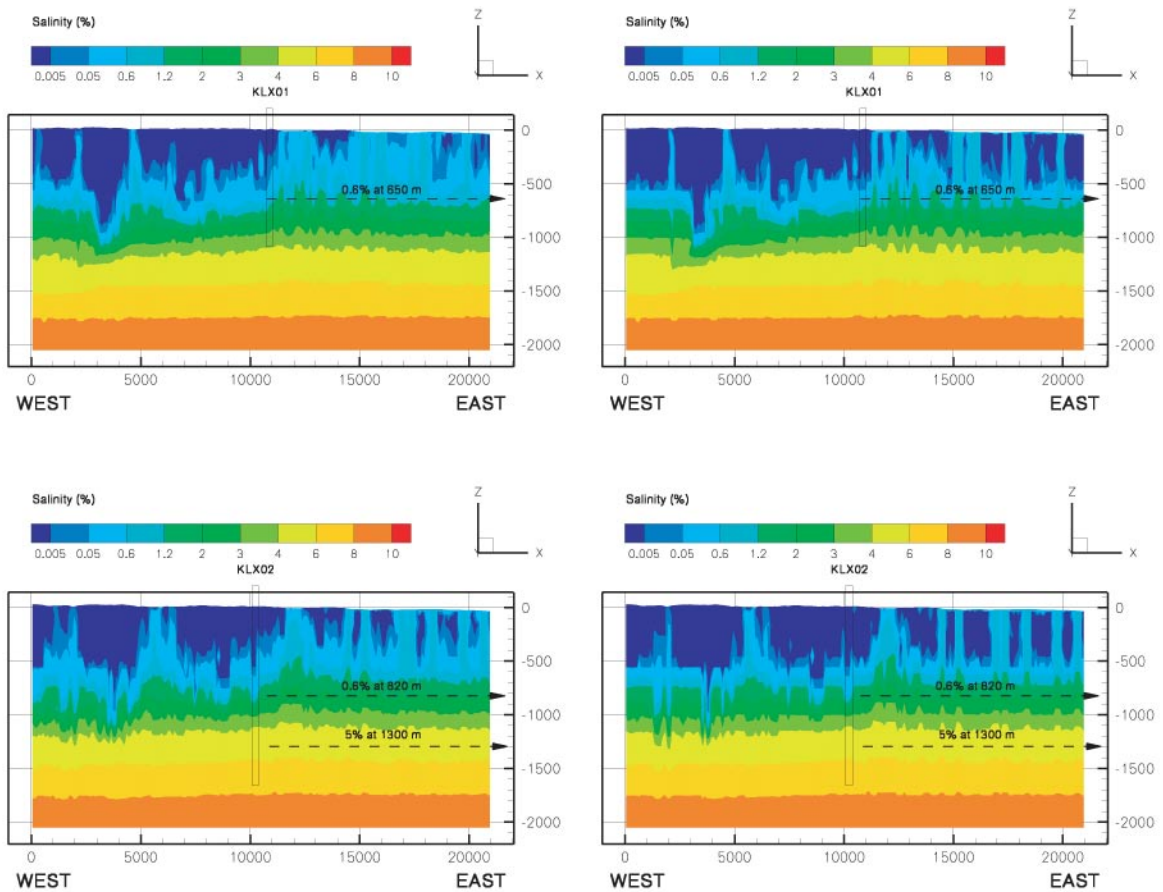
Figure 5-26. *Visualisation of the salinity field for realisation A (left column) and C (right column).*
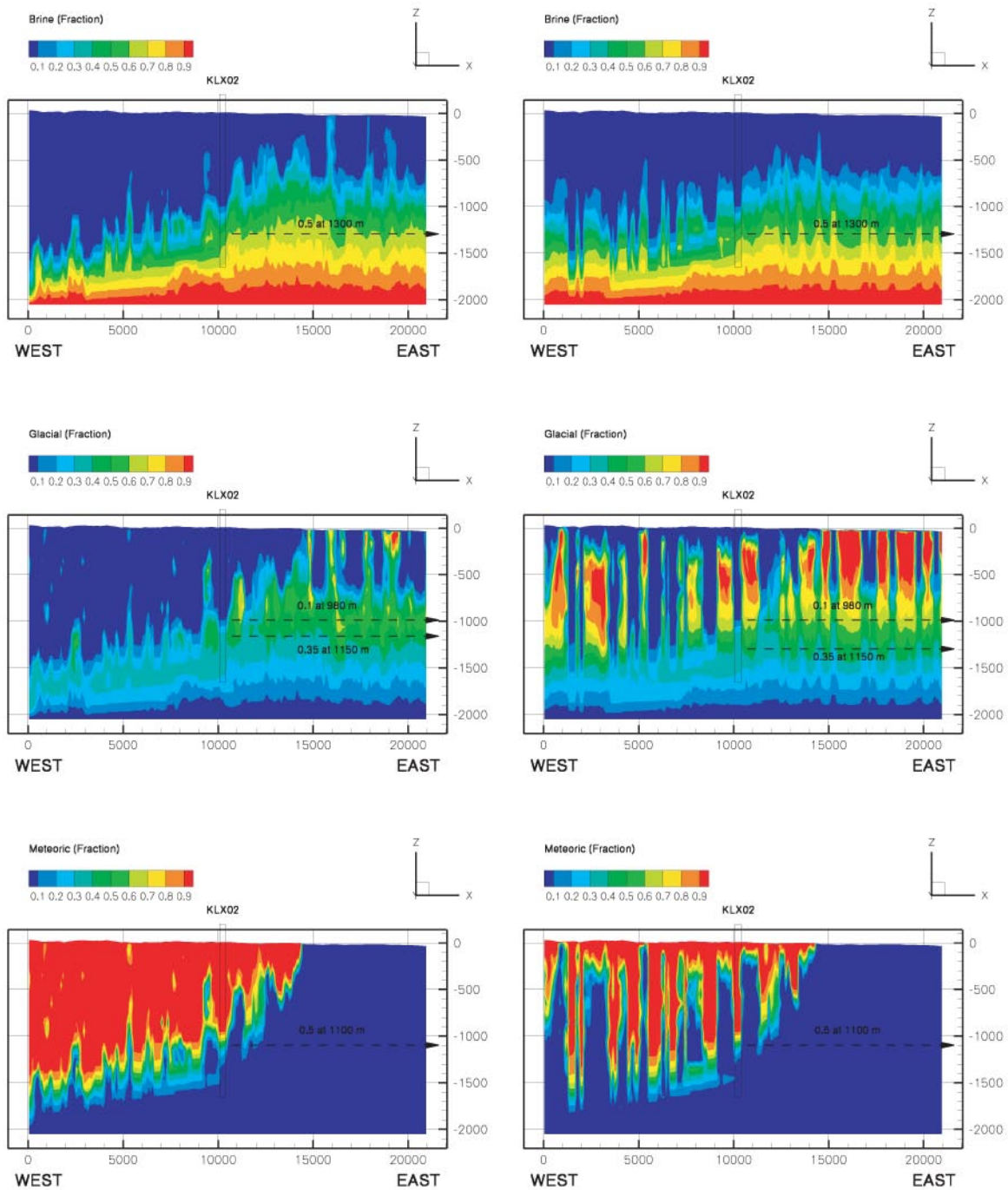
Figure 5-27. *Comparison of water type distributions between realisation A (left column) and C (right column). The flushing is deeper for realisation A.*

5.9 Sensitivity to the transmissivity of the deterministically modelled deformation zones

Section 5.7 addressed the sensitivity to a different magnitude of the correlation $T = T(L)$ for the stochastic DFN. The variation was denoted by realisation C corresponding to Model #13 in Table 3-4. In this section we decreased also the transmissivity of the deterministically modelled deformation zones by an order of magnitude. The variation is denoted by realisation D corresponding to Model #14 in Table 3-4. The geometric means of the grid cell hydraulic conductivities within the local model domain for realisations C and D are shown in Table 5-4. Realisation C is more conductive than realisation D. Realisation A is circa eight times more conductive than realisation D. The reason why the contrast is less than ten is that c 3.5% of the cells were not intersected by any deformation zones.

Figure 5-28 shows the simulated and measured conductivity profiles versus depth at the locations of the cored boreholes KLX01 and KLX02. The simulated values represent the geometric means of the directional components on each level. The measured values were obtained by integrating measurement results on a smaller test scale, see /Follin et al. 2000/.

Table 5-4. Comparison between realisations C and D. The table shows the geometric means of the grid cell conductivities within the local model domain at three elevations (–1,000) masl, (–500) masl and c (–13) masl.

$K \times 10^{-9}$ (m/s)	$z = (-1,000)$ masl		
	Kxx	Kyy	Kzz
Real. C	0.47	0.46	0.45
Real. D	0.19	0.18	0.18
C/D	2.52	2.46	2.44

$K \times 10^{-9}$ (m/s)	$z = (-500)$ masl		
	Kxx	Kyy	Kzz
Real. C	0.45	0.47	0.45
Real. D	0.17	0.18	0.18
C/D	2.63	2.64	2.60

$K \times 10^{-9}$ (m/s)	$z = (-13)$ masl		
	Kxx	Kyy	Kzz
Real. C	1.05	0.93	1.40
Real. D	0.43	0.39	0.56
C/D	2.46	2.40	2.51

Size (m)	Number of fractures		
	(100-200)	(200-500)	(500-1,000)
Real. C (131,338)	2,494	25,527	103,317
Real. D (131,338)	2,494	25,527	103,317
C/D	1.00	1.00	1.00
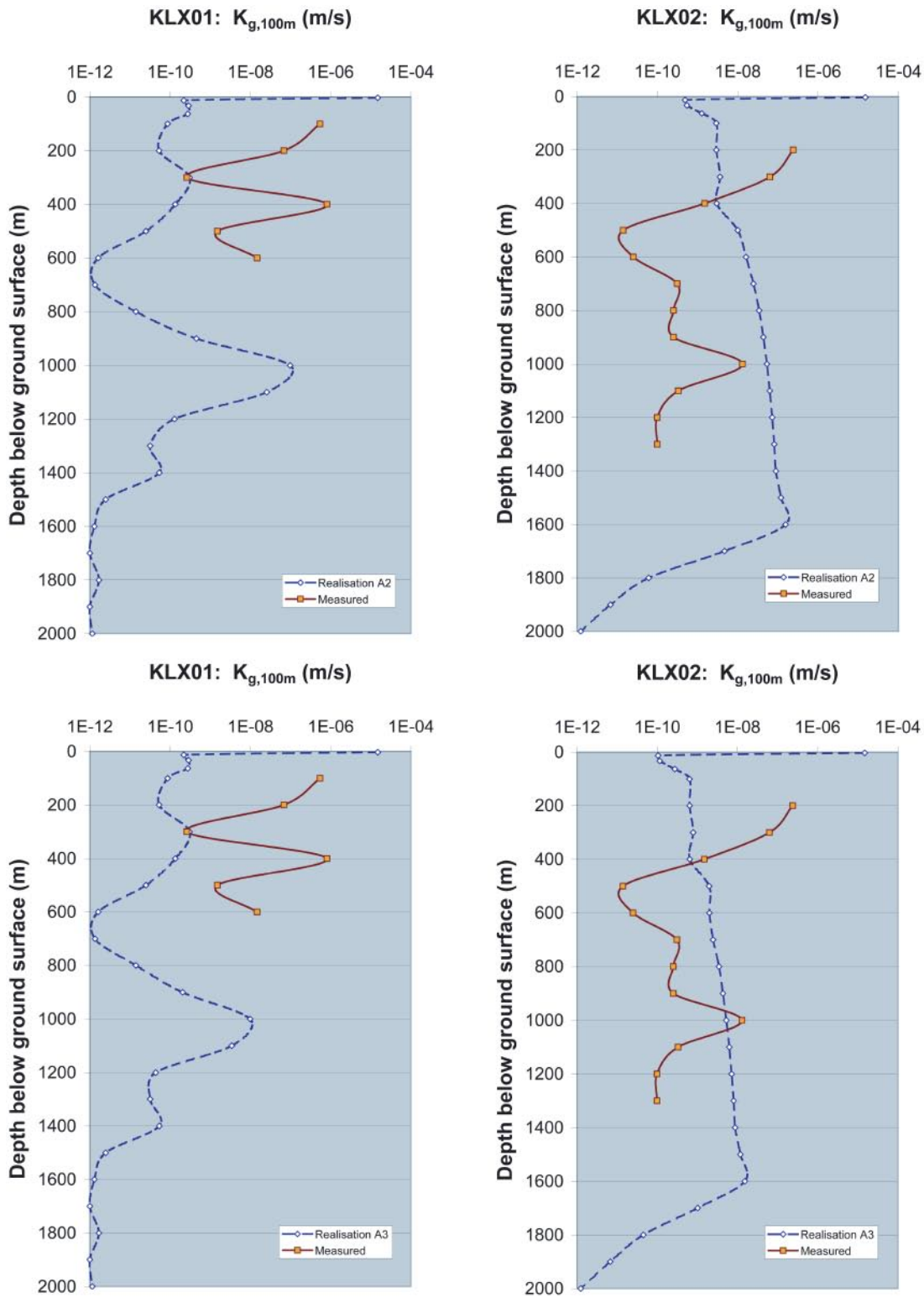
Figure 5-28. *Grid cell conductivity profiles at the locations of the cored boreholes KLX01 and KLX02. Upper row: Realisation C. Lower row: Realisation D.*

Figure 5-29 and Figure 5-30 show the differences between realisation C and D; Figure 5-29 shows the salinity profiles and Figure 5-30 shows the water type profiles. The simulation results show that:

• Realisation D reinforces the differences shown in Figure 5-26 and Figure 5-27. In particular, it is noted that the contrast in salinity between the stochastic DFN and the deterministically modelled is sharpened in realisation D.

• The outcropping of the deterministically modelled deformation zones appears to be as an important parameter as their transmissivity value.
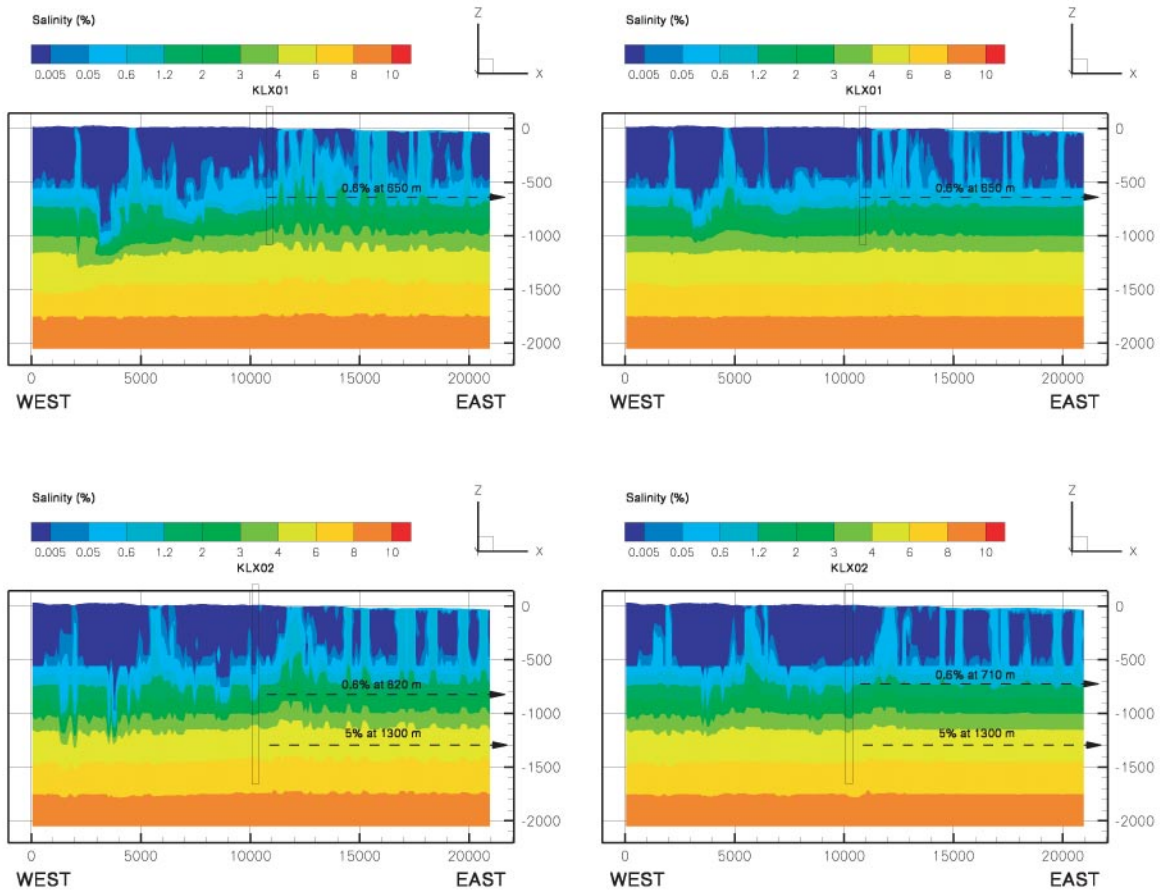
Figure 5-29. *Visualisation of the salinity field for realisation C (left column) and D (right column).*
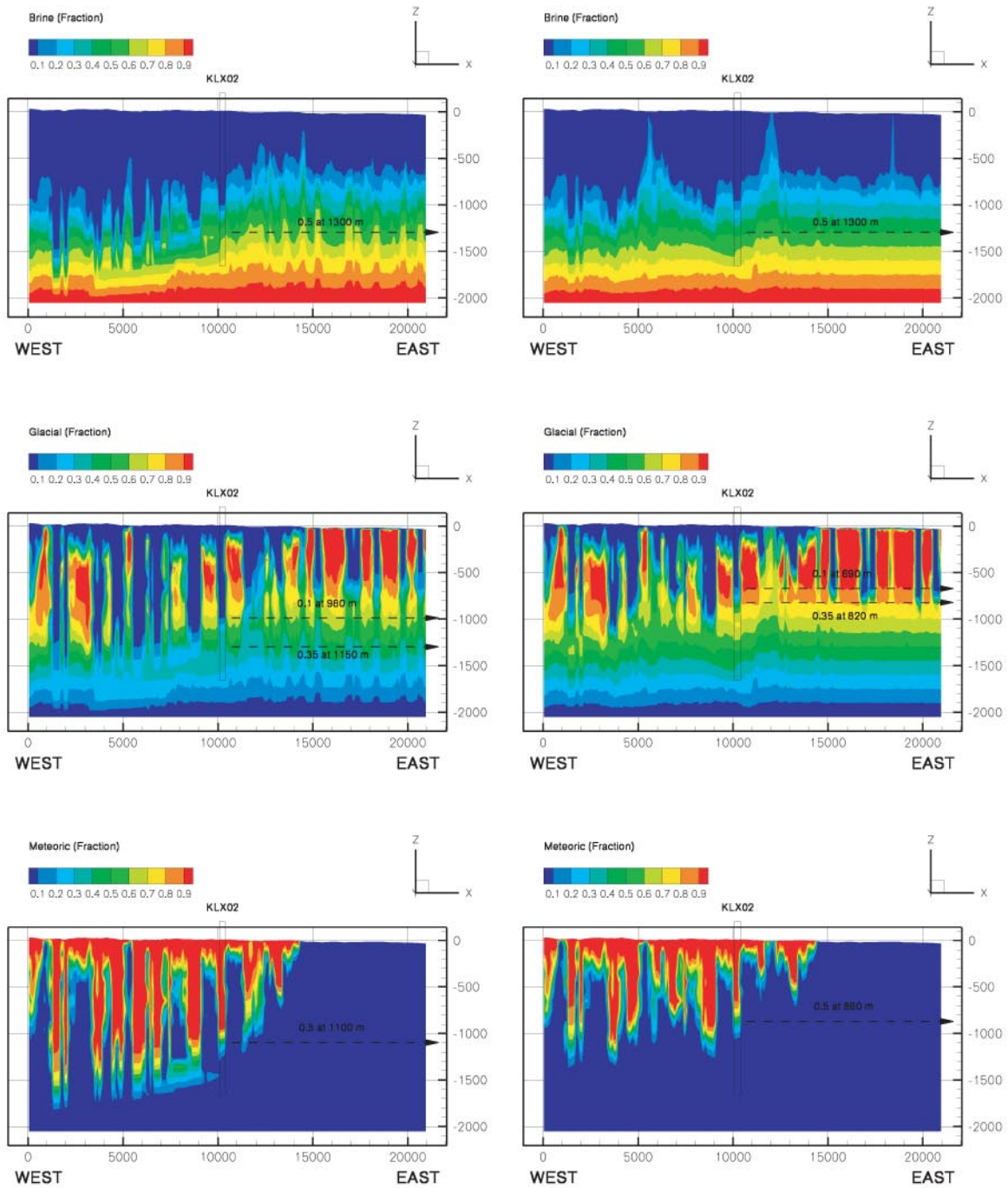
***Figure 5-30.*** *Comparison of water type distributions between realisation C (left column) and D (right column). The flushing of C and D are both less than for realisation A1.*

6   Flow related transport parameters

6.1   General

This chapter focuses on particle tracking and flow related transport parameters. The flow porosity used for the advective particle tracking was the same as the flow porosity used for transient advective-diffusive salinity transport calculations. The particle flow paths were computed by means of interpolation using the steady-state velocity field calculated for the present flow conditions. The maximum step length was set to 10% of the grid cell size, i.e. 10 m. The particles were released at (–500) masl within two rectangular release areas, referred to as the Laxemar and Simpevarp subareas in the previous chapters. The locations of the release areas are shown in Figure 6-1, on a topographic map where also the identified lineaments in the area are indicated.

The particles were released on a regular grid, i.e. without flux weighting. The spacing between the starting positions within the release areas was 50 m; 800 particles were released in the Simpevarp release area and 832 in the Laxemar release area. Hence, four particles were released in each grid cell, such that the lateral distance from any starting position to the nearest adjacent grid cell in the horizontal was 25 m.
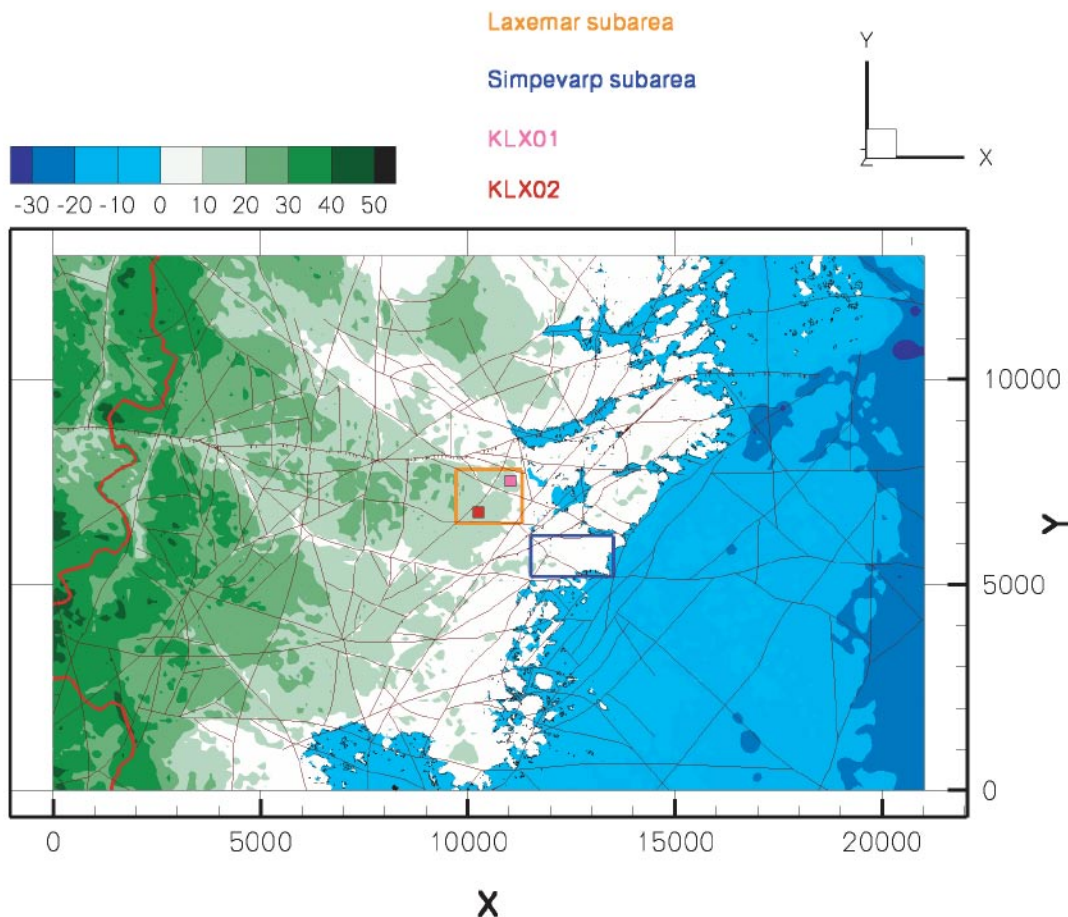
Figure 6-1. *Topographic map with deformation zone lineaments and the regional surface water divide (red line). Particles were released within the indicated Laxemar (orange) and Simpevarp (blue) release areas.*

It was demonstrated in Section 3.3 that all grid cells were intersected by at least one stochastic deformation zone in all directions in the case of the higher DFN intensity investigated. In contrast, c 3.5% of the grid cells at repository depth within the local model area were not intersected by stochastic deformation zones in any direction in the case of the lower DFN intensity. The lower DFN intensity was used in all particle tracking simulations discussed in this chapter, which implies that some of the potential starting positions were located in cells without intersecting deformation zones.

For particles starting in grid cells without stochastic or deterministic deformation zones the approach described in Chapter 2 cannot be used; Equation (2-8) and Equation (2-11) are useless unless a value of the FWS for the "non-fractured background rock" is assumed. In this study, it was decided that all particles starting in grid cells without intersecting deterministic or stochastic zones were to be excluded from the particle tracking analysis. In the simulation results shown below, empty grid cells are used to indicate the starting positions that were excluded because they had no intersecting deformation zones.

6.2   Outputs and implications of model simplifications

The required deliverables from the particle tracking simulations are listed in Section 3.6. Essentially, the model outputs can be divided into two main categories:

- The geometric description of the flow paths: the actual paths, including the exit positions of particles at the boundaries of the model, and calculated path lengths between starting and exit positions.
- The transport parameters (performance measures): Darcy fluxes at starting positions, and flow-related transport parameters (F parameter and advective travel time, t_w).

The geometric description is primarily useful for developing the hydrogeological understanding of the modelled site. It provides mainly visual information on flow patterns, thereby illustrating, for instance, the degree of hydraulic contact between different parts of the model volume and the locations of discharge areas. The transport parameters, on the other hand, provide quantitative information on the transport conditions along the flow paths. This type of information can either be used for direct comparisons between different sites or between site-specific parameters and safety criteria, or as an input to other transport models. However, the transport parameters also provide information relevant for the site understanding, as further discussed below.

In the evaluation of the particle tracking simulations, especially the calculated transport parameters, it is important to note that the lower size (length) limit of the DFN was 100 m. In addition, particles were released in cells intersected by stochastic and/or deterministic structures only, and the rock mass between the structures was assumed not to contribute to the flow-wetted surface or the flow porosity. This means that structures smaller than 100 m were not considered explicitly in the model, such that particles were released into and transported in a fractured medium consisting of relatively large structures only.

Since smaller structures realistically can be expected to contribute significantly to the integrated F- and t_w-values of flow paths, this implies that these parameters are considerably under-estimated (orders of magnitude) in the present results. This is due to the fact that only a subset of the structures that would make up more "complete" flow paths are considered in the model, but also to the release of particles at positions that would not be included in a more realistic transport scenario (i.e. in large deterministic deformation zones).

The main implication of these model limitations is that the transport parameters should not be regarded as quantitative in the sense that they can be used in comparisons between sites or with safety criteria. Transport calculations in flow models with finer discretisation are performed by Safety Assessment. The present results can, however, be used for comparing different sensitivity cases, bearing in mind that the values only represent a part of the "actual flow paths". Such quantifications are useful for setting the information provided by the visual impressions of the flow paths and the calculated path lengths into a relevant perspective. In this context, the transport parameters should be regarded as generalised measures of the properties of the flow paths, not as Safety Assessment performance measures. In other words, they express differences that are otherwise only observed visually in terms of relevant quantities.

It should also be noted that other assumptions that affect the transport parameters have been made in the model development. In particular, the geometric surface area of the structures (flow-wetted surface), as calculated for each cell based on the DFN, was used without modification in the F calculation. Concerning the details of the F calculations, the reader is referred to the description of the definitions used in DarcyTools, see Chapter 2. It is noted that the cumulative F values shown below for the different cases are, in this study, directly proportional to the assumed fixed value of the specific flow wetted surface, cf Table 3-4. If the active flow wetted surface area per unit fracture surface area is much smaller/greater than the nominal value used in this study, the cumulative statistics are to be corrected accordingly.

The effect of excluding some starting positions on the statistics of the transport parameters was found to small though owing to: (i) the small number of non-fractured grid cells, and (ii) the short lateral distance from any starting position to the nearest adjacent grid cell (25 m). An equally important note is the fact that the starting positions of the remaining particles in this study were chosen without any consideration of whether the grid cell was intersected by a deterministic or stochastic deformation zone, or to the magnitude of the latter.

6.3   Base Case and sensitivity study

As described in Chapter 3 (Table 3-4) through Chapter 5, a large number of groundwater flow simulations have been performed. In a first set of simulations, Model #1, which met the specification in the Task Description, was tested. This resulted in Model #5, which constituted the reference case for Models #6–14. Model #5 is also the Base Case for the sensitivity study of flow paths and transport parameters discussed below.

Flow paths and transport parameters are available for most of the model variations specified in Table 3-4, thereby providing qualitative and quantitative information on the effects of the parameter variations on transport entities. In the following, we first describe the results of the Base Case, and then a number of sensitivity cases where the Base Case results are compared with other model variants. A description of the sensitivity study is given in Section 3.4. For convenience, the sensitivity cases are summarised also here; the cases described below concern variations of the following parameters, as compared to Model #5:

- **The hydraulic properties of the uppermost rock layer (Model #3):** In the sensitivity case, the hydraulic conductivity of the uppermost rock layer was constant and lower than in the Base Case, in which fractures and fracture zones of higher transmissivities were allowed to penetrate also the uppermost layer.

- **The position of the salinity interface (Model #7):** In the sensitivity case, the initial condition in the transient flow simulation that produced the present-day flow field for the particle tracking prescribed a more shallow salinity interface than the Base Case.

- **The position of the western boundary of the model domain (Model #8):** The sensitivity case had its western boundary of the flow model at the regional water divide, instead of further west at the boundary of the regional Simpevarp model domain.

- **The flow porosity of fractures and fracture zones (Model #9):** In the sensitivity case, the (uniform) flow porosity of the deterministic and stochastic structures was reduced to 20% of the value used in the Base Case.

- **The effect of using a different DFN realisation (Model #12):** The whole sequence of flow and particle tracking simulations was repeated for another DFN realisation generated with the same input parameters as the Base Case.

- **The transmissivity of the stochastic structures (Model #13):** The transmissivities of all stochastic structures were reduced by one order of magnitude.

- **The transmissivities of the deterministic and the stochastic structures (Model #14):** The transmissivities of both the deterministic and the stochastic structures were reduced by one order of magnitude.

In the subsequent sections, flow paths and statistics of transport parameters for the Base Case and the different cases considered in the sensitivity study are shown. First, the Base Case is presented in detail, showing a relatively large number of different visualisations of the results. Then, a more condensed presentation of the sensitivity cases is given. Finally, the results are summarised and discussed in Section 6.12.

6.4   Base Case results

The presentation of the transport results for the Base Case consists of a relatively large set of figures, Figure 6-2 through Figure 6-7, and a table summarising the transport parameter statistics (Table 6-1). In addition to providing a sufficiently detailed reporting of the Base Case, the presentation is also intended to demonstrate some of the tools for presentation and analysis that have been developed.

The different types of figures presented and the main observations made in these figures can be summarised as follows:

- **Figure 6-2** shows horizontal visualisations of all advective flow paths. By comparison with Figure 6-1, which illustrates the larger, deterministically modelled deformation zones, it becomes clear that these zones have a profound effect on the flow path pattern. The particles released in the smaller structures outside the deterministic zones tend to travel to the larger zones, where they are transported further to the exit points at the upper model boundary. Therefore, the flow path pattern is quite similar to the pattern of deterministic zones in Figure 6-1.

- **Figure 6-3** illustrates flow paths in an E-W vertical section. It can be seen that most particles reach the ground surface within or very close to the release areas. Essentially, only a few particles from the Laxemar release area are transported much further outside the release area than a distance on the order of the E-W extent of this area. It is also observed that the particles from the Simpevarp release, which is closer to the coastline, have a stronger tendency to discharge locally.

- **Figure 6-4** shows 3D visualisations of the flow paths, confirming the observations that most particles discharge locally and that the few relatively longer flow paths that can be observed originate from the Laxemar release area.

- **Figure 6-5** presents flow path lengths and Darcy fluxes at starting positions for each particle, with the results for each flow path reported at its starting position. Thus, the colour of a cell indicates the parameter value associated with the flow path starting at that cell. Whereas the Darcy fluxes are strongly related to the deterministic zones (large values/orange or red coloured cells in these zones), this correspondence is not as obvious for the path lengths. Especially for the Laxemar release area it can be seen that there is a tendency towards relatively longer flow paths for particles released in the western part of the area; see also Figure 6-3, which shows that most of the longer flow paths come from the "upstream part" of the release area. This illustrates that both the hydraulic conditions at the starting position and the general flow pattern are important for the paths length. Once a particle has reached one of the larger zones, which it may do after a relatively short travel distance, it either discharges locally or travels some distance in the zone, as determined by the flow direction there.

- **Figure 6-6** provides a similar presentation of travel times, t_w, and F parameters associated with the individual particles (note the $\log_{10}$ representations). It can be noted that the spatial distributions of these two parameters are similar, although F displays a larger spatial variability (more red/orange and dark blue cells). The deterministic zones are readily identified in the results for both parameters, indicating that particles released within or in the vicinity of these zones follow flow paths characterised by short travel times and small F-values. The correlation between the hydraulic conditions at the starting positions and these transport parameters appear to be stronger for the Laxemar release area than for the Simpevarp area. Furthermore, t_w and F show stronger correlations to the starting positions (whether within or outside deterministic zones) than the path lengths (cf Figure 6-5). This indicates that the contributions from the deterministic zones to the integrated t_w- and F-values are usually small, such that the parameter values are dominated by the smaller structures for particles starting there.

- **Figure 6-7** presents some illustrations of the calculated t_w- and F-distributions, i.e. a few results from basic data evaluations. It can be seen that the ($\log_{10}$-) parameters have relatively uniform distributions over most of their variation intervals, deviating from simple, unimodal Gaussian distributions. Conversely, the F distribution for the Laxemar release area (upper right diagram) indicates a bimodal behaviour, possibly resulting from starting positions within and outside the deterministic zones. However, whereas the distributions clearly show differences between the different parameters and release areas, it should also be noted that the variation intervals for each parameter (the intervals containing the bulk of the data) are more or less the same for the two release areas. The t_w-F plots (bottom row) give clear evidence of correlations between the two parameters, i.e. a large value of t_w for a particle usually corresponds to a large value of F for that particle. The correlations appear to be linear in the log-log space. However, no attempt has been made to quantify these correlations.

Table 6-1 summarises some output statistics from the particle tracking simulations, i.e. the 5th, 50th and 95th percentiles of the Darcy fluxes at starting positions, q, and the F- and t_w-values for the flow paths. In addition, a normalised measure of variability has been calculated as $(F_{95\%}–F_{5\%}) / F_{50\%}$ for F, and similarly for the other parameters.

It can be seen in Table 6-1 that the Laxemar release area generally displays smaller travel times and F-values and larger Darcy fluxes than the Simpevarp area. Variability is also smaller in the results for the particles released in the Laxemar area, with the exception of

the variability in the F parameter. Generally, the differences between the two release areas can be regarded as relatively small (not order(s) of magnitude); for example, the relative difference in the median values of t_w and F is about 50% when normalised with the Laxemar values. Furthermore, the differences between the release areas in terms of the "point" parameter q are larger than those observed for the integrated parameters F and t_w.
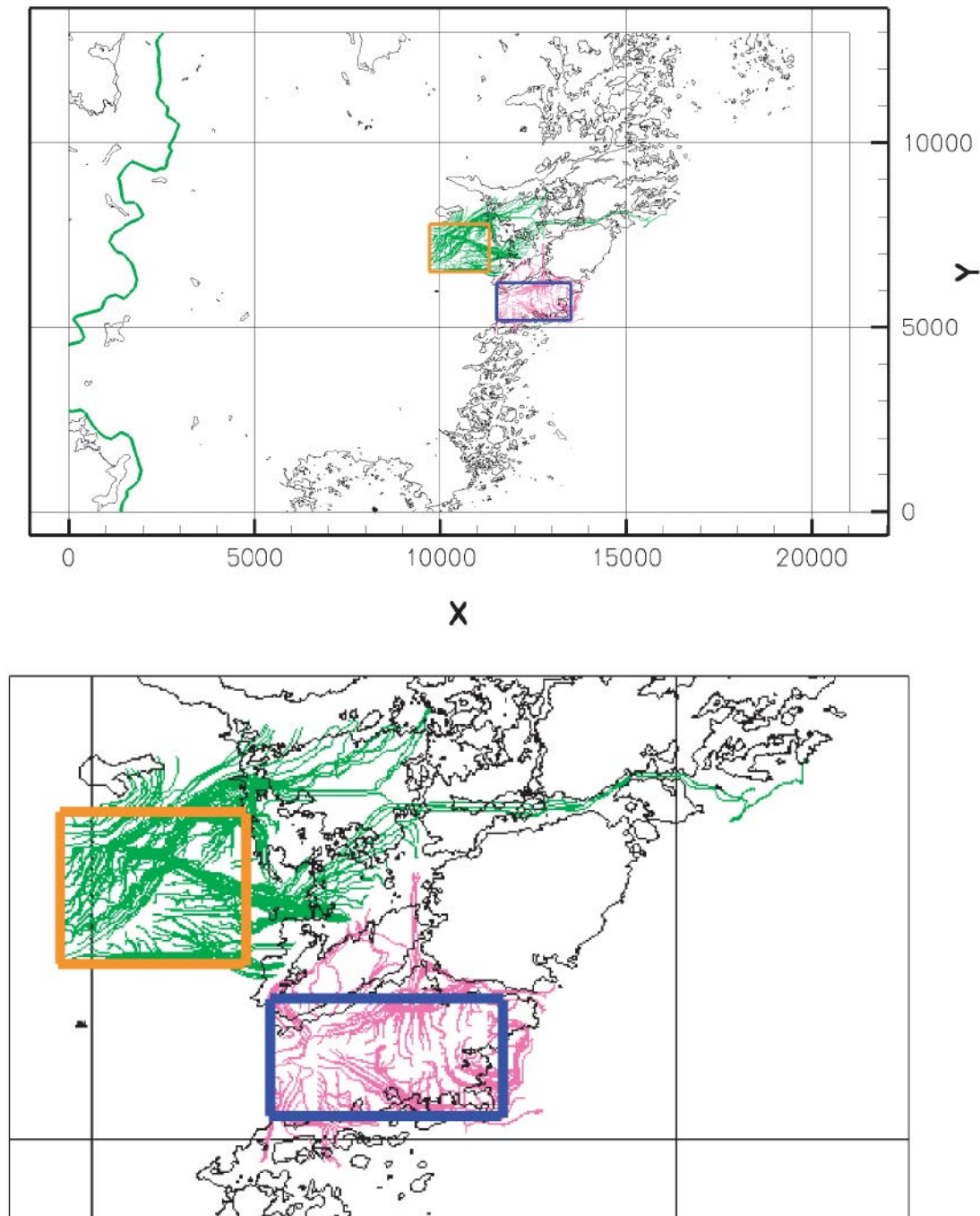
Figure 6-2. *Visualisations of advective flow paths for Model #5 in the horizontal plane, overview (top) and detail (bottom). The Laxemar release area is indicated by the orange rectangle and the Simpevarp release area by the blue one.*
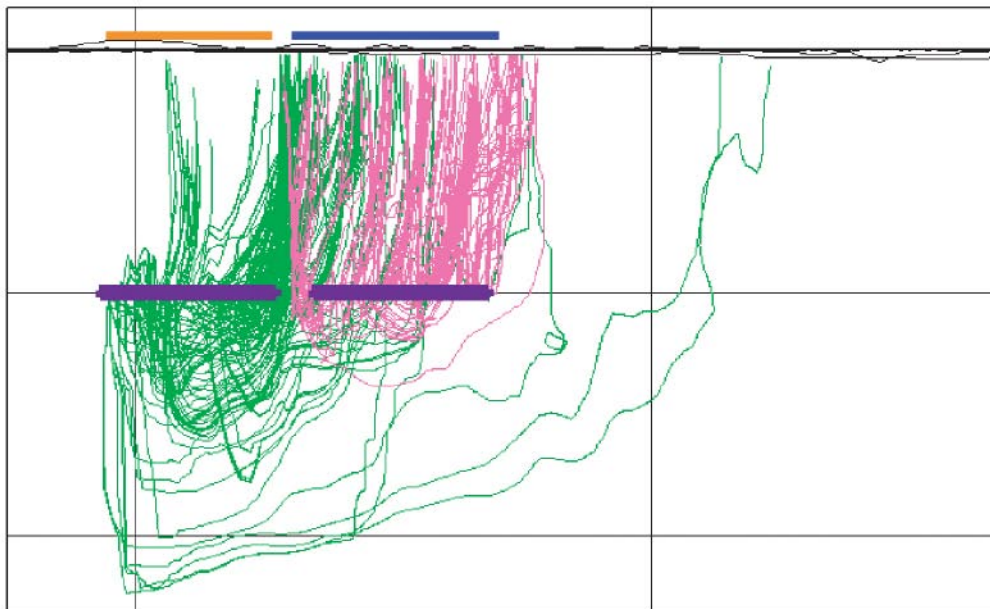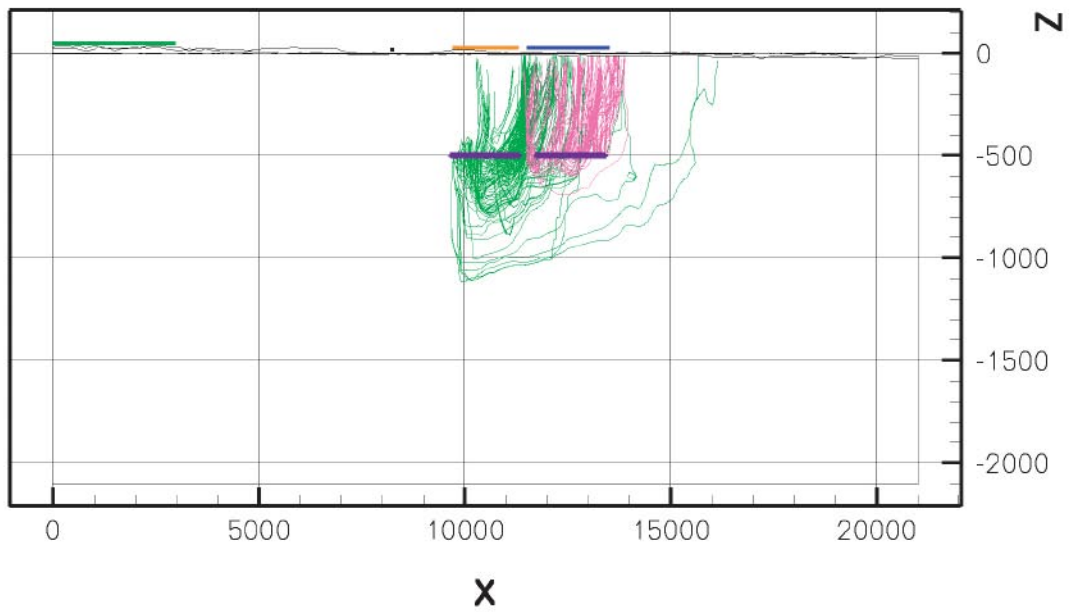
Figure 6-3. *Advective flow paths for Model #5 visualised in an E-W vertical section, overview (top) and detail (bottom). The E-W extent of the Laxemar and Simpevarp release areas are indicated at release depth and at ground level.*

87
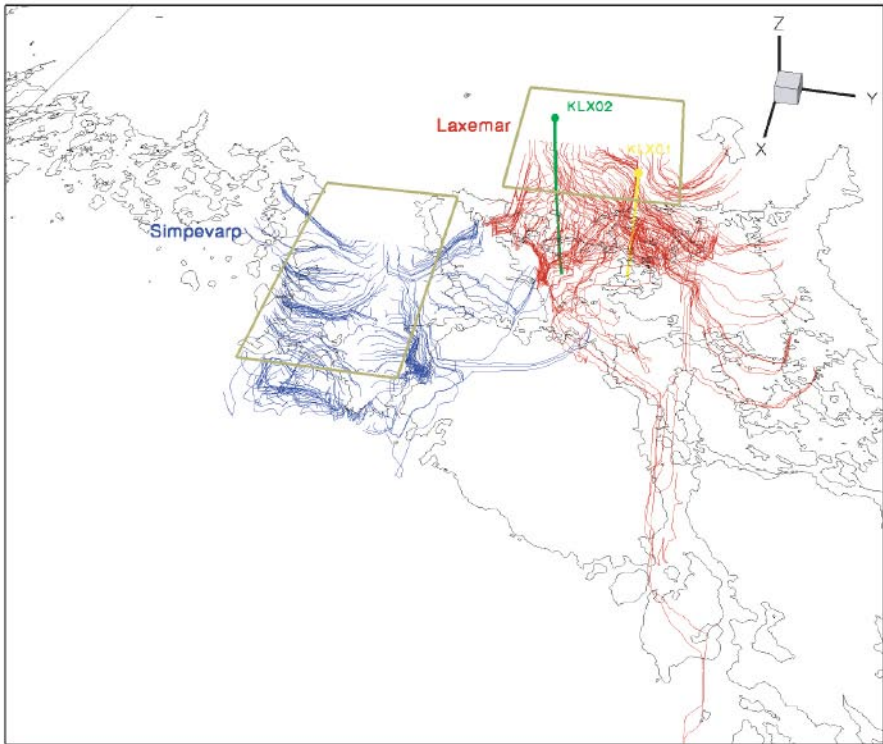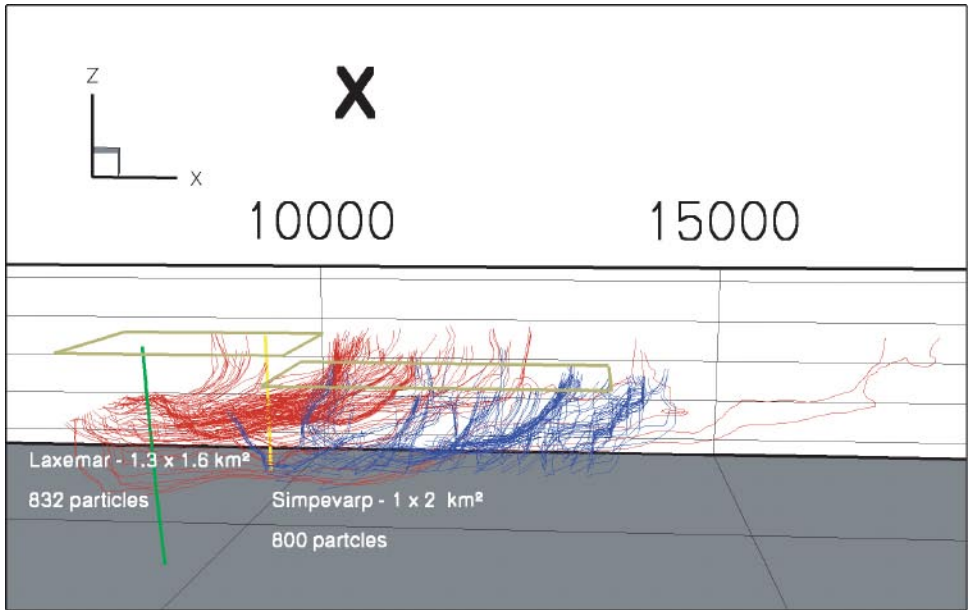
Figure 6-4. 3D visualisations of advective flow paths for Model #5 (note the orientation of the bottom figure).
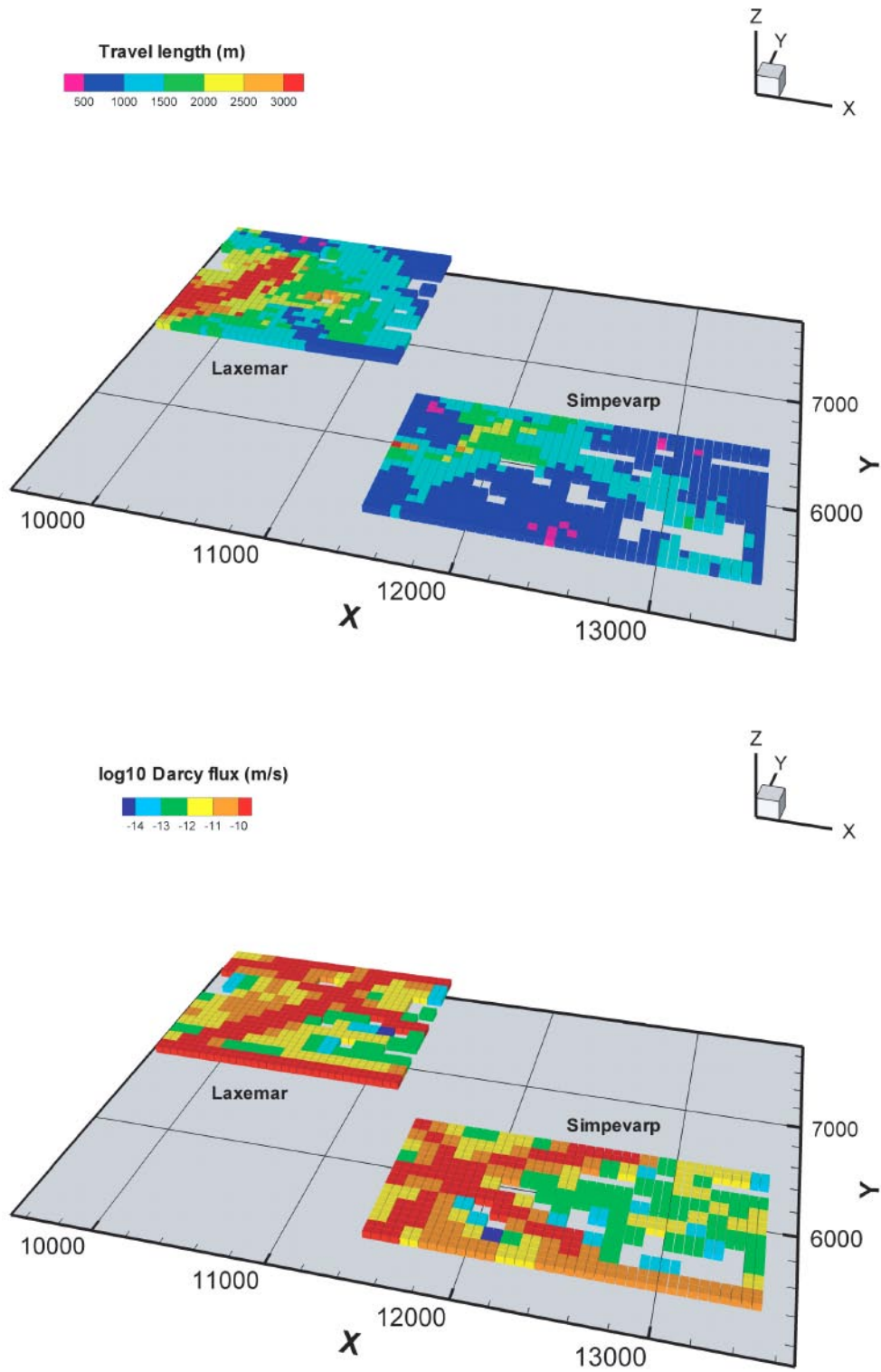
Figure 6-5. *Calculated travel lengths (top) and Darcy fluxes at starting positions (bottom) for particles in Model #5; the result for each particle is reported at its starting position. Empty cells indicate positions where no particles were released.*
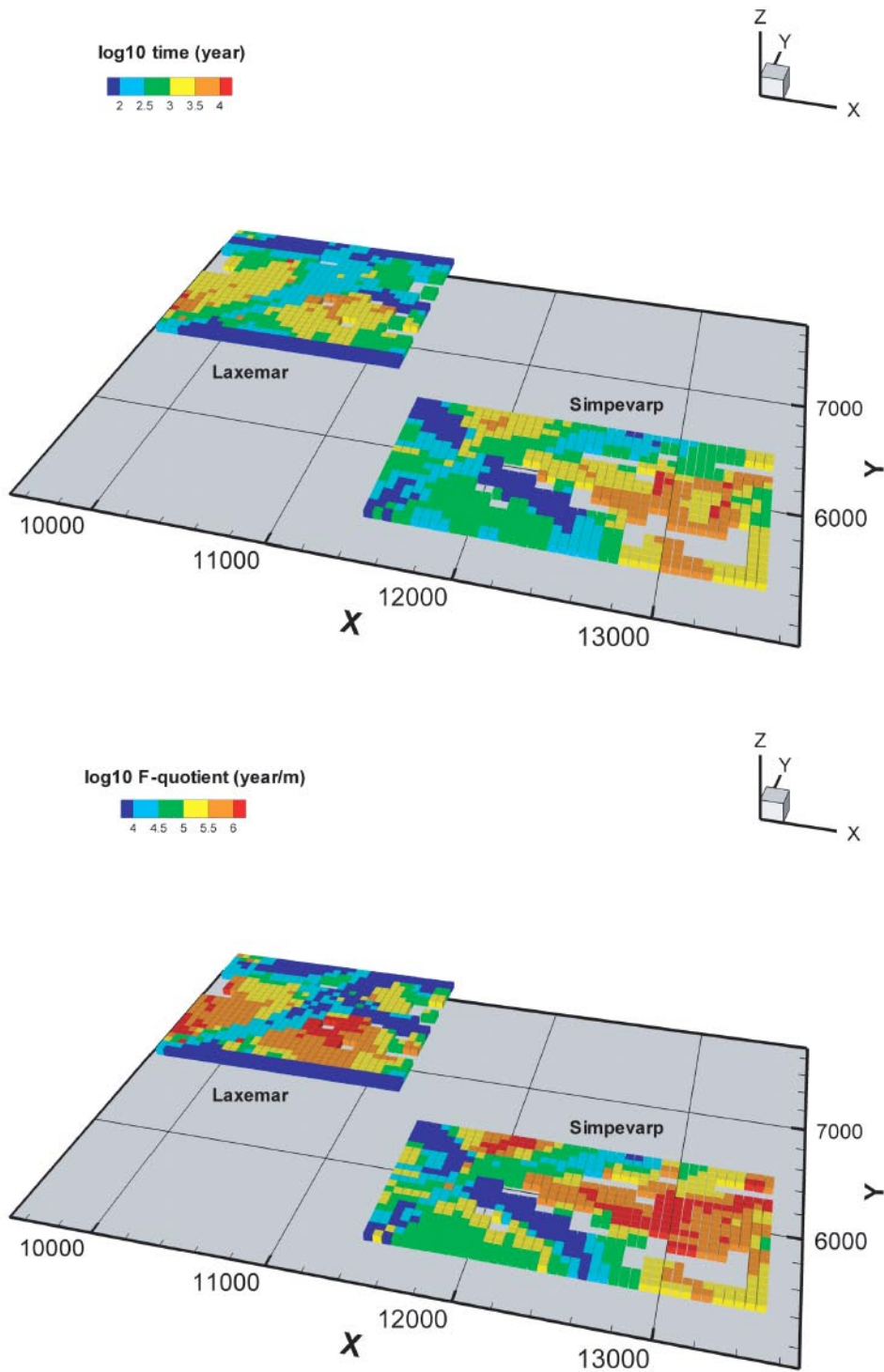
Figure 6-6. *Calculated travel times (top) and F values (bottom) for particles in Model #5; the result for each particle is reported at its starting position. Empty cells indicate positions where no particles were released.*
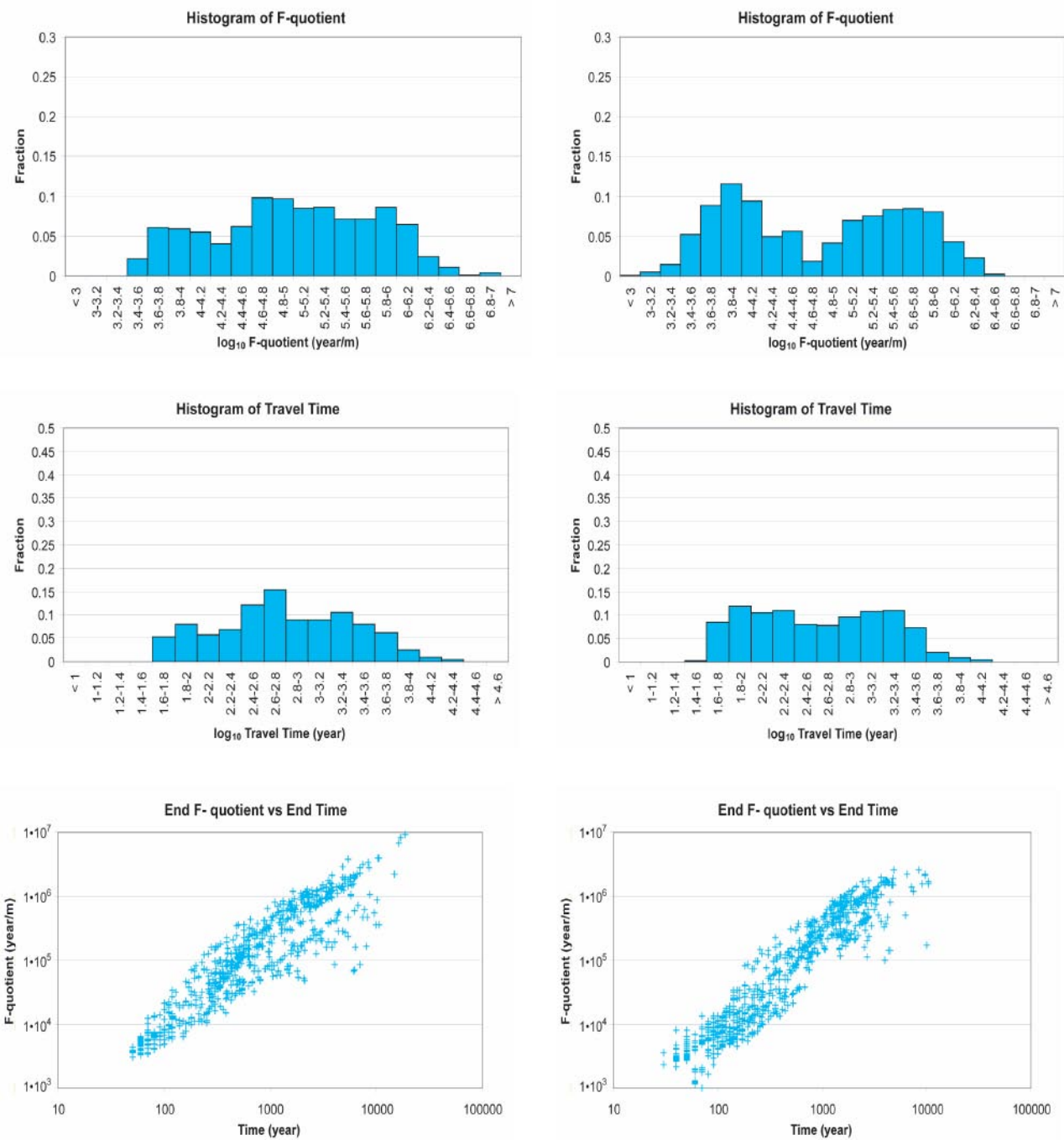
Figure 6-7. *Histograms of calculated F- and t_w-distributions and diagrams showing corresponding F- and t_w-values for each particle (Model #5); the results for the Simpevarp release area are in the left column and those for the Laxemar release area in the right.*

Table 6-1. Summary of particle tracking results for Model #5 (Base Case).

F (y/m)	Laxemar	Simpevarp
$F_{5\%}$	$3.3 \cdot 10^3$	$4.9 \cdot 10^3$
$F_{50\%}$	$6.4 \cdot 10^4$	$1.0 \cdot 10^5$
$F_{95\%}$	$1.2 \cdot 10^6$	$1.4 \cdot 10^6$
$(F_{95\%} - F_{5\%}) / F_{50\%}$	18.7	14.0
t_w (y)	Laxemar	Simpevarp
$t_{w,5\%}$	50	60
$t_{w,50\%}$	390	560
$t_{w,95\%}$	3,340	5,740
$(t_{w,95\%} - t_{w,5\%}) / t_{w,50\%}$	8.4	10.1
q (m/s)	Laxemar	Simpevarp
$q_{5\%}$	$1.2 \cdot 10^{-13}$	$3.9 \cdot 10^{-14}$
$q_{50\%}$	$1.3 \cdot 10^{-11}$	$3.4 \cdot 10^{-12}$
$q_{95\%}$	$8.2 \cdot 10^{-10}$	$2.5 \cdot 10^{-10}$
$(q_{95\%} - q_{5\%}) / q_{50\%}$	63.1	73.5

6.5　Sensitivity to the treatment of the uppermost rock layer

Sections 6.5–6.11 present the results of the sensitivity study outlined in Section 6.3. The various sensitivity cases are described in less detail than the Base Case (cf above), focusing on comparisons with the Base Case in a few key figures and a data table for each sensitivity case. Some comments, highlighting what is viewed as the main results of the comparisons, are provided for each sensitivity case. However, the emphasis of the presentation is on figures and tables.

In the sensitivity case addressing the properties of the uppermost rock layer (Model #3), the hydraulic conductivity of the uppermost layer was constant and lower than in the Base Case (Model #5), in which the structures were allowed to penetrate the uppermost layer resulting in higher grid cell conductivities along the structures. Thus, the uppermost layer acts as a more efficient "barrier" in the sensitivity case, which can be expected to result in longer flow paths and larger travel times.

As shown in Figure 6-8, the flow path lengths indeed increase. In the sensitivity case, a larger fraction of the released particles are transported to exit points outside the immediate vicinity of the release areas; this causes the deterministic structures to be clearly visible also at some distance from these areas. It is also observed that the properties of the uppermost rock layer affect the particles' "selection" of zones such that a larger fraction of the flow paths have an eastern direction. Whereas the Simpevarp release area has some long flow paths that are not present in the Base Case, it can be noted that the maximum path length does not increase for the Laxemar release.
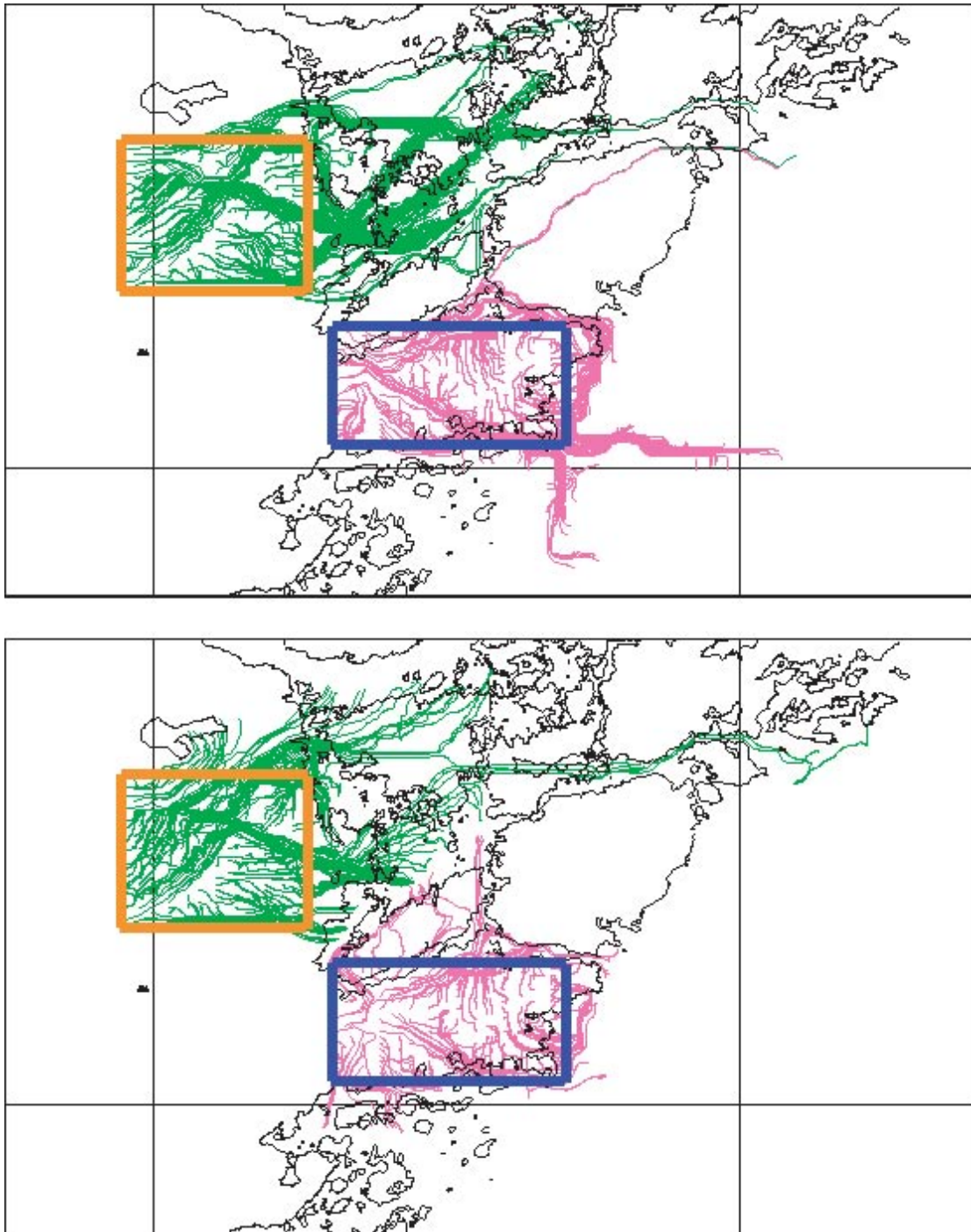
Figure 6-8. *Comparison of advective flow paths for Model #3 (sensitivity case; top) and Model #5 (Base Case; bottom).*

The comparison between the sensitivity case and the Base Case in Figure 6-9 shows that the path lengths increase for most starting positions when the hydraulic conductivity of the uppermost rock layer is reduced. Especially for the Laxemar release area, it can also be noted that the dependence on whether the release point is within or outside the deterministic zones is weaker for the sensitivity case.
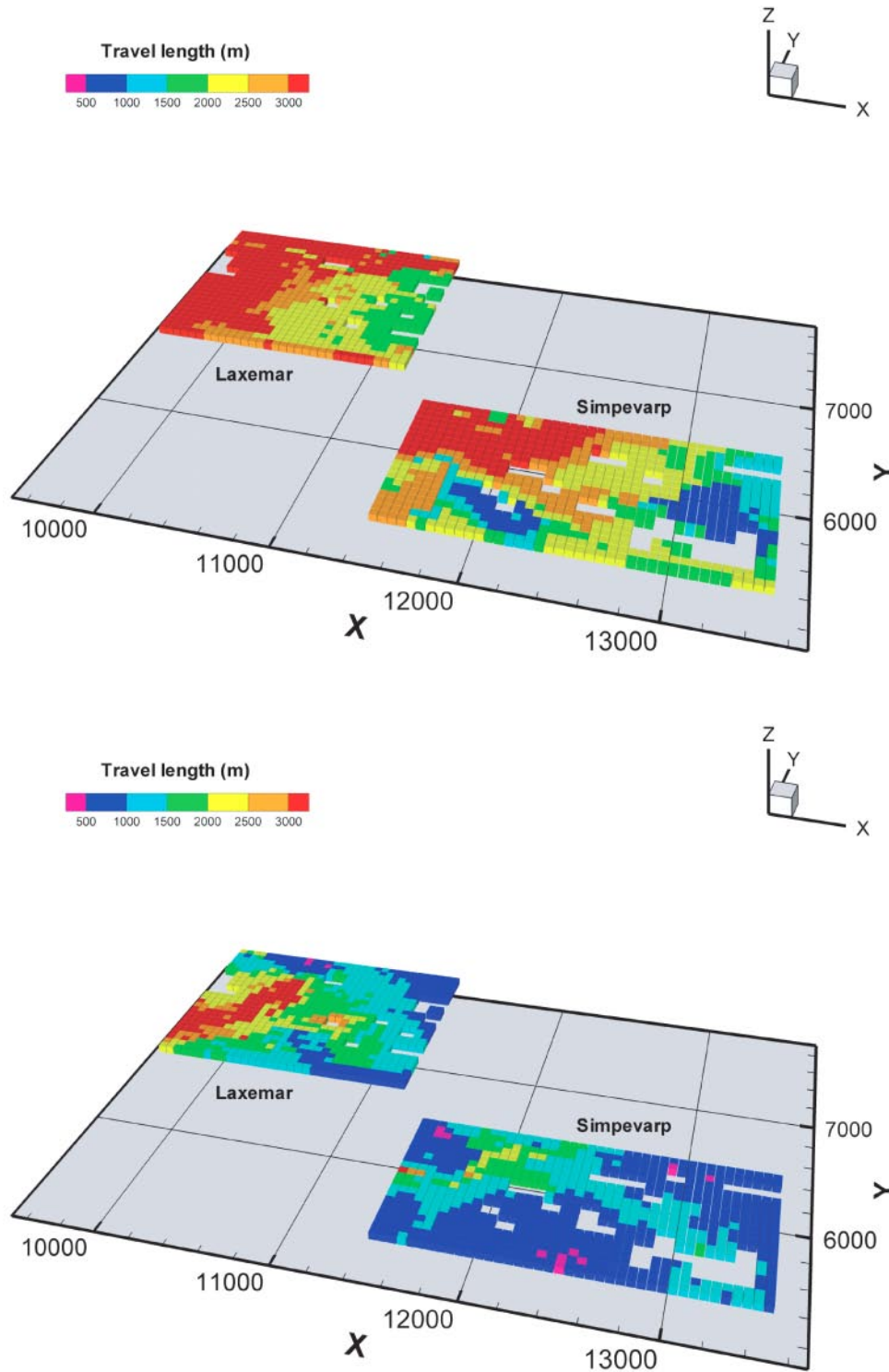
Figure 6-9. *Comparison of calculated flow path lengths, reported at each starting position, for Model #3 (sensitivity case; top) and Model #5 (Base Case; bottom). Empty cells indicate positions where no particles were released.*

The comparison of travel times in Figure 6-10 shows a general increase for the sensitivity case. In particular, blue cells, that would have indicated the shortest travel times, are absent from the upper figure. This also implies that the introduction of a homogeneous upper layer reduces the spatial variability in travel times, and hence the significance of the starting
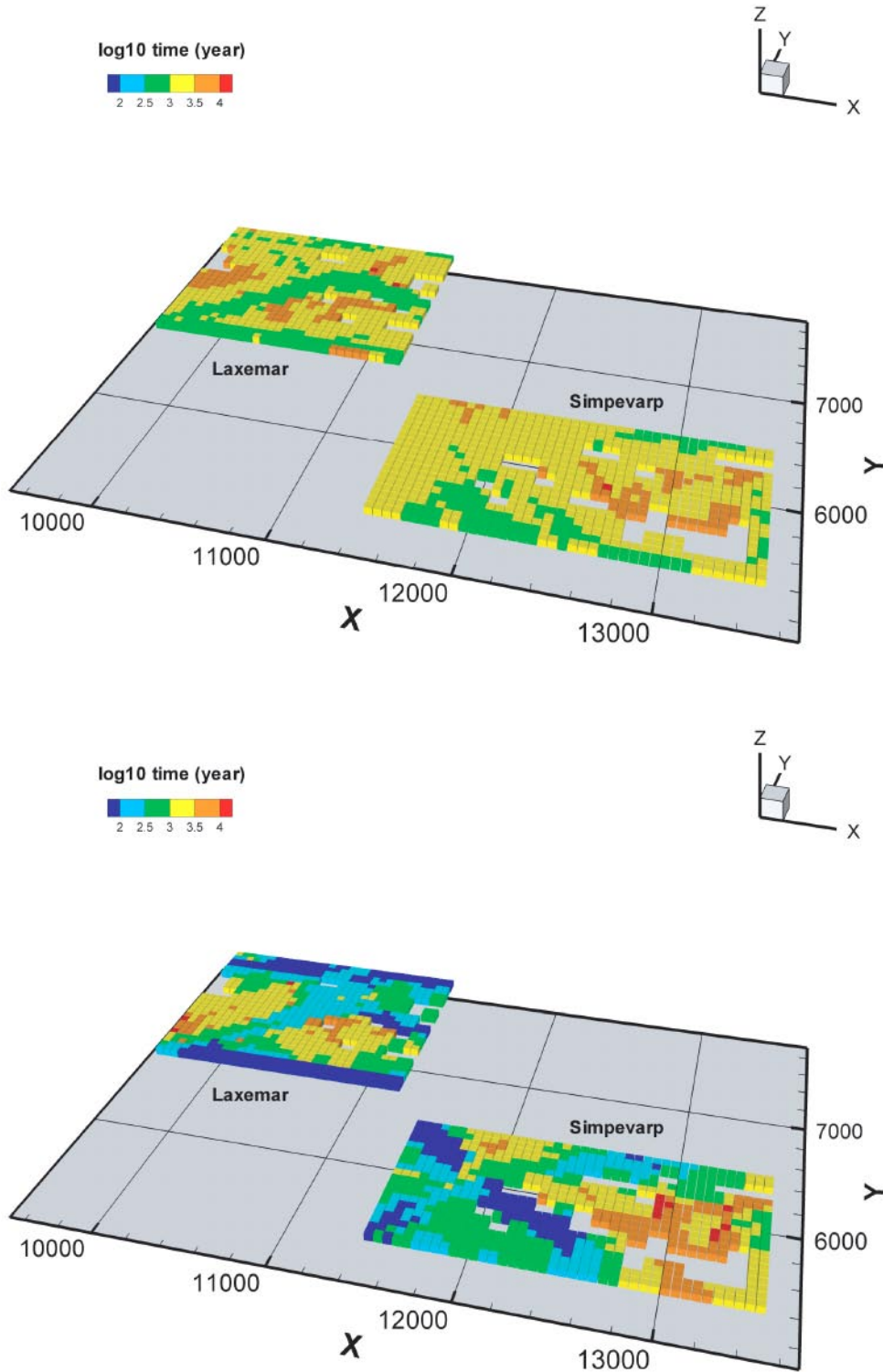
Figure 6-10. Comparison of calculated travel times, reported at each starting position, for Model #3 (sensitivity case; top) and Model #5 (Base Case; bottom). Empty cells indicate positions where no particles were released.

position for this parameter. This is further illustrated in Figure 6-11, which shows that the travel time distributions obtained for the sensitivity case (left column) are narrower than those for the Base Case (right column).

In addition, Figure 6-11 shows that the distributions for the sensitivity case have marked peaks, whereas the Base Case distributions are more uniform. Thus, the time required for the particles to penetrate the more low-permeable, uniform uppermost layer in Model #3 determines (and increases) the shortest travel times, whereas the longest travel times remain more or less unchanged compared to the Base Case.
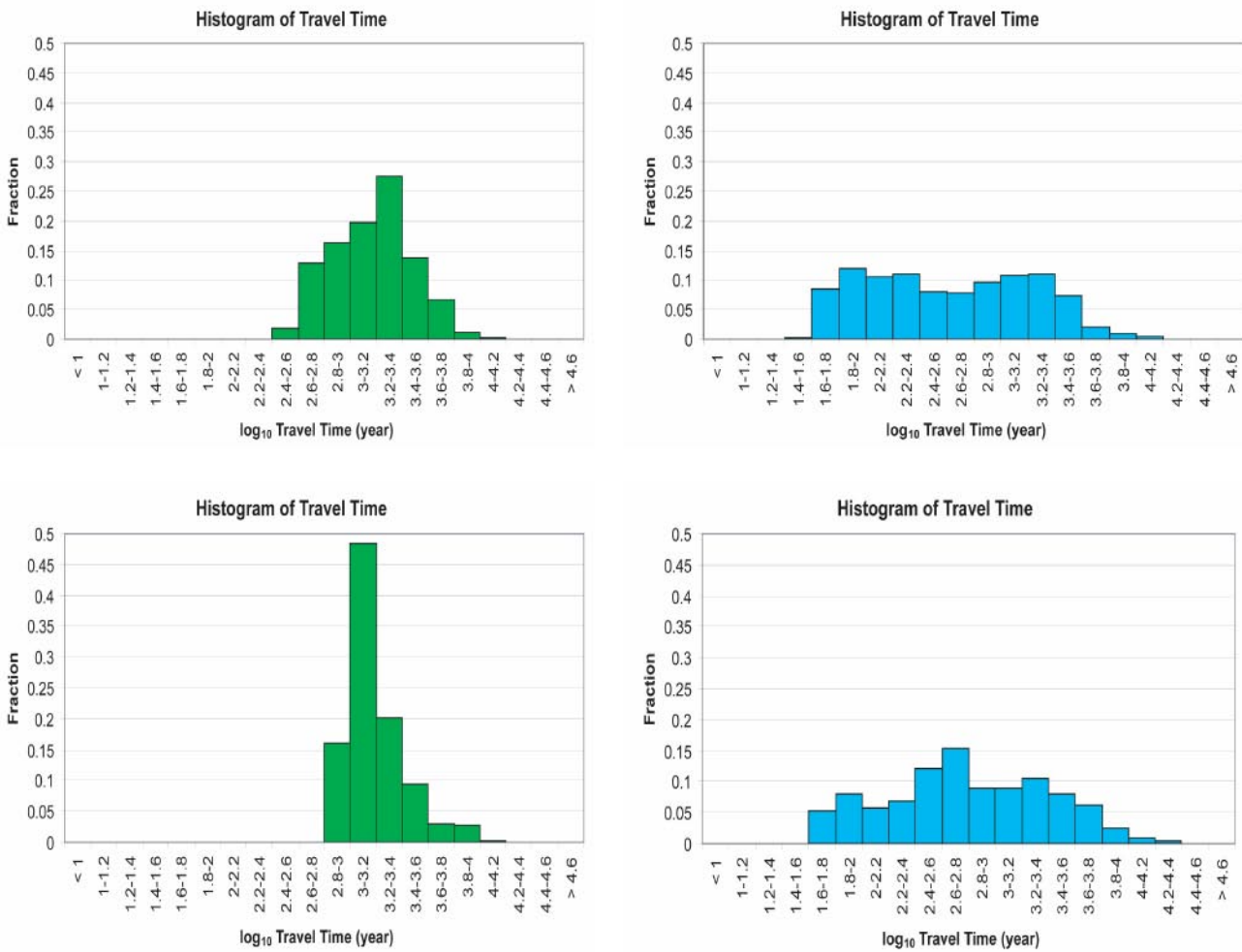
Figure 6-11. *Histograms of calculated t_w-distributions for Model #3 (sensitivity case; left column) and Model #5 (Base Case; right column); upper row: Laxemar release area, lower row: Simpevarp release area.*

Table 6-2 shows a comparison of the statistics of F, t_w and q (Darcy fluxes at starting positions). Generally, the characteristic F- and t_w-values are larger for Model #3 than for Model #5 (Base Case), whereas the Darcy fluxes are smaller (Laxemar release area) or do not change significantly (Simpevarp). Furthermore, the increase in the median values of F and t_w is somewhat larger for the Laxemar release area than for the Simpevarp area, which indicates a higher sensitivity to the properties of the uppermost layer for the "inland" release area.

As discussed above, the variability in travel times is smaller for the sensitivity case; Table 6-2 shows that this applies also to F. Specifically, it can be seen in the table that the values for the 5th percentiles of t_w and F are much higher for Model #3 than for Model #5. It can also be noted that the effects on the 95th percentiles of t_w and F are different for the two release areas; the values obtained for the sensitivity case are higher for the Laxemar release area and lower for the Simpevarp area relative to the Base Case.

Table 6-2. Comparison of particle tracking results for Model #5 (Base Case) and Model #3 (sensitivity case addressing the treatment of the superficial rock layer).

F (y/m)	Laxemar release area		Simpevarp release area	
	Model #3	**Model #5**	**Model #3**	**Model #5**
$F_{5\%}$	$4.8 \cdot 10^4$	$3.3 \cdot 10^3$	$6.5 \cdot 10^4$	$4.9 \cdot 10^3$
$F_{50\%}$	$2.1 \cdot 10^5$	$6.4 \cdot 10^4$	$1.6 \cdot 10^5$	$1.0 \cdot 10^5$
$F_{95\%}$	$1.3 \cdot 10^6$	$1.2 \cdot 10^6$	$1.3 \cdot 10^6$	$1.4 \cdot 10^6$
$(F_{95\%} - F_{5\%}) / F_{50\%}$	6.0	18.7	7.7	14.0

t_w (y)	Laxemar release area		Simpevarp release area	
	Model #3	**Model #5**	**Model #3**	**Model #5**
$t_{w,5\%}$	450	50	900	60
$t_{w,50\%}$	1,560	390	1,320	560
$t_{w,95\%}$	4,380	3,340	4,920	5,740
$(t_{w,95\%} - t_{w,5\%}) / t_{w,50\%}$	2.5	8.4	3.0	10.1

q (m/s)	Laxemar release area		Simpevarp release area	
	Model #3	**Model #5**	**Model #3**	**Model #5**
$q_{5\%}$	$1.1 \cdot 10^{-13}$	$1.2 \cdot 10^{-13}$	$3.6 \cdot 10^{-14}$	$3.9 \cdot 10^{-14}$
$q_{50\%}$	$6.8 \cdot 10^{-12}$	$1.3 \cdot 10^{-11}$	$4.5 \cdot 10^{-12}$	$3.4 \cdot 10^{-12}$
$q_{95\%}$	$3.9 \cdot 10^{-10}$	$8.2 \cdot 10^{-10}$	$2.1 \cdot 10^{-10}$	$2.5 \cdot 10^{-10}$
$(q_{95\%} - q_{5\%}) / q_{50\%}$	57.3	63.1	46.7	73.5

6.6   Sensitivity to the initial position of the salinity interface

In this sensitivity case, the effects of the initial position of the salinity interface on flow paths and transport parameters are investigated. Specifically, the sensitivity case (Model #7) prescribed a more shallow position of this interface in the initial conditions for the transient flow simulation, resulting in higher initial salinities in the upper part of the rock than in the Base Case (Model #5). Thus, the differences between this sensitivity case and the Base Case depend on to what extent the modelled present flow fields used in the particle tracking simulations are affected by the initial conditions in the transient flow simulations. The sensitivity of the present-day flow situation to the initial conditions is discussed in Section 5.2.

Figure 6-12 shows that there is a tendency towards longer flow paths for the sensitivity case, as compared to the Base Case. This effect can be observed for both release areas, but appears to be more pronounced for the Simpevarp area. This implies that the path lengths for the particles from the release area located closest to the coastline are more sensitive to the initial position of the salinity interface. The increase in path lengths for the Laxemar release area can be considered as relatively small, and is not consistent within the release area (path lengths decrease for some starting positions).

Essentially, the same observations can be made when comparing travel times in Figure 6-13. Thus, the overall impression is that travel times are larger for the sensitivity case, and that the increase is larger and more consistent among the different starting positions for the Simpevarp release area. Concerning the travel times from the Simpevarp release area, it can also be noted that they primarily increase for starting positions in the western part of the area.

Statistics of F, t_w and q for the present sensitivity case (Model #7) and the Base Case (Model #5) are summarised in Table 6-3. Generally, the differences in the various performance measures imposed by the more shallow initial salinity interface can be characterised as small. Focusing on the median values, it can be noted that the effect on the travel times, as indicated by the graphical presentation in Figure 6-13, is larger for the Simpevarp release area. For the F-values, qualitatively different effects of the changed initial condition are obtained; the median of F decreases for Laxemar and increases for Simpevarp.

The variability in F- and t_w-values for the released particles shows relatively small differences, at least for the Laxemar release area. However, for the Laxemar area the variability is larger for the sensitivity case than for the Base Case, whereas the opposite is observed for the Simpevarp release.

The median values of the Darcy fluxes appear not to be sensitive to the initial position of the salinity interface, whereas the variability in this parameter is lower for the sensitivity case than for the Base Case. It should be noted that the Darcy flux can be expected to show some differences in its sensitivity to the various parameter variations studied, because it is a "point" parameter and not an integrated parameter such as F and t_w.
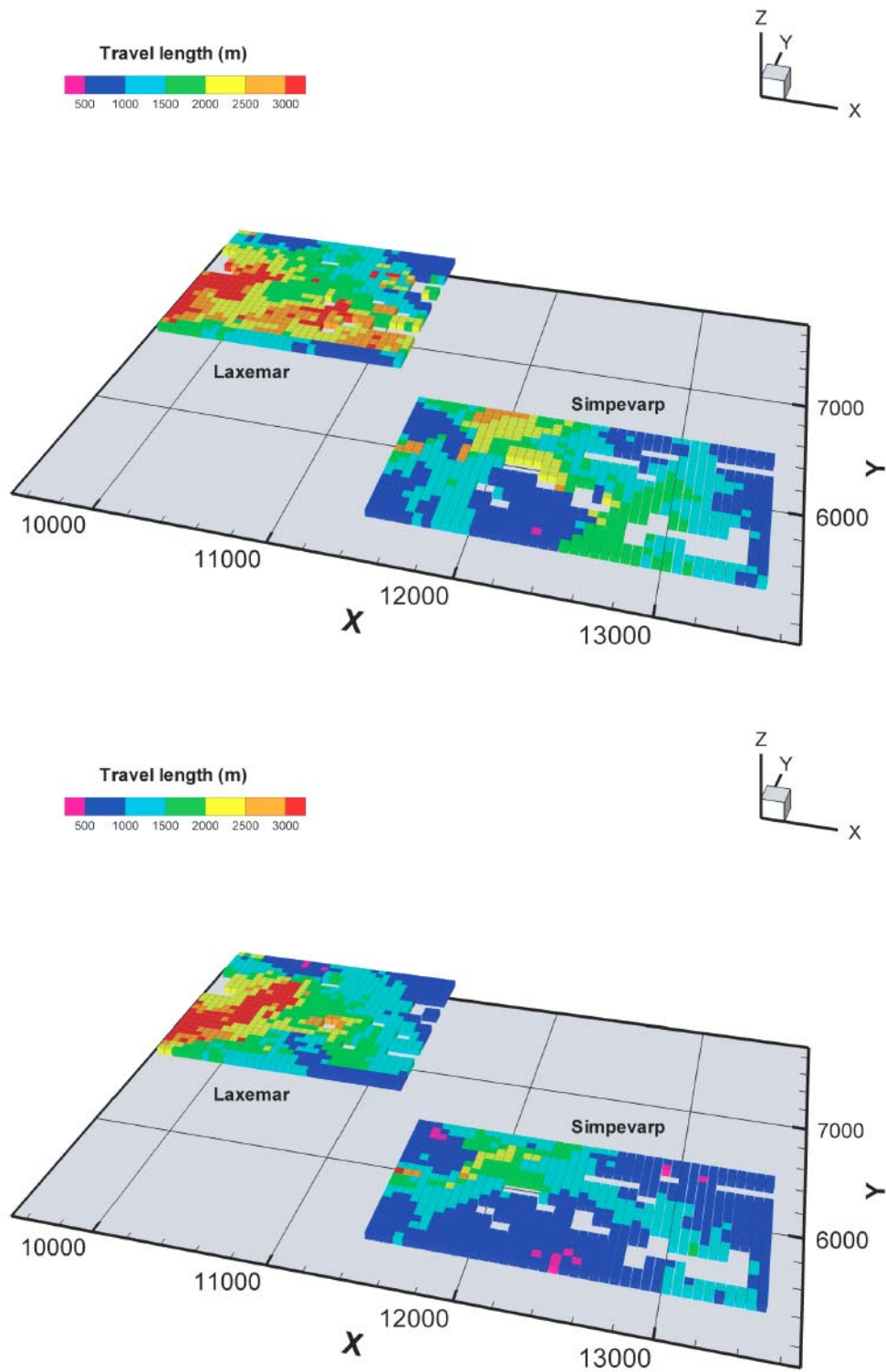
Figure 6-12. *Comparison of calculated flow path lengths, reported at each starting position, for Model #7 (sensitivity case; top) and Model #5 (Base Case; bottom). Empty cells indicate positions where no particles were released.*
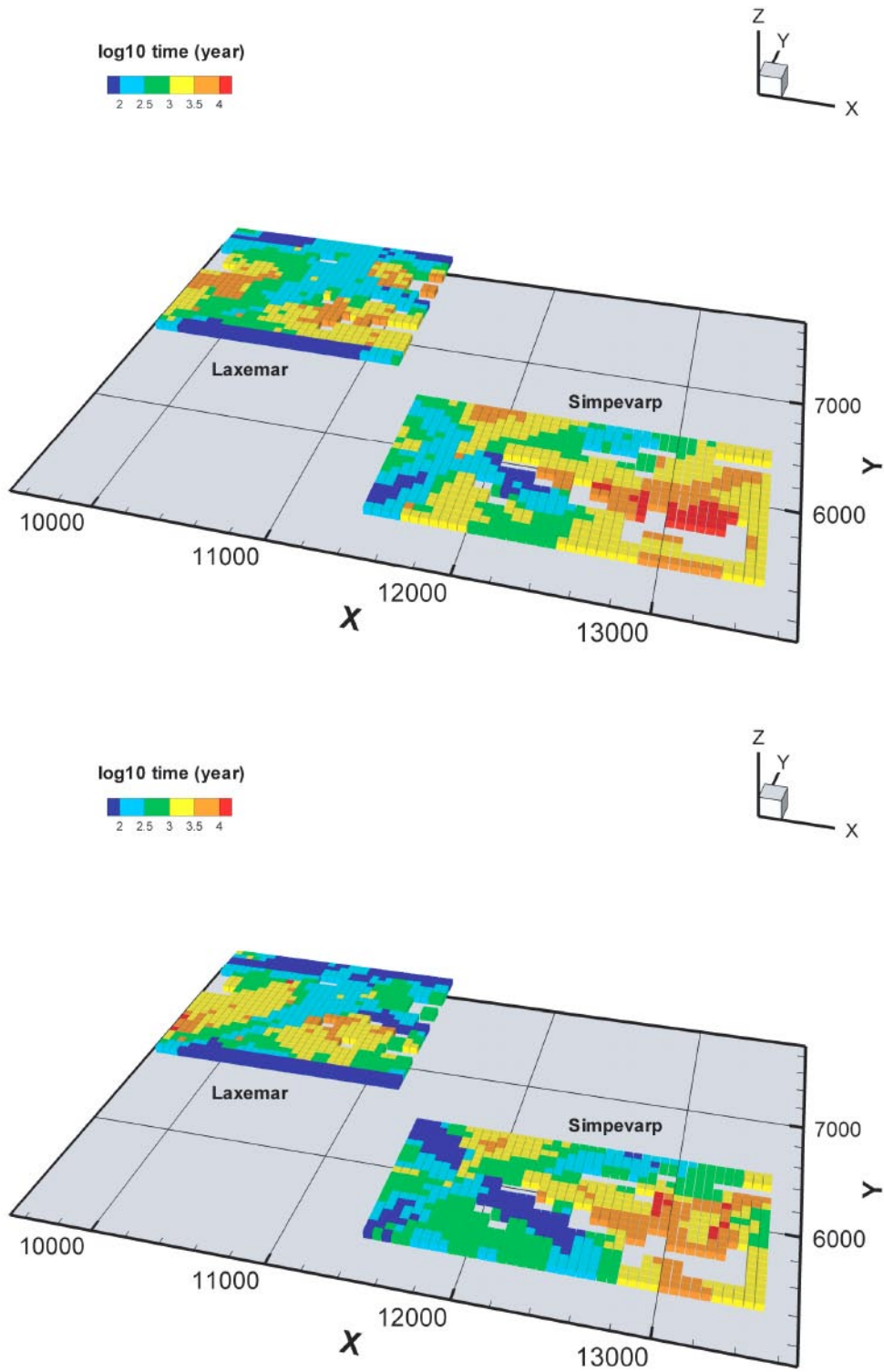
Figure 6-13. Comparison of calculated travel times, reported at each starting position, for Model #7 (sensitivity case; top) and Model #5 (Base Case; bottom). Empty cells indicate positions where no particles were released.

Table 6-3. Comparison of particle tracking results for Model #5 (Base Case) and Model #7 (sensitivity case addressing the initial position of the salinity interface).

F (y/m)	Laxemar release area		Simpevarp release area	
	Model #7	Model #5	Model #7	Model #5
$F_{5\%}$	$4.6 \cdot 10^3$	$3.3 \cdot 10^3$	$8.3 \cdot 10^3$	$4.9 \cdot 10^3$
$F_{50\%}$	$5.1 \cdot 10^4$	$6.4 \cdot 10^4$	$1.7 \cdot 10^5$	$1.0 \cdot 10^5$
$F_{95\%}$	$1.0 \cdot 10^6$	$1.2 \cdot 10^6$	$1.8 \cdot 10^6$	$1.4 \cdot 10^6$
$(F_{95\%} - F_{5\%}) / F_{50\%}$	19.5	18.7	10.5	14.0

t_w (y)	Laxemar release area		Simpevarp release area	
	Model #7	Model #5	Model #7	Model #5
$t_{w,5\%}$	70	50	110	60
$t_{w,50\%}$	450	390	1,260	560
$t_{w,95\%}$	4,630	3,340	8,280	5,740
$(t_{w,95\%} - t_{w,5\%}) / t_{w,50\%}$	10.1	8.4	6.5	10.1

q (m/s)	Laxemar release area		Simpevarp release area	
	Model #7	Model #5	Model #7	Model #5
$q_{5\%}$	$1.0 \cdot 10^{-13}$	$1.2 \cdot 10^{-13}$	$1.4 \cdot 10^{-14}$	$3.9 \cdot 10^{-14}$
$q_{50\%}$	$1.4 \cdot 10^{-11}$	$1.3 \cdot 10^{-11}$	$3.4 \cdot 10^{-12}$	$3.4 \cdot 10^{-12}$
$q_{95\%}$	$6.0 \cdot 10^{-10}$	$8.2 \cdot 10^{-10}$	$1.4 \cdot 10^{-10}$	$2.5 \cdot 10^{-10}$
$(q_{95\%} - q_{5\%}) / q_{50\%}$	42.8	63.1	41.2	73.5

6.7 Sensitivity to a smaller regional model domain

This sensitivity case investigated the sensitivity of the flow paths and transport parameters to the position of the western boundary of the groundwater flow model. The flow model used to produce the sensitivity case flow paths (Model #8) had its western boundary at the regional water divide, see Figure 6-1, instead of further west at the boundary of the regional Simpevarp model domain (Model #5, Base Case). Thus, a smaller model was used for the sensitivity case simulation.

Inspections of visualisations similar to those discussed in the preceding sections showed that neither path lengths nor travel times changed much in response to the shift of the western model boundary. Essentially, only a few cells/particles in each release area indicated differences in parameter values when comparing the sensitivity case to the Base Case. Hence, the visualisations do not provide much useful information for the evaluation of this sensitivity case, except the overall observation that the effects are small. Therefore, they are not presented here. The numerical values of the particle tracking statistics are required to enable a rational evaluation of this sensitivity case.

The summary of the particle tracking results in Table 6-4 confirms that the effects of the investigated change in the location of the western boundary are small; the differences between the sensitivity case and the Base Case are generally less than 10%, for many parameters less than 5%. However, it may be worth noting that the effects on the median values of F and t_w are different for the two release areas; these parameters increase for Laxemar and decrease for Simpevarp as the size of the model is reduced.

Table 6-4. Comparison of particle tracking results for Model #5 (Base Case) and Model #8 (sensitivity case addressing the position of the western model boundary).

F (y/m)	Laxemar release area		Simpevarp release area	
	Model #8	Model #5	Model #8	Model #5
$F_{5\%}$	$3.2 \cdot 10^3$	$3.3 \cdot 10^3$	$5.2 \cdot 10^3$	$4.9 \cdot 10^3$
$F_{50\%}$	$7.0 \cdot 10^4$	$6.4 \cdot 10^4$	$9.4 \cdot 10^4$	$1.0 \cdot 10^5$
$F_{95\%}$	$1.3 \cdot 10^6$	$1.2 \cdot 10^6$	$1.6 \cdot 10^6$	$1.4 \cdot 10^6$
$(F_{95\%} - F_{5\%}) / F_{50\%}$	18.5	18.7	17.0	14.0

t_w (y)	Laxemar release area		Simpevarp release area	
	Model #8	Model #5	Model #8	Model #5
$t_{w,5\%}$	50	50	60	60
$t_{w,50\%}$	400	390	540	560
$t_{w,95\%}$	3,430	3,340	6,610	5,740
$(t_{w,95\%} - t_{w,5\%}) / t_{w,50\%}$	8.4	8.4	12.1	10.1

q (m/s)	Laxemar release area		Simpevarp release area	
	Model #8	Model #5	Model #8	Model #5
$q_{5\%}$	$9.0 \cdot 10^{-14}$	$1.2 \cdot 10^{-13}$	$2.0 \cdot 10^{-14}$	$3.9 \cdot 10^{-14}$
$q_{50\%}$	$1.3 \cdot 10^{-11}$	$1.3 \cdot 10^{-11}$	$3.5 \cdot 10^{-12}$	$3.4 \cdot 10^{-12}$
$q_{95\%}$	$8.2 \cdot 10^{-10}$	$8.2 \cdot 10^{-10}$	$2.6 \cdot 10^{-10}$	$2.5 \cdot 10^{-10}$
$(q_{95\%} - q_{5\%}) / q_{50\%}$	63.1	63.1	74.3	73.5

6.8   Sensitivity to the deformation zone flow porosity

In the sensitivity case, the flow porosity of all deformation zones, both deterministically and stochastically modelled zones, was reduced to 20% of the value used in the Base Case (cf Table 3-4). As described in Section 5.4, this implies a proportional reduction of the amount of mobile water in the model, affecting the mobile-immobile zone interactions and hence the transient flow during the simulated time period resulting in the present-day flow field. The effects on path lengths and Darcy fluxes depend on whether the change in flow porosity has significant effects on the modelled present flow field, whereas a reduction of the porosity would lead to smaller travel times and F-values also in a fixed flow field.

Figure 6-14 indicates some differences in the sensitivity of the path lengths to the flow porosity for the two release areas. The Laxemar area contains both sub-areas of increasing paths lengths (in the western part) and sub-areas showing decreasing path lengths (in the eastern part). Conversely, there appears to be a general increase in path lengths for particles released within the Simpevarp area.

As shown in Figure 6-15, the travel times of particles from the Laxemar release area decrease at many starting positions, although the changes perhaps are smaller than might expected based on the porosity reduction alone. Also for the Simpevarp release area, the overall impression is that of reduced travel times, but there are also sub-areas where travel times increase. The main directly observable effect for the Simpevarp release is that the variability in travel times decreases (both the areas of the smallest values and those of the largest decrease significantly).
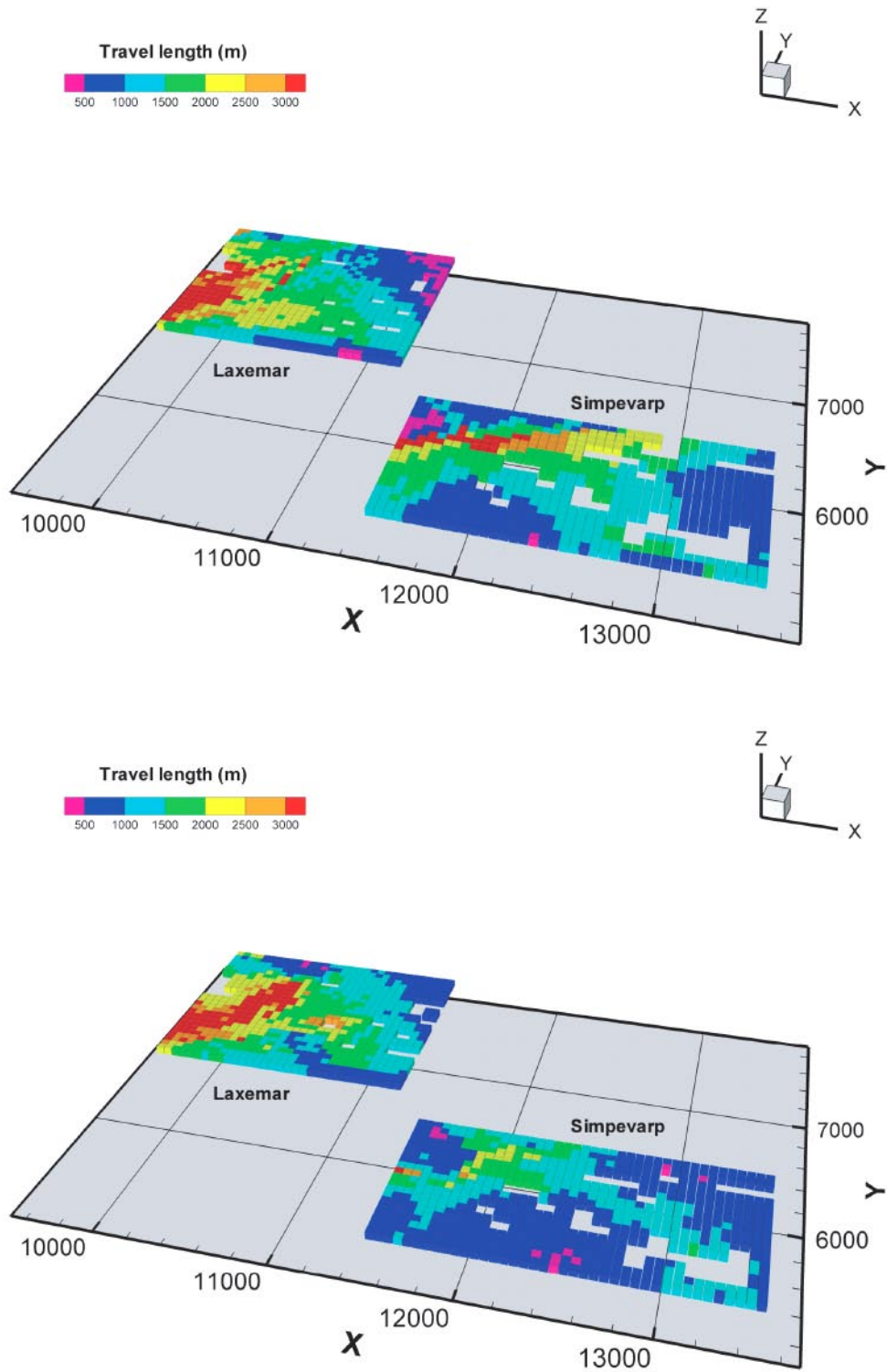
Figure 6-14. *Comparison of calculated flow path lengths, reported at each starting position, for Model #9 (sensitivity case; top) and Model #5 (Base Case; bottom). Empty cells indicate positions where no particles were released.*
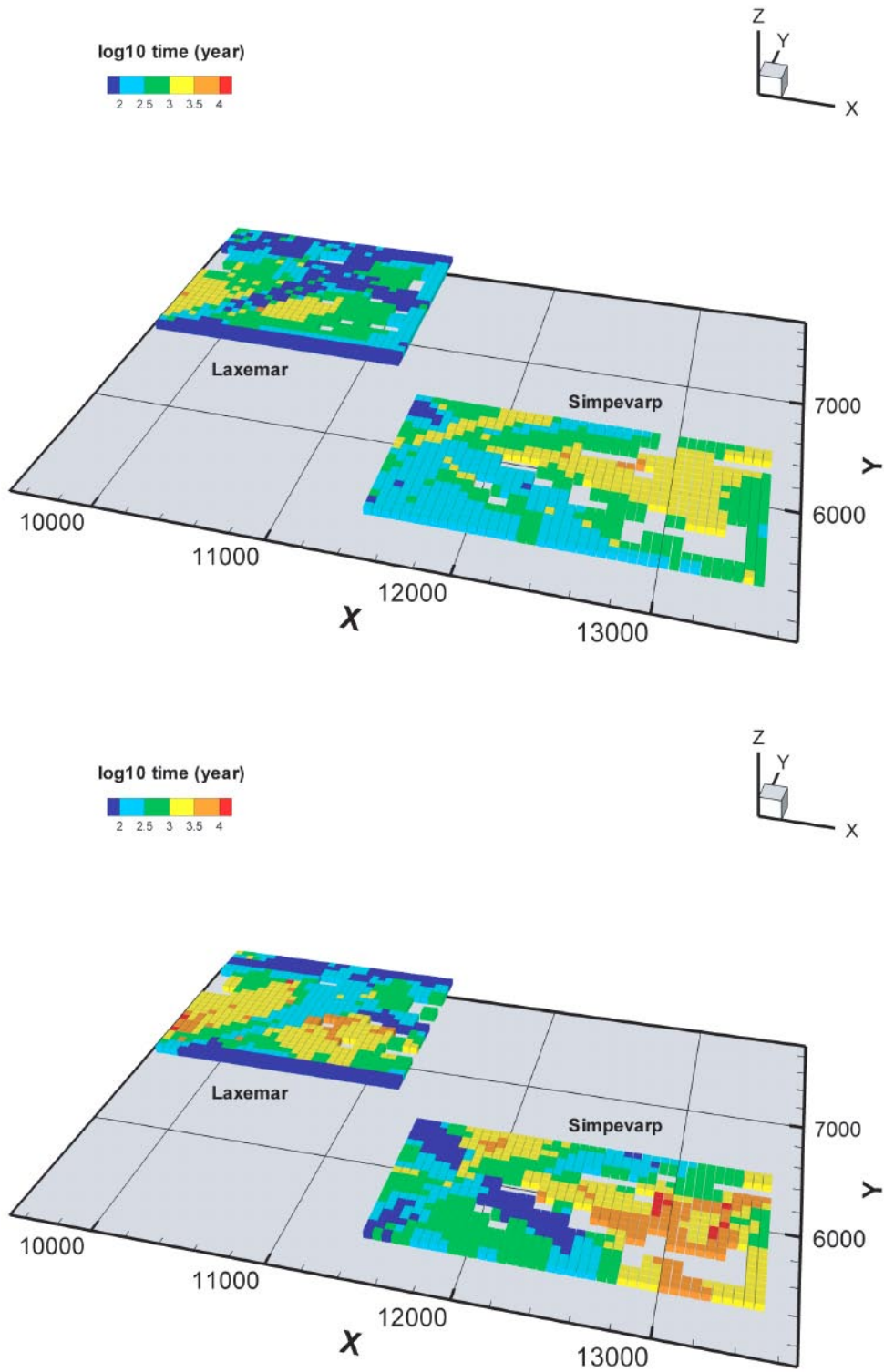
Figure 6-15. *Comparison of calculated travel times, reported at each starting position, for Model #9 (sensitivity case; top) and Model #5 (Base Case; bottom). Empty cells indicate positions where no particles were released.*

The summary of the particle tracking results in Table 6-5 shows that the median values of F and t_w decrease for both release areas (more for Laxemar) when the flow porosity decreases, whereas the median Darcy fluxes increase (more for Simpevarp). Regarding F and t_w, however, it should be noted that the reductions are much smaller than that of the flow porosity (reduced to 20% of the Base Case value). Spatial variability, as quantified by the normalised difference between the 95th and 5th percentiles, is generally smaller for the sensitivity case than for the Base Case. The decrease in spatial variability is largest for the Simpevarp release area.

Table 6-5. Comparison of particle tracking results for Model #5 (Base Case) and Model #9 (sensitivity case addressing the flow porosity).

F (y/m)	Laxemar release area		Simpevarp release area	
	Model #9	Model #5	Model #9	Model #5
$F_{5\%}$	$3.8 \cdot 10^3$	$3.3 \cdot 10^3$	$1.7 \cdot 10^4$	$4.9 \cdot 10^3$
$F_{50\%}$	$3.6 \cdot 10^4$	$6.4 \cdot 10^4$	$7.0 \cdot 10^4$	$1.0 \cdot 10^5$
$F_{95\%}$	$3.1 \cdot 10^5$	$1.2 \cdot 10^6$	$3.5 \cdot 10^5$	$1.4 \cdot 10^6$
$(F_{95\%}-F_{5\%}) / F_{50\%}$	8.5	18.7	4.8	14.0

t_w (y)	Laxemar release area		Simpevarp release area	
	Model #9	Model #5	Model #9	Model #5
$t_{w,5\%}$	20	50	120	60
$t_{w,50\%}$	200	390	500	560
$t_{w,95\%}$	1,480	3,340	2,210	5,740
$(t_{w,95\%}-t_{w,5\%}) / t_{w,50\%}$	7.3	8.4	4.2	10.1

q (m/s)	Laxemar release area		Simpevarp release area	
	Model #9	Model #5	Model #9	Model #5
$q_{5\%}$	$7.5 \cdot 10^{-12}$	$1.2 \cdot 10^{-13}$	$1.9 \cdot 10^{-12}$	$3.9 \cdot 10^{-14}$
$q_{50\%}$	$1.5 \cdot 10^{-11}$	$1.3 \cdot 10^{-11}$	$5.7 \cdot 10^{-12}$	$3.4 \cdot 10^{-12}$
$q_{95\%}$	$7.6 \cdot 10^{-10}$	$8.2 \cdot 10^{-10}$	$2.0 \cdot 10^{-10}$	$2.5 \cdot 10^{-10}$
$(q_{95\%}-q_{5\%}) / q_{50\%}$	50.2	63.1	34.8	73.5

6.9   Sensitivity to the DFN realisation

The sensitivity to the DFN realisation was investigated by performing the whole sequence of flow and particle tracking simulations for another DFN realisation (Model #12) generated with the same input parameters as the Base Case (Model #5). As explained above, deformation zones in the size (length) range of 100 m to 1,000 m are modelled stochastically in the present study, whereas zones larger than 1,000 m are modelled deterministically. By considering a different DFN realisation, another set of stochastically modelled structures is created and used, together with the deterministically modelled structures, to calculate the grid cell conductivities in the groundwater flow model. It follows that the contribution from the stochastic structures to the hydraulic conductivity of a particular cell is different in the two realisations, and that the (relative) differences in the local conductivity values are largest outside the (unchanged) deterministic zones.

By comparing the results of two realisations obtained from the same basic input, the uncertainty in flow paths and transport parameters related to the stochastically modelled spatial variability can be assessed. The sensitivity to the DFN realisation, and hence the uncertainty, will be different for different parameters and performance measures, e.g. larger for parameters associated with a particular starting position than for summary statistics for all particles released.

The path lengths resulting from particle tracking in the two flow fields obtained from the two DFN realisations are compared in Figure 6-16. The overall impression is that path lengths are smaller for the sensitivity case than for the Base Case. However, it can also be observed that the reduction is not consistent within the release areas; both areas contain cells where larger path lengths are obtained for the sensitivity case. Perhaps more important, it can be noted that spatial patterns are similar, illustrating the significance of the deterministic zones for the flow paths.

Similar observations can be made for the travel times visualised in Figure 6-17, however, with some differences between the two release areas. The sensitivity case yields smaller travel times for most starting positions within the Laxemar area, whereas the Simpevarp area contains a relatively large number of positions where travel times increase. This is reflected in the statistics presented in Table 6-6; the median travel time for Model #12 is smaller for the Laxemar release area and larger for the Simpevarp area, as compared to Model #5. Similar results are obtained for the F parameter. However, the most important observation is not the particular effects obtained for the two areas (or which area is "best"), but that the overall effects for the two areas can be qualitatively different.

For the Laxemar release area, the spatial variability in F and t_w is larger for Model #12 than for Model #5, whereas the opposite holds for the Simpevarp area. The change in the considered measure of variability is larger for the Simpevarp release. The differences between the Darcy flux statistics for the two cases are relatively small (except for the 5th percentiles), thereby indicating a lower sensitivity to the DFN realisation for the point parameter q than for the integrated parameters F and t_w.
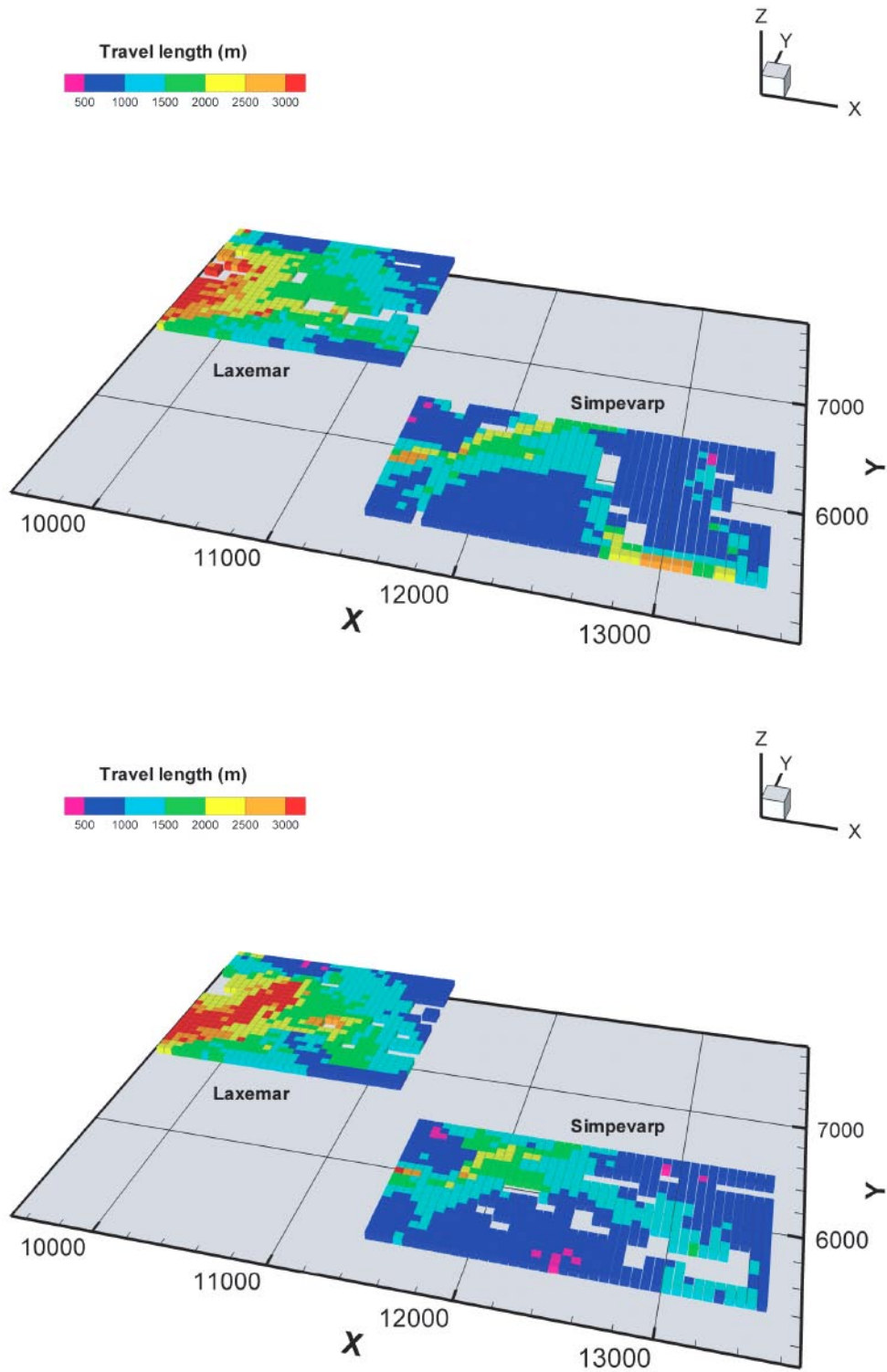
Figure 6-16. Comparison of calculated flow path lengths, reported at each starting position, for Model #12 (sensitivity case; top) and Model #5 (Base Case; bottom). Empty cells indicate positions where no particles were released.
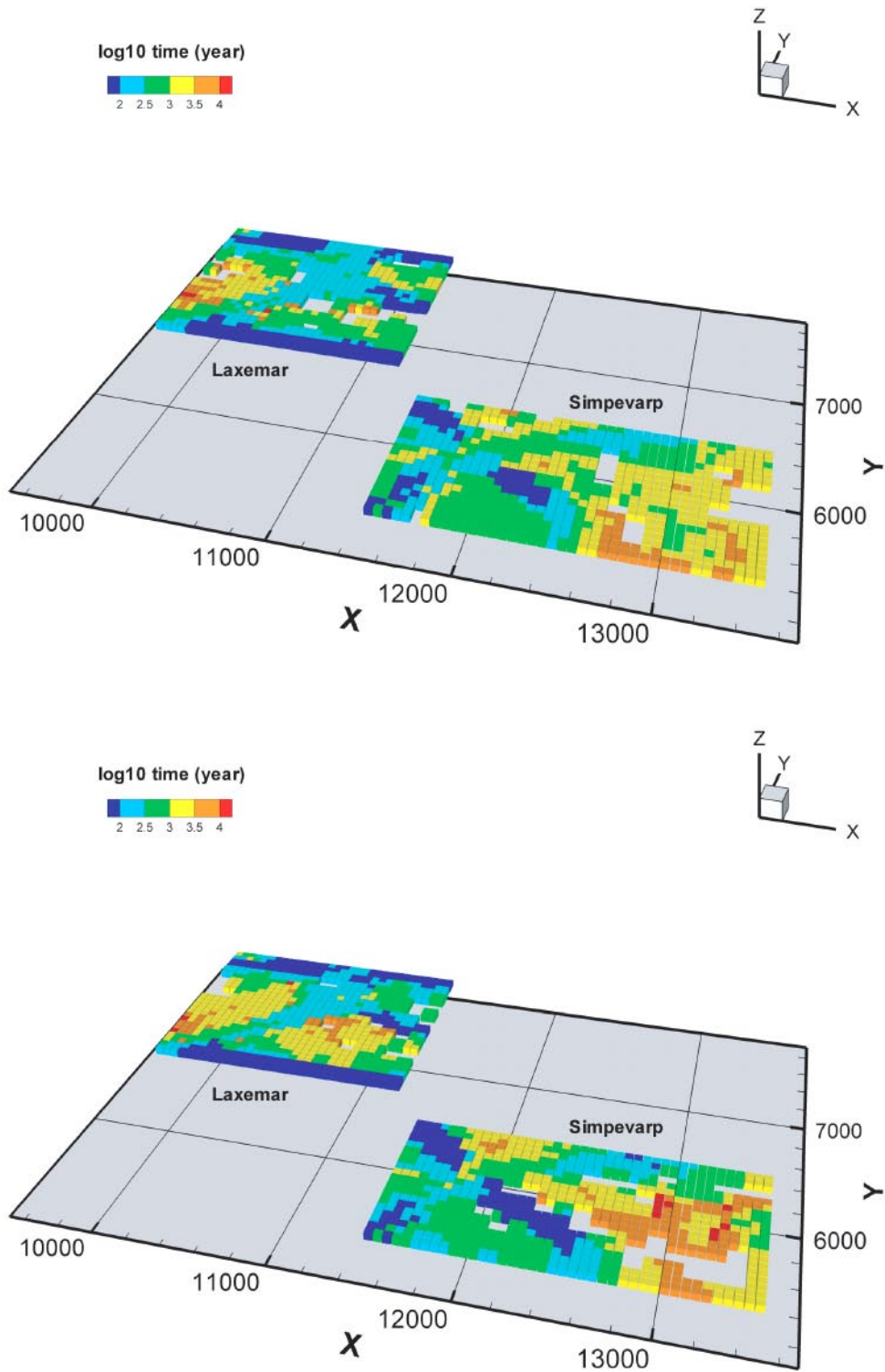
Figure 6-17. *Comparison of calculated travel times, reported at each starting position, for Model #12 (sensitivity case; top) and Model #5 (Base Case; bottom). Empty cells indicate positions where no particles were released.*

Table 6-6. Comparison of particle tracking results for Model #5 (Base Case) and Model #12 (sensitivity case addressing the DFN realisation).

F (y/m)	Laxemar release area		Simpevarp release area	
	Model #12	Model #5	Model #12	Model #5
$F_{5\%}$	$3.0 \cdot 10^3$	$3.3 \cdot 10^3$	$7.2 \cdot 10^3$	$4.9 \cdot 10^3$
$F_{50\%}$	$2.8 \cdot 10^4$	$6.4 \cdot 10^4$	$1.5 \cdot 10^5$	$1.0 \cdot 10^5$
$F_{95\%}$	$7.9 \cdot 10^5$	$1.2 \cdot 10^6$	$9.6 \cdot 10^5$	$1.4 \cdot 10^6$
$(F_{95\%} - F_{5\%}) / F_{50\%}$	28.1	18.7	6.4	14.0

| t_w (y)	Laxemar release area		Simpevarp release area	
	Model #12	Model #5	Model #12	Model #5
$t_{w,5\%}$	60	50	90	60
$t_{w,50\%}$	300	390	790	560
$t_{w,95\%}$	3,340	3,340	3,220	5,740
$(t_{w,95\%} - t_{w,5\%}) / t_{w,50\%}$	10.9	8.4	4.0	10.1

q (m/s)	Laxemar release area		Simpevarp release area	
	Model #12	Model #5	Model #12	Model #5
$q_{5\%}$	$2.6 \cdot 10^{-13}$	$1.2 \cdot 10^{-13}$	$1.1 \cdot 10^{-13}$	$3.9 \cdot 10^{-14}$
$q_{50\%}$	$1.5 \cdot 10^{-11}$	$1.3 \cdot 10^{-11}$	$3.1 \cdot 10^{-12}$	$3.4 \cdot 10^{-12}$
$q_{95\%}$	$7.3 \cdot 10^{-10}$	$8.2 \cdot 10^{-10}$	$1.9 \cdot 10^{-10}$	$2.5 \cdot 10^{-10}$
$(q_{95\%} - q_{5\%}) / q_{50\%}$	48.6	63.1	61.3	73.5

6.10 Sensitivity to the transmissivities of the stochastic structures

This sensitivity case (Model #13) investigated the sensitivity to the hydraulic properties of the stochastically modelled deformation zones. Specifically, the transmissivities of all stochastic structures were reduced to 1/10 of their values in the Base Case. No changes were made in the parameters describing the properties of the deterministic zones. Thus, the sensitivity case had a larger transmissivity contrast between stochastic and deterministic zones, thereby increasing the "preferential flow effect" associated with the latter. The expected effects on the transport parameters would be increases in F-values and travel times for particles with starting positions in stochastic structures, and decreasing Darcy fluxes at these starting positions.

Figure 6-18 shows that the differences in path lengths between the two cases generally can be regarded as fairly small, indicating a limited effect of the flow path pattern. Both increases (e.g. in the westernmost part of the Laxemar area) and decreases (e.g. the eastern part of the Simpevarp area) can be observed.

The travel times, Figure 6-19, increase for many starting positions within both release areas. A more detailed comparison, involving the locations of the deterministic zones (Figure 6-1), reveals that the increases in travel times concern the particles released outside the deterministic zones. Therefore, the areas of the shortest travel times (blue cells) are unaffected, whereas increases can be noted primarily in areas of intermediate Base Case travel times (green cells shifting to yellow, yellow/orange to red).
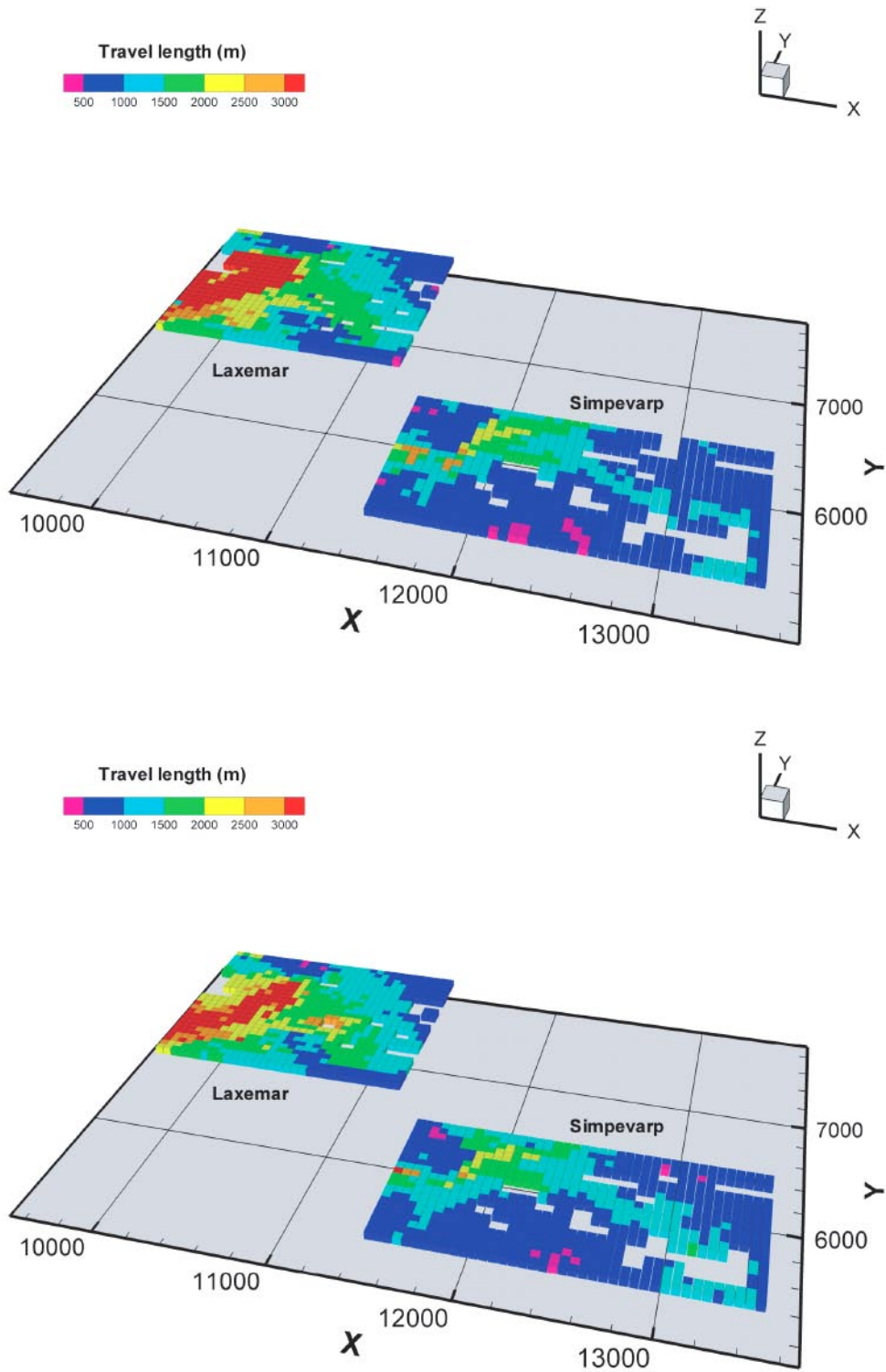
Figure 6-18. Comparison of calculated flow path lengths, reported at each starting position,
for Model #13 (sensitivity case; top) and Model #5 (Base Case; bottom). Empty cells indicate
positions where no particles were released.
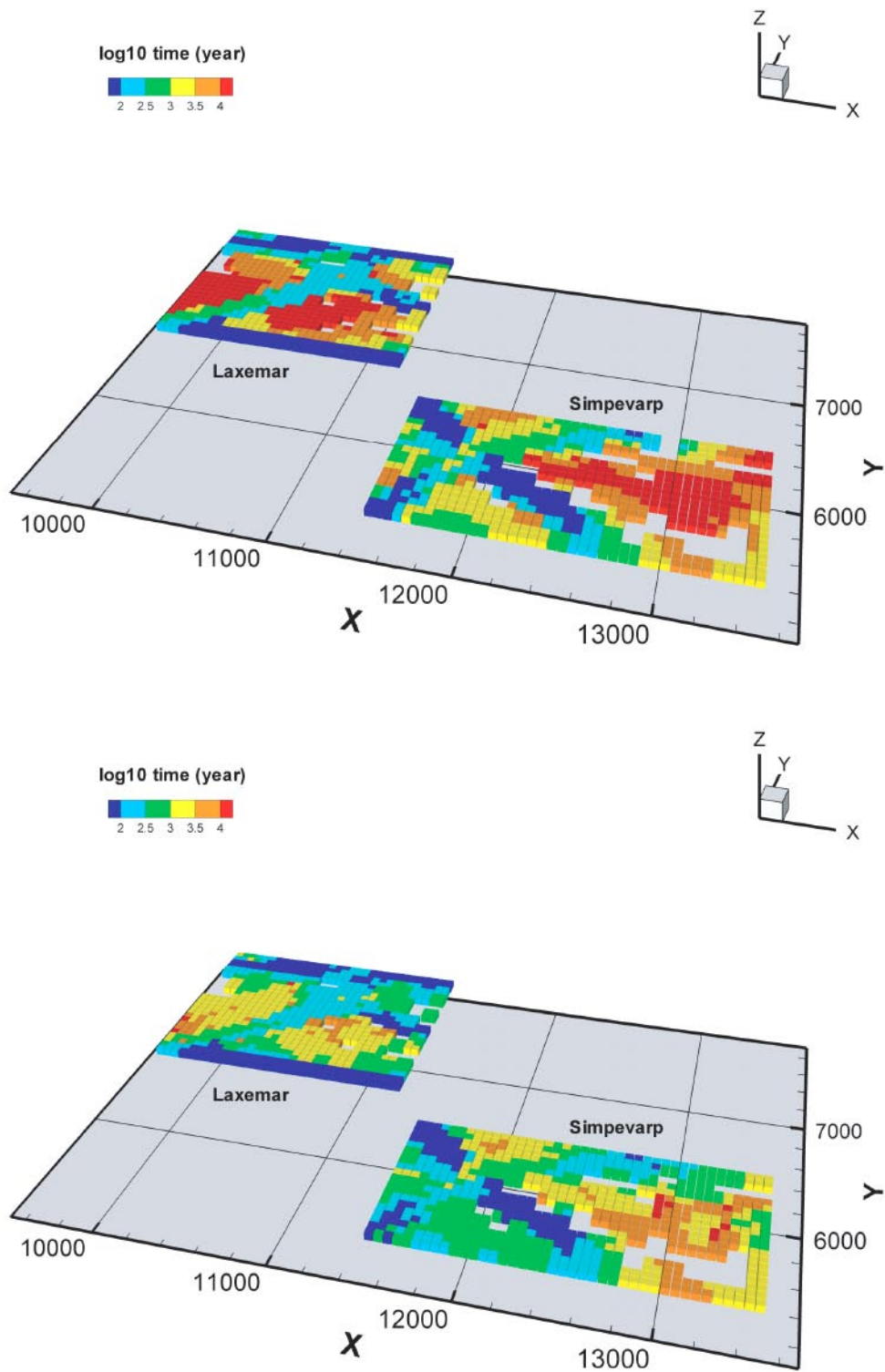
Figure 6-19. Comparison of calculated travel times, reported at each starting position, for Model #13 (sensitivity case; top) and Model #5 (Base Case; bottom). Empty cells indicate positions where no particles were released.

The particle tracking results in Table 6-7 show an increase in F- and t_w-values for the sensitivity case, except for the 5th percentiles representing starting positions in the largest zones, and a decrease in the Darcy fluxes. The increases in the median values of F and t_w are largest for the Simpevarp release area. Furthermore, it is noted that the spatial variability is larger for Model #13 than for Model #5, which is consistent with the increasing contrast in hydraulic properties associated with the sensitivity case.

Table 6-7. Comparison of particle tracking results for Model #5 (Base Case) and Model #13 (sensitivity case addressing the transmissivities of the stochstic structures).

F (y/m)	Laxemar release area		Simpevarp release area	
	Model #13	Model #5	Model #13	Model #5
$F_{5\%}$	$3.2 \cdot 10^3$	$3.3 \cdot 10^3$	$4.9 \cdot 10^3$	$4.9 \cdot 10^3$
$F_{50\%}$	$1.1 \cdot 10^5$	$6.4 \cdot 10^4$	$2.1 \cdot 10^5$	$1.0 \cdot 10^5$
$F_{95\%}$	$8.4 \cdot 10^6$	$1.2 \cdot 10^6$	$8.5 \cdot 10^6$	$1.4 \cdot 10^6$
$(F_{95\%} - F_{5\%}) / F_{50\%}$	76.3	18.7	40.4	14.0

t_w (y)	Laxemar release area		Simpevarp release area	
	Model #13	Model #5	Model #13	Model #5
$t_{w,5\%}$	50	50	60	60
$t_{w,50\%}$	580	390	1,610	560
$t_{w,95\%}$	18,000	3,340	18,220	5,740
$(t_{w,95\%} - t_{w,5\%}) / t_{w,50\%}$	31.0	8.4	11.3	10.1

q (m/s)	Laxemar release area		Simpevarp release area	
	Model #13	Model #5	Model #13	Model #5
$q_{5\%}$	$1.8 \cdot 10^{-14}$	$1.2 \cdot 10^{-13}$	$1.3 \cdot 10^{-14}$	$3.9 \cdot 10^{-14}$
$q_{50\%}$	$2.1 \cdot 10^{-12}$	$1.3 \cdot 10^{-11}$	$9.1 \cdot 10^{-13}$	$3.4 \cdot 10^{-12}$
$q_{95\%}$	$8.0 \cdot 10^{-10}$	$8.2 \cdot 10^{-10}$	$2.4 \cdot 10^{-10}$	$2.5 \cdot 10^{-10}$
$(q_{95\%} - q_{5\%}) / q_{50\%}$	380.9	63.1	263.7	73.5

6.11 Sensitivity to the transmissivities of stochastic and deterministic structures

Particle tracking simulations were also performed for a sensitivity case in which the transmissivities of both the stochastic and the deterministic zones were reduced to 1/10 of their values in the Base Case. Thus, the results of this sensitivity case (Model #14) show the total effect of reduced transmissivities in both types of zones when compared to the Base Case (Model #5), and the additional effect of the deterministic zones when compared to the sensitivity case discussed in Section 6.10 (Model #13). For consistency with the rest of this chapter, we use Model #5 as reference case here.

Obviously, we expect a general increase in F-values and travel times for this sensitivity case, whereas the effects on flow paths and path lengths are more difficult to predict. As indicated by Figure 6-20, path lengths increase for particles released within the Laxemar area, especially in its western part, whereas both increases and decreases in path lengths can be observed for the Simpevarp area. In particular, a sub-area characterised by a relatively large decrease in path lengths is seen in the central eastern part of this release area.

As expected, the comparison of travel times in Figure 6-21 shows a more or less general, proportional increase in travel times for Model #14. With few exceptions (such as the SE corner of the Simpevarp release area), travel times increase sufficiently to cause changes in the displayed colours. Although the spatial patterns appear to be preserved, the visualisations of the sensitivity case indicate a somewhat smaller spatial variability in the travel times for the different starting positions.

A summary of the resulting particle tracking statistics for F, t_w and q is presented in Table 6-8. For the Laxemar release area, the increases in F- and t_w-values are nearly proportional to the reduction in transmissivities (a factor of 10), in some cases even larger. However, the median values of these parameters for the Simpevarp area show somewhat lower sensitivities to the transmissivities. The median Darcy fluxes decrease in proportion to the transmissivities for both release areas. Furthermore, it can be noted that the spatial variability in F-values for the flow paths is larger for Model #14 than for the Base Case (Model #5), whereas the travel time variability, as also observed in the visualisations, is smaller for the sensitivity case.

Table 6-8. Comparison of particle tracking results for Model #5 (Base Case) and Model #14 (sensitivity case addressing the transmissivities of stochastic and deterministic structures).

F (y/m)	Laxemar release area		Simpevarp release area	
	Model #14	Model #5	Model #14	Model #5
$F_{5\%}$	$4.3 \cdot 10^4$	$3.3 \cdot 10^3$	$4.9 \cdot 10^4$	$4.9 \cdot 10^3$
$F_{50\%}$	$5.0 \cdot 10^5$	$6.4 \cdot 10^4$	$5.2 \cdot 10^5$	$1.0 \cdot 10^5$
$F_{95\%}$	$9.8 \cdot 10^6$	$1.2 \cdot 10^6$	$1.2 \cdot 10^7$	$1.4 \cdot 10^6$
$(F_{95\%}-F_{5\%}) / F_{50\%}$	19.5	18.7	23.0	14.0

t_w (y)	Laxemar release area		Simpevarp release area	
	Model #14	Model #5	Model #14	Model #5
$t_{w,5\%}$	660	50	700	60
$t_{w,50\%}$	4,030	390	4,260	560
$t_{w,95\%}$	22,490	3,340	30,000	5,740
$(t_{w,95\%}-t_{w,5\%}) / t_{w,50\%}$	5.4	8.4	6.9	10.1

q (m/s)	Laxemar release area		Simpevarp release area	
	Model #14	Model #5	Model #14	Model #5
$q_{5\%}$	$2.0 \cdot 10^{-14}$	$1.2 \cdot 10^{-13}$	$7.7 \cdot 10^{-15}$	$3.9 \cdot 10^{-14}$
$q_{50\%}$	$1.4 \cdot 10^{-12}$	$1.3 \cdot 10^{-11}$	$3.9 \cdot 10^{-13}$	$3.4 \cdot 10^{-12}$
$q_{95\%}$	$8.5 \cdot 10^{-11}$	$8.2 \cdot 10^{-10}$	$3.4 \cdot 10^{-11}$	$2.5 \cdot 10^{-10}$
$(q_{95\%}-q_{5\%}) / q_{50\%}$	60.7	63.1	87.2	73.5
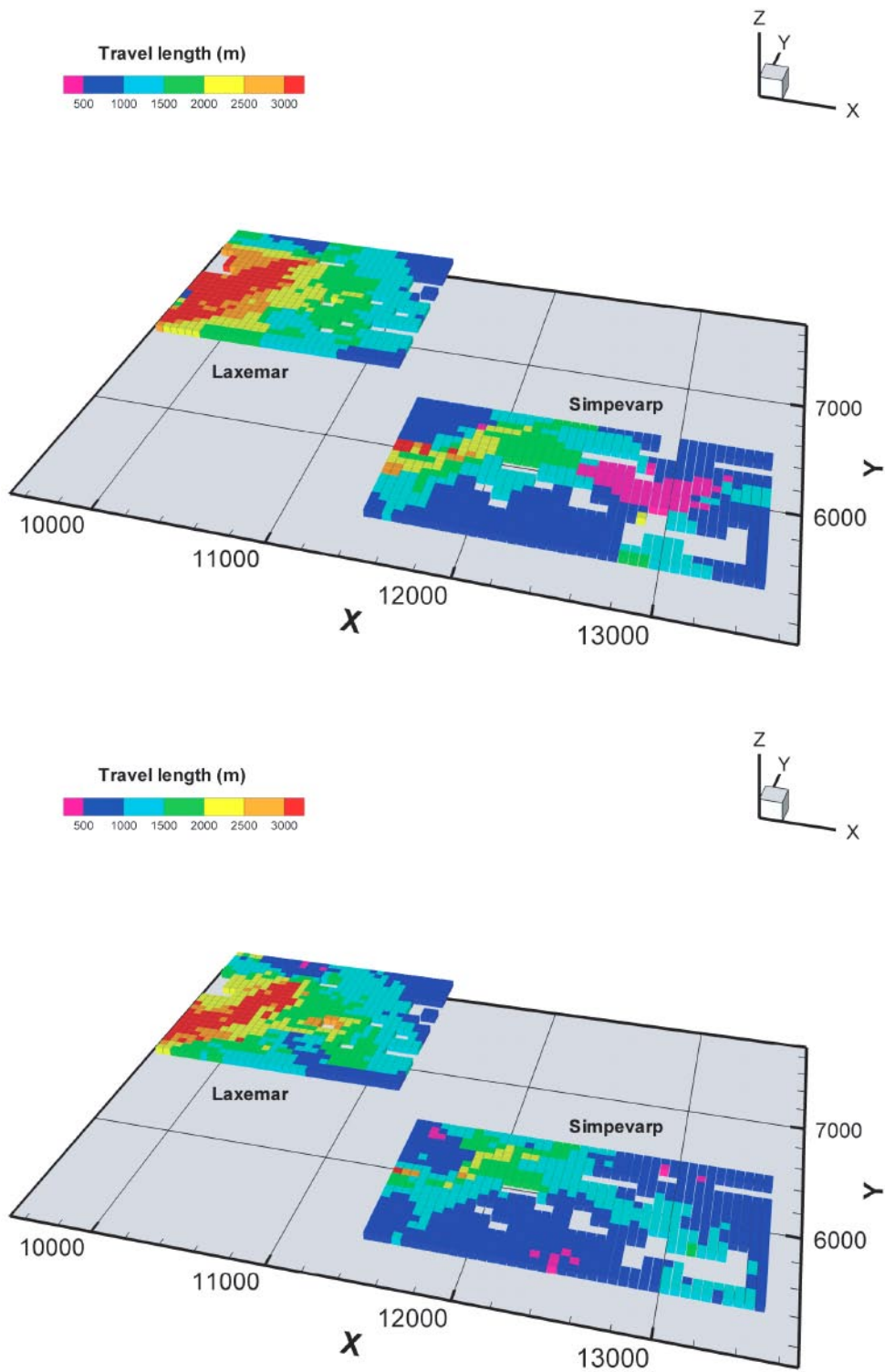
Figure 6-20. *Comparison of calculated flow path lengths, reported at each starting position, for Model #14 (sensitivity case; top) and Model #5 (Base Case; bottom). Empty cells indicate positions where no particles were released.*
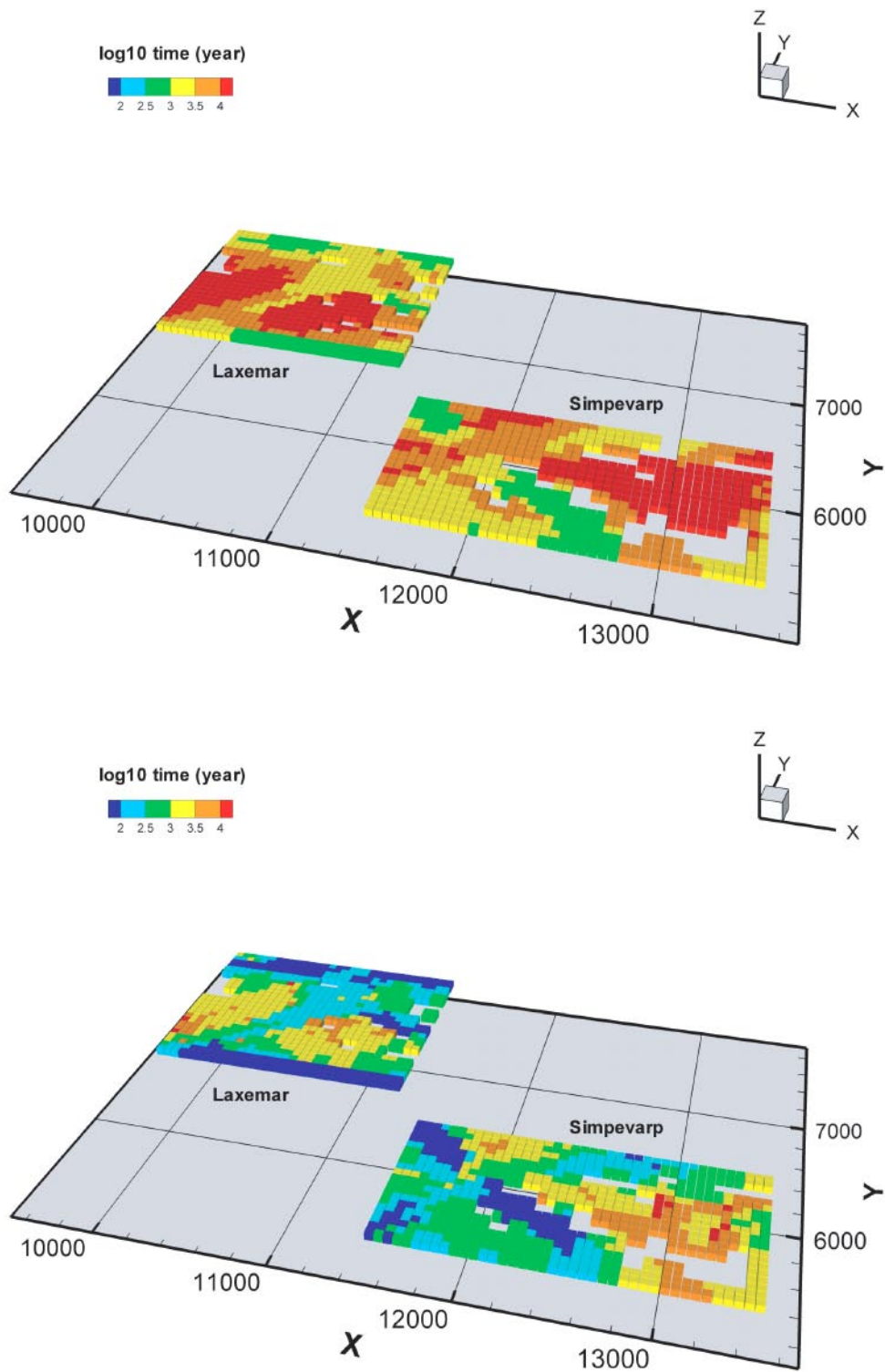
Figure 6-21. *Comparison of calculated travel times, reported at each starting position, for Model #14 (sensitivity case; top) and Model #5 (Base Case; bottom). Empty cells indicate positions where no particles were released.*

6.12 Summary of particle tracking statistics

Table 6-9 summarises the 5th, 50th and 95th percentiles from the particle tracking results for selected cases shown to have large effects on the transport parameters (Models #7–9 are excluded). In Table 6-10, a summary of the median F- and t_w-values for all cases is provided together with the corresponding quantifications of spatial variability. Finally, Table 6-11 presents the differences, relative to the Base Case, in the median values of F and t_w for the various sensitivity cases.

A comparison of the two defined release areas shows that both F-values and travel times generally are larger in the case of Simpevarp than for Laxemar. As noted above, the relative difference in median F- and t_w-values for the Base Case (Model #5) is about 50% when normalised with the values of the Laxemar release. However, the sensitivity study shows that the two release areas respond differently to the various parameter variations, such that this relation by no means should be regarded as general.

It is noted that the median values of both F and t_w in most cases are larger in the case of Simpevarp than for Laxemar, despite the fact that the advective flow paths generally are longer for the Laxemar release. The explanation for this observation is that the Laxemar subarea is strongly affected by the large, highly transmissive deterministically modelled deformation zones that cut straight through this release area. For the unconditional release used in this study, a large number of particles are released at unrealistic starting positions, i.e. in large zones.

At this stage, however, the results of the comparisons between the two release areas should not be taken as a basis for conclusions on the suitability of the one area relative to the other. The main messages conveyed by the present results are that the two release areas show some differences in the overall sensitivities to the parameter variations, and that different parameters/performance measures give somewhat different results when comparing release areas and sensitivity cases. In particular, path lengths are fairly insensitive to many input parameters, and may also behave qualitatively different from F and t_w in comparisons of release areas and in evaluations of sensitivities.

An equally important note is that if the transmissivity of the deterministically modelled deformation zones is decreased by an order of magnitude this change alone is more important for the particle tracking results than any of the other model variants. That is, Model #14 (realisation D) rendered the largest F-values and travel times of all model variations studied, differing significantly from all other cases. In conclusion, it is essential to understand the uncertainties in the characterisation of the deterministically modelled deformation zones.

Another interesting note is that the alternative DFN realisation based on the Base Case parameters (realisation B; Model #12) of the Laxemar release area rendered smaller F- and t_w-values than the first realisation (A). This is particularly noteworthy since the Base Case rendered an excellent match with the chosen hydrogeochemical calibration criteria, whereas B did not. It is also noted that in this particular case the difference in the DFN geometry between realisations was found to be as significant for the F-values as lowering the magnitude of $T = T(L)$ of the stochastic DFN for realisation A by an order of magnitude. Finally, the particle tracking results emphasise the importance of the properties of the uppermost rock layer for flow paths and transport parameters.

Table 6-9. Summary of particle tracking results for Model #3, #5 (A), #12 (B), #13 (C) and #14 (D). Model #5 = Base Case; <mark>max</mark>, <mark>min</mark>.

Rank	3	9	10	7	2	5	8	6	3	1
F (y/m)	Laxemar release area					Simpevarp release area				
	#3	#5	#12	#13	#14	#3	#5	#12	#13	#14
		A	B	C	D		A	B	C	D
$F_{5\%}$	$4.8 \cdot 10^4$	$3.3 \cdot 10^3$	$3.0 \cdot 10^3$	$3.2 \cdot 10^3$	$4.3 \cdot 10^4$	$6.5 \cdot 10^4$	$4.9 \cdot 10^3$	$7.2 \cdot 10^3$	$4.9 \cdot 10^3$	$4.9 \cdot 10^4$
$F_{50\%}$	$2.1 \cdot 10^5$	$6.4 \cdot 10^4$	$2.8 \cdot 10^4$	$1.1 \cdot 10^5$	$5.0 \cdot 10^5$	$1.6 \cdot 10^5$	$1.0 \cdot 10^5$	$1.5 \cdot 10^5$	$2.1 \cdot 10^5$	$5.2 \cdot 10^5$
$F_{95\%}$	$1.3 \cdot 10^6$	$1.2 \cdot 10^6$	$7.9 \cdot 10^5$	$8.4 \cdot 10^6$	$9.8 \cdot 10^6$	$1.3 \cdot 10^6$	$1.4 \cdot 10^6$	$9.6 \cdot 10^5$	$8.5 \cdot 10^6$	$1.2 \cdot 10^7$

Rank	8	9	10	4	3	7	6	5	2	1
Darcy flux q (m/s)	Laxemar release area					Simpevarp release area				
	#3	#5	#12	#13	#14	#3	#5	#12	#13	#14
		A	B	C	D		A	B	C	D
$q_{5\%}$	$1.1 \cdot 10^{-13}$	$1.2 \cdot 10^{-13}$	$2.6 \cdot 10^{-13}$	$1.8 \cdot 10^{-14}$	$2.0 \cdot 10^{-14}$	$3.6 \cdot 10^{-14}$	$3.9 \cdot 10^{-14}$	$1.1 \cdot 10^{-13}$	$1.3 \cdot 10^{-14}$	$7.7 \cdot 10^{-15}$
$q_{50\%}$	$6.8 \cdot 10^{-12}$	$1.3 \cdot 10^{-11}$	$1.5 \cdot 10^{-11}$	$2.1 \cdot 10^{-11}$	$1.4 \cdot 10^{-12}$	$4.5 \cdot 10^{-12}$	$3.4 \cdot 10^{-12}$	$3.1 \cdot 10^{-12}$	$9.1 \cdot 10^{-13}$	$3.9 \cdot 10^{-13}$
$q_{95\%}$	$3.9 \cdot 10^{-10}$	$8.2 \cdot 10^{-10}$	$7.3 \cdot 10^{-10}$	$8.0 \cdot 10^{-10}$	$8.5 \cdot 10^{-10}$	$2.1 \cdot 10^{-10}$	$2.5 \cdot 10^{-10}$	$1.9 \cdot 10^{-10}$	$2.4 \cdot 10^{-10}$	$3.4 \cdot 10^{-11}$

Rank	4	9	10	7	2	5	8	6	3	1
Travel time t_w (y)	Laxemar release area					Simpevarp release area				
	#3	#5	#12	#13	#14	#3	#5	#12	#13	#14
		A	B	C	D		A	B	C	D
$t_{w,5\%}$	450	50	60	50	660	900	60	90	60	700
$t_{w,50\%}$	1,560	390	300	580	4,030	1,320	560	790	1,610	4,260
$t_{w,95\%}$	4,380	3,340	3,340	18,000	22,490	4,920	5,740	3,220	18,220	30,000

117

Table 6-10. Particle tracking results for all investigated cases. Definition of selected measure of spatial variability: F-var = ($F_{95\%}$–$F_{5\%}$) / $F_{50\%}$ (similar for t_w); <mark>max</mark>, <mark>min</mark>.

	Laxemar release area				Simpevarp release area			
	$F_{50\%}$ (y/m)	F-var (–)	$t_{w,50\%}$ (y)	t_w-var (–)	$F_{50\%}$ (y/m)	F-var (–)	$t_{w,50\%}$ (y)	t_w-var (–)
Model #3	$2.1\cdot10^5$	6.0	1,560	2.5	$1.6\cdot10^5$	7.7	1,320	3.0
Model #5	$6.4\cdot10^4$	18.7	390	8.4	$1.0\cdot10^5$	14.0	560	10.1
Model #7	$5.1\cdot10^4$	19.5	450	10.1	$1.7\cdot10^5$	10.5	1,260	6.5
Model #8	$7.0\cdot10^4$	18.5	400	8.4	$9.4\cdot10^4$	17.0	540	12.1
Model #9	$3.6\cdot10^4$	8.5	200	7.3	$7.0\cdot10^4$	4.8	500	4.2
Model #12	$2.8\cdot10^4$	28.1	300	10.9	$1.5\cdot10^5$	6.4	790	4.0
Model #13	$1.1\cdot10^5$	76.3	580	31.0	$2.1\cdot10^5$	40.4	1,610	11.3
Model #14	$5.0\cdot10^5$	19.5	4,030	5.4	$5.2\cdot10^5$	23.0	4,260	6.9

Table 6-11. Evaluation of sensitivity cases, relative differences in median values of F and t_w compared to the Base Case. Reported values have been calculated as $\Delta F_{rel} = (F_{50\%,SC}–F_{50\%,BC}) / F_{50\%,BC}$, where indices "SC" and "BC" refer to "Sensitivity Case" and "Base Case", respectively (similar definition for t_w); <mark>largest increase</mark>, <mark>second largest increase</mark>, <mark>largest decrease</mark>.

	Laxemar release area		Simpevarp release area	
Sensitivity case	ΔF_{rel} (%)	$\Delta t_{w,rel}$ (%)	ΔF_{rel} (%)	$\Delta t_{w,rel}$ (%)
Uppermost rock layer (#3)	+228	+300	+60	+136
Initial salinity interface (#7)	–20	+15	+70	+125
Western model boundary (#8)	+9	+3	–6	–4
Flow porosity (#9)	–44	–49	–30	–11
DFN realisation (#12)	–56	–23	+50	+41
T, stochastic zones (#13)	+72	+49	+110	+188
T, stoch. and determ. zones (#14)	+681	+933	+420	+661

7   Discussion and conclusions

The work presented in this report investigates the possibility of using hydrogeochemical measurements in deep boreholes to reduce parameter uncertainty in regional modelling of groundwater flow and salt transport in fractured rock. The work was conducted with the aim of "improving the palaeo-hydrogeological understanding of the Simpevarp area" and to give recommendations to the preparations of the next version of the Preliminary Site Description (version 1.2). The study is based on a large number of numerical simulations of transient variable-density groundwater flow through a strongly heterogeneous and anisotropic porous medium. The sensitivity to a number of different hydrogeological assumptions was studied. The main findings of this study are:

1. The lack of sensitivity to the position of the western upstream boundary for the simulated conditions at the two subareas Simpevarp and Laxemar. This suggests that the current size of the regional model domain may be sufficient for the Preliminary Site Descriptions version 1.2 of the two subareas. However, it is noted that the work presented here is based on the V0 deformation zone model and preliminary fracture statistics from the Laxemar subarea gathered prior to the start of the site investigations. Changes in this information as a result of the site investigations may call for a revisit.

2. The local topography within the model domain, which was used to define the ground water table in this study, causes local flow cells that reach repository depth at the two subareas. The simulation results suggest that the Laxemar subarea is predominantly subjected to recharging flow conditions at (–500) masl. In contrast, the Simpevarp subarea is predominantly subjected to discharging flow conditions.

3. The hydrogeological properties of the deterministically modelled deformation zones (DDZ) are very important for the palaeo-hydrogeological understanding. The motivation for the assumed hydraulic properties used in this study should be scrutinised in the preparations of the next model version of the Preliminary Site Description. For instance, in the work reported here it was concluded that a decrease of the transmissivity of the deterministically modelled deformation zones by an order magnitude reinforced the relative strength of the local flow field and had a great impact on the flow related transport parameters.

4. The assumed geometric and hydraulic properties of the stochastic DFN, i.e. the stochastically modelled deformation zones (SDZ), were found to be of significance for the simulation results, where the geometry of the stochastic DFN was found to be as important as the decrease in the magnitude of the transmissivity correlation. A probable explanation for this result is the sparse fracture intensity used in the simulations. The motivation for the assumed fracture intensity used in this study should be scrutinised in the preparations of the next model version of the Preliminary Site Description.

5. Salinity can be an insensitive parameter for hydrogeological calibration. For some of the sensitivity cases the differences in the salinity field were not as significant as one would expect. To some extent this observation can probably be linked to the uncertainty about the looks of the initial salinity field at 10,000 BC (12,000 BP). The problem can be described as a matter of hydraulic equivalence. That is, starting with two different salinity interfaces, the hydraulic parameter settings can be adjusted to make both cases match the present-day situation reasonably well. Hopefully, this complexity can be resolved by incorporating more data.

6. Integration with hydrogeochemistry by simulation of different water types may be useful as guidance in the calibration process. The water type simulations were found to reveal differences between sensitivity cases that were not readily seen in the salinity results. The integration between the water type simulations and the M3 calculations is an interesting approach that hopefully can be improved by more data in V1.2. It is noted that the use of water types in this study was not fully developed, e.g. no matrix diffusion was used except for the salinity.

7. The flow porosity of the deformation zones affects their initial contents of salinity, which in turn affects the extent of the post-glacial flushing during the shoreline displacement. As a consequence, differences in the Darcy flux field were obtained, which affected the flow related transport parameters.

8. The results from the particle tracking show that F and t_w are highly spatially variable and that the variability follows a similar pattern, i.e. the two parameters are correlated. A comparison of the two release areas where particles were released show that both F-quotients and travel times for the base case generally are larger for the Simpevarp subarea than for the Laxemar subarea. The results indicate that spatial variability is an important source to uncertainty. Essentially, all sensitivity variants indicate high uncertainties in the flow related transport parameters. In particular, the variants addressing the properties of the uppermost rock layer and the outcropping and transmissivities of the deterministic and stochastic deformation zones show large differences compared to the Base Case. This emphasises the importance of the interactions with the surface system and the uncertainties related to the underlying description of the deterministic and stochastic deformation zones for the resulting uncertainties in the flow related transport parameters.

Finally, the comparisons between simulated data and borehole observations leading to the above conclusions were made for a horizontal grid size of 100 m. That is, fractures and deformation zones of sizes smaller than 100 m were not described explicitly in the present regional scale model. Since these features can be expected to contribute significantly to the integrated F- and t_w-values for flowpaths from repository depth, the calculated flow related transport parameters are not considered quantitative in the sense that they should be used for detailed comparisons with safety criteria, or with results from other sites. However, it should be noted that all median values of F for the two release areas in the present modelling results (including all sensitivity cases) exceed 10^4 year/m, which is the suitability indicator value expressed in /Andersson et al. 2000/.

8   References

Andersson J, Elert M, Gylling B, Moreno L, Selroos J-O, 1998. Derivation and treatment of the flow wetted surface and other geosphere parameters in the transport models FARF31 and COMP23 for use in safety assessment. SKB R-98-60, Svensk Kärnbränslehantering AB.

Andersson J, Ström A, Svemar C, Almén K-E, Ericsson L O, 2000. What requirements does the KBS-3 repository make on the host rock? Geoscientific suitability indicators and criteria for siting and site evaluation. SKB TR-00-12, Svensk Kärnbränslehantering AB.

Andersson P, Byegård J, Dershowitz W, Doe T, Hermanson J, Meier P, Tullborg E-L, Winberg A, 2002b. TRUE Block Scale Project, Final report 1: Characterisation and model development. SKB TR-02-13, Svensk Kärnbränslehantering AB.

Andersson J, 2003. Site descriptive modelling – strategy for integrated evaluation. SKB R-03-05, Svensk Kärnbränslehantering AB.

Antal I, Bergman T, Gierup J, Rudmark L, Thunholm B, Wahlgren C-H, Stephens M, Johansson R, 1998. Översiktsstudie av Kalmar län – Geologiska förutsättningar. SKB R-98-24, Svensk Kärnbränslehantering AB.

Bergman T, Johansson R, Lindén A H, Rudmark L, Wahlgren C-H, Follin S, Isaksson H, Lindroos H, Stanfors R, 1999. Förstudie Oskarshamn – Erfarenheter från geovetenskapliga undersökningar i nordöstra delen av kommunen. SKB R-99-04, Svensk Kärnbränslehantering AB.

Brydsten L, 1999. Shore line displacement in Öregrundsgrepen. SKB TR-99-16, Svensk Kärnbränslehantering AB.

Darcel C, 2003. True Block Scale continuation project – Assessment of the feasibility of tracer tests with injection in "background factures" usin a model based on a power law fracture length distribution. SKB R-00-46, Svensk Kärnbränslehantering AB.

Dershowitz W, Winberg A, Hermanson J, Byegård J, Tullborg E-L, Andersson P, Mazurek M, 2003. Äspö Task Force on modelling of groundwater flow and transport of solutes. Task 6C. A semi-synthetic model of block scale conductive structures at the Äspö HRL. SKB IPR-03-13, Svensk Kärnbränslehantering AB.

Follin S, Askling P, Carlsten S, Stråhle A, 2000. Smålandsgranitens vattengenomsläpplighet. SKB R-00-46, Svensk Kärnbränslehantering AB.

Haggerty R, Gorelick S M, 1995. Multi-rate mass transfer for modelling diffusion and surface reactions in media with pore-scale heterogeneity. Water Resources Research, 31(10), 2383–2400.

Holmén J G, Stigsson M, Marsic N, Gylling B, 2003. Modelling of groundwater flow and flow paths for a large regional domain in northeast Uppland. SKB R-03-24, Svensk Kärnbränslehantering AB.

Laaksoharju M, Skårman C, Skårman E, 1999a. Multivariate Mixing and Mass balance (M3) calculations – a new tool for decoding the hydrogeochemical information. Applied Geochemistry, 14(7), 861–871.

Laaksoharju M, Tullborg E-L, Wikberg P, Wallin B, Smellie J, 1999b.
Hydrogeochemical conditions and evaluation at the Äspö HRL, Sweden. Applied Geochemistry, 14(7), 835–859.

Påsse T, 1996. A mathematical model of the shore level displacement in Fennoscandia. SKB TR-96-24, Svensk Kärnbränslehantering AB.

Rhén I, Follin S, Hermanson J, 2003. Hydrogeological Site Descriptive Model – a strategy for its development during Site Investigations. SKB R-03-08, Svensk Kärnbränslehantering AB.

Rohr-Torp E, 2000. Postglacial isostatic uplift and ground water potential. In: Knutsson G (ed), Proceedings of the Workshop on Hardrock Hydrogeology of the Fennoscandian Shield, Äspö, Sweden, May 26–27, 1998. Nordic Hydrological Programme, NHP Report Number 45.

SKB, 2000. Geoscientific programme for investigation and evaluation of sites for the deep repository. SKB TR-00-20, Svensk Kärnbränslehantering AB.

SKB, 2001. Site Investigations. Investigation methods and general execution programme. SKB TR-01-29, Svensk Kärnbränslehantering AB.

SKB, 2002. Forsmark – site descriptive model version 0. SKB R-02-35, Svensk Kärnbränslehantering AB.

SKB, 2004. Preliminary Site Description, Forsmark area, version 1.1. SKB R-04-15, Svensk Kärnbränslehantering AB.

Svensson U, 2001a. A continuum representation of fracture networks. Part I: Method and basic test cases. Journal of Hydrology, Volume 250, 170–186.

Svensson U, 2001b. A continuum representation of fracture networks. Part II: Application to the Äspö Hard Rock Laboratory. Journal of Hydrology, Volume 250, 187–205.

Svensson U, 2004. DarcyTools, Version 2.1. Verification and validation. SKB R-04-21, Svensk Kärnbränslehantering AB.

Svensson U, Ferry M, 2004. DarcyTools, Version 2.1. User's guide. SKB R-04-20, Svensk Kärnbränslehantering AB.

Svensson U, Kuylenstierna H-O, Ferry M, 2004. DarcyTools, Version 2.1. Concepts, methods, equations and demo simulations. SKB R-04-19, Svensk Kärnbränslehantering AB.

Westman P, Wastegård S, Schoning K, Gustafsson B, Omstedt A, 1999. Salinity change in the Baltic sea during the last 8,500 years: evidence, causes and models. SKB TR-99-38, Svensk Kärnbränslehantering AB.